COHERENT INTERFERENCE EFFECTS AND SQUEEZED LIGHT GENERATION IN OPTOMECHANICAL SYSTEMS

By

KENAN QU

Bachelor of Science in Microelectronics
Nankai University
Tianjin, China
2009

Submitted to the Faculty of the
Graduate College of
Oklahoma State University
in partial fulfillment of
the requirements for
the Degree of
DOCTOR OF PHILOSOPHY
December, 2015

COHERENT INTERFERENCE EFFECTS AND SQUEEZED LIGHT GENERATION IN OPTOMECHANICAL SYSTEMS

Dissertation Approved:

Prof. Girish S. Agarwal (Dissertation Advisor)

Prof. Albert T. Rosenberger

Prof. Jacques H. H. Perk

Prof. Yingmei Liu

Prof. Daniel R. Grischkowsky

ACKNOWLEDGMENTS

This dissertation marks the end of my journey in obtaining my Ph.D, which I have been traveling through fulfilled with joyfulness and gratefulness despite the years of intensive study and diligent effort. This dissertation presents a concentration of my work in the field of cavity optomechanics conducted in the Department of Physics at Oklahoma State University (OSU). My experience at OSU has been nothing short of amazing as I have been given unique opportunities and taken advantage of them. I have felt at home since the first day that I arrived at OSU and during these years I have grown both personally and academically. I already see the results emanating from what I learned, and for that, I am most humble and most grateful.

At this moment of accomplishment, I'd like to pay homage to my advisor, Prof. Girish S. Agarwal, who has supported me throughout my Ph.D study with his vast amount of knowledge, ingenious understanding of physics and maybe most importantly, patience. I have been amazingly fortunate to have Prof. Agarwal's guidance to understand physics, especially quantum optics, and then apply the obtained knowledge in creating new physics — a career I would like to devote my life to. I notice that I learn physics best from those professors who model difficult physical concepts with concise and elegant mathematics. Essentially, Prof. Agarwal laid out a landscape of the physical model and then focused on individual details of it. In each step of the mathematical derivation, he kept relating it to the overall model. A sort of retraction of the lens then followed, which facilitated a mushrooming of the mind. He has the supreme art to awaken joy in creative expression and knowledge. There is a lot of hardship in the Ph.D pursuit. Prof. Agarwal's selfless time and care were sometimes all that kept me going. I attribute the level of my Ph.D degree to his encouragement and effort and without him would never have been completed.

I gratefully acknowledge my dissertation committee who guided me through my Ph.D pursuit, as well as my course teachers who tutored me the esoteric methods

Acknowledgements reflect the views of the author and are not endorsed by committee members or Oklahoma State University.

necessary for my research. Thank you to Albert Rosenberger, Jacques Perk, Yingmei Liu, Daniel Grischkowsky, Satyanaravan Nandi, Bruce Ackerson, Kaladi Babu, and Eric Benton. I take this opportunity to sincerely acknowledge Prof. Roserberger for providing top-quality courses on the subject of lasers and, in a broader sense, light which contribute enormously to the qualification for my next stage postdoctoral study in intense laser plasma interaction. He did a fabulous job of instructing and I would like to extend a huge warm thanks to him for letting me take or audit all his courses which I always enjoyed listening to. His consistent class quality broadcasts his insightful understanding of lasers into my mind through plain words. I also acknowledge Prof. Perk, who was always there whenever I had a question. His constructive criticism at different stages of my study were thought-provoking. Prof. Nandi is one of the most gracious teachers that I have had in my life. He has inadvertently, and without fail, provided something much greater—a friendly smile and a small talk every time we met. His encouragement and personal attention have provided good and smooth basis for my Ph.D track.

Dozens of workmates and visiting scholars have helped me and taught me immensely in my office. The previous Ph.D student Dr. Sumei Huang introduced me to the basics when I started my Ph.D study. Prof. Subhasish Dutta-Gupta is not only a great professor but also a fantastic friend who shares with me the same interests in electronic gadgets and photography. I greatly appreciate that we still keep in contact today. I would like to acknowledge Prof. Sudhanshu Jha, Jan Sperling, Svend-Age Biehs, Xuele Liu, Thomas Kipf, and Daniel Bhatti for numerous discussions on related topics in quantum optics that helped me improve my knowledge in the area. I also acknowledge my collaborators for lending me their expertise and intuition in my research: Prof. Hailin Wang, Dr. Chunhua Dong, Prof. Weili Zhang and Ningning Xu.

Beyond physics, I am indebt to my wife, He Sun, who abandoned her former job, devoted her life to me, and brought unconditional support and companionship during my Ph.D study. Her tolerance of my occasional vulgar moods is a testament in itself of her unyielding devotion and love. My immediate family including my wife and my parents to whom this dissertation is dedicated have been a constant source of love, concern, support and strength through all these years. I would like to express my heart-felt gratitude to them. I also deeply thank my parents-in-law for their trust

Acknowledgements reflect the views of the author and are not endorsed by committee members or Oklahoma State University.

and encouragement. I warmly appreciate their generosity and understanding.

In my daily work, I have been blessed with a cheerful group of friends. My Ph.D life became joyful mostly because of them. Special thanks to Jigang Zhao who has been my roommate for one year and will be my friend for all my life. We together learned to enjoy the American life by travelling through half of the continent, chatting and commenting on what we saw on the road. I will never forget our holiday gathering dinners and the group trip to the Rocky Mountains with my friends Penghui Lin and Huan Song, Lian Duan and Yi Tian, Yun Zhao and Er Yue. You all shared my best days at OSU. Thank you to Eric Gonzales, Rajagopal Raj, Limu Ke, Shaikh Saad, Hem Moktan, Shreyashi Chakdar, and all other friends including my students in the Physics Department. Chatting with Shuo Dai and Meng Ding has brightened many a dull lunchtime which helped me keep a healthy mental state.

Finally, I appreciate Prof. Agarwal and the Physics Department at OSU for funding my Ph.D research.

Acknowledgements reflect the views of the author and are not endorsed by committee members or Oklahoma State University.

Name: Kenan Qu

Date of Degree: December, 2015

Title of Study: COHERENT INTERFERENCE EFFECTS AND SQUEEZED LIGHT GENERATION IN OPTOMECHANICAL SYSTEMS

Major Field: Physics

My Ph.D dissertation is on the fundamental effects in optomechanical systems (OMS) and their important applications. The OMS are based on the possibility of the mechanical motion produced by few photons incident on the mechanical device. This dissertation presents several applications of the OMS in the area of storage of light in long-lived phonons, single mode optomechanical Ramsey interferometry, and generation of large amount of squeezing in the output radiation. The long-lived phonons can be monitored and controlled via optical means as was experimentally demonstrated. To show this, I develop the theory of transient electromagnetically induced transparency (EIT). For further applications like state transfer, especially over very different frequency regimes, I consider double-cavity OMS, where the two cavities can correspond to different spectral domains, yet the state transfer is possible via phonons. The state transfer is based on a new effect, electromagnetically induced absorption (EIA), where one uses a second control field from the other cavity to produce an absorption peak inside the EIT window. All these involve the interference of various path ways via which a final state is reached. The following chapter shows how Fano-like interference can arise in OMS. A Fano asymmetry parameter for OMS was defined.

The last two chapters deal with the question if OMS can be efficient generators of squeezed light. I show by blue and red tuning the two cavities in a double-cavity OMS, one can generate effectively a two-mode parametric interaction which yields two-mode squeezed output with the squeezing magnitude of the order of 10dB. This requires a bath temperature of 10mK. Such temperatures obtained by using Helium dilution refrigerator are routinely used with superconducting OMS. The major part of this dissertation is devoted to the dispersive optomechanical interaction. However, the interaction can also be dissipative, where the mechanical displacement modulates the cavity decay rate. Such dissipative OMS have unusual quantum features. The last chapter discusses the squeezing capability of dissipative optomechanical interaction. Very large squeezing of the order of 10dB or more can be produced. Clearly the work of the earlier chapters can be extended to cover dissipative OMS.

ADVISOR'S APPROVAL: _____

TABLE OF CONTENTS

LIST OF FIGURES

CHAPTER 1

INTRODUCTION TO CAVITY OPTOMECHANICS

Light, as is well-known, carries energy as well as momentum exerting radiation pressure to particles. Perhaps the most striking example is comet dust tails pointing away from the sun. Kepler postulated in 1619 that this phenomenon is due to radiation pressure of the sun light. That light can push matter is quite contrary to everyday experience. Nevertheless, radiation pressure plays an important role as it acts on the interplanetary dust. Under certain conditions, solar radiation pressure can greatly increase and even exceed solar gravity, thereby ejecting dust into interstellar space. Attempts to theoretically explain radiation pressure can be dated back to immediately after Kepler's postulate. Newton used his corpuscular theory, however, only to find that the repulsion between the sun and comet tails was merely due to the buoyancy forces exerted by the ambient ether. Euler in 1744 adopted Huygens's longitudinal wave theory of light and treated the repulsion as due to a series of mechanical impacts. Ultimately, the correct theory of radiation pressure was theoretically developed by Maxwell in 1876 as a result of his electro-magnetic theory of light and also independently derived by Bartoli in 1876 as a consequence of the second law of thermal dynamics. Based on Planck's proposal that blackbody radiates electro-magnetic field in discrete frequencies, Einstein developed the quantum description of radiation pressure in 1909, which earned him the Nobel prize in 1921, identifying light as discrete packets with specific energy and momentum.

The experimental verification, however, only yielded few conclusive results considering that the radiation pressure force is orders of magnitudes weaker than the collision

force with massive air molecules. The invention of lasers finally altered this situation, and Arthur Ashkin in 1970 [1] demonstrated that focused laser beams can trap and control dielectric particles making radiation pressure a useful laboratory tool. Laser cooling based on radiation pressure was subsequently realized experimentally in the 1980s allowing cooling of ions to their motional quantum ground state. Braginsky [2] investigated the role of radiation pressure and its ability of cooling macroscopic systems in the context of interferometers. His research advanced the study of radiation pressure to the quantum level which imposes a limit on how quantum fluctuations of radiation pressure hinder the accuracy of mechanical control. Cavity optomechanics has been explored theoretically in several aspects since then. In 2005, the advent of nanofabrication technology combined with advanced optical microcavities enabled the dispersive optomechanical coupling during which energy is conserved. Since then, the field of cavity optomechanics, at the intersection of nanophysics and quantum optics, has gained tremendous popularity [3–5].

A cavity optomechancial system (OMS) encompasses micro- or nanofabricated structures realizing high quality mechanical oscillators coupled to single mode optical or microwave cavities via radiation pressure or most recently also via optical gradient forces [6–12]. This mechanism offers disparate possibilities of both theoretical and experimental studies due to the versatile design of optical (microwave [13–15]) cavities and a large variety of mechanical elements including vibrating end-mirrors [16, 17], whispering gallery modes [18–21], cold atoms [22–24], etc. [25–29]. In general, this field is driven by promising aspects, such as ultrasensitive measurements, tests of quantum mechanics in macroscopic systems, classical signal or quantum information processing, and all-light optomechanical circuits. It has been shown theoretically [30, 31] that these micro- or nanomechanical systems can in fact be laser cooled to their quantum mechanical ground state via radiation pressure optomechanical coupling, and corresponding experiments [32–34] have also been demonstrated to cool down

the mean mechanical occupation number of a few quanta.

In this chapter, I introduce the theoretical model of OMS starting from the theory of optical cavities and the Hamiltonian of the optomechanical interaction. Then I derive the Heisenberg equation of motion and continue with the standard procedure of linearization. I further describe the enhancement of optomechanical coupling by using driving lasers with different frequencies. The stability condition which is essential to all OMS studies will also be discussed in detail.

1.1 Hamiltonian for an optomechanical system

The standard model of OMS consists of an optical Fabry-Pérot cavity with one of its end-mirror mounted on a spring, as illustrated in Fig. 1.1. The left boundary of

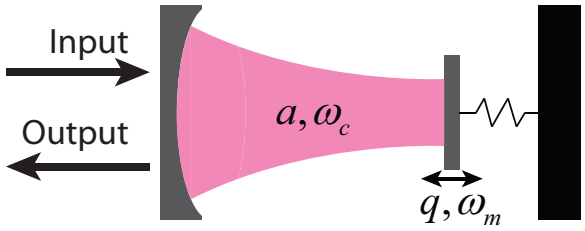

Figure 1.1: Schematic of optomechanical system.

the cavity is a partial transmissive mirror with a power reflectivity $R \approx 1$, serving as the interface of the intra-cavity field and the input/output fields. A total reflective mirror determines the right boundary of the cavity. The cavity has its resonance frequencies such that the cavity can employ the power of constructive interference in order to create a standing wave within the confines of the cavity. For an empty cavity, the resonance frequencies are $\omega_c = n\frac{\pi c}{L}$ where n is an integer. The frequency difference between two consecutive resonances is called the free spectral range $\nu_{\text{fsr}} = \frac{\pi c}{L}$. Its reciprocal represents the round trip time of an intra-cavity photon $\frac{2\pi}{\nu_{\text{fsr}}} = \frac{L}{2c}$. Finesse [35] is another important parameter of the cavity describing how many round trips a photon bounces inside the cavity before leaking out through the partial

transmissive mirror. If we ignore other internal losses, it is solely determined by the power reflectivity and has the form $\mathcal{F} = \frac{\pi\sqrt{R}}{1-R}$. Finesse also indicates how much narrower the transmission peak is compared to the free spectral range. Hence, the photon lifetime can be obtained by multiplying the photon round-trip time with round-trip numbers $\tau_c = \frac{L}{2c}\mathcal{F}$. In the study of OMS, we are more interested in the cavity photon decay rate $2\kappa_e$ which takes the form $2\kappa_e = \frac{2\pi}{\tau_c} = \frac{\pi c}{L\mathcal{F}}$. The input laser field is sent into the cavity through the partial transmissive mirror. Let's assume the input laser has a frequency ω_l and power $\mathcal{P}_l$. The photon number incident on the cavity input per unit time is $\mathcal{P}_l/(\hbar\omega_l)$ and this value is to be multiplied with the cavity photon decay rate $2\kappa_e$ to get the photon number that leaks into the cavity. Hence the input laser amplitude inside the cavity is $\mathcal{E}_l = \sqrt{2\kappa_e\mathcal{P}_l/(\hbar\omega_l)}$. Once the input laser is applied, the cavity quickly builds up an intra-cavity field. The cavity photons when being reflected from the mirrors exert a radiation pressure onto the mirrors. Since the right side mirror is mounted to a spring, the radiation pressure induces a mechanical motion. We describe the state of the end-mirror with the displacement q and momentum p. On the other hand, the displacement q also modulates the cavity resonance frequency $\omega_c(q)$ by changing the cavity length $L+q$. We denote the cavity field using the annihilation operator a, hence the field energy can be written as $\hbar\omega_c(q)a^\dagger a$. The cavity field operator obeys the commutation relation $[a, a^\dagger] = 1$. The mechanical motion of the end-mirror can be well described using a harmonic oscillator with oscillation frequency ω_m. The system Hamiltonian can be thus written as

$$\begin{aligned} H &= H_c + H_m + H_{\mathrm{dr}} \\ &= \hbar\omega_c(q)a^\dagger a + \frac{1}{2}m\omega_m^2 q^2 + \frac{p^2}{2m} + i\hbar\mathcal{E}_l(a^\dagger e^{-i\omega_l t} - a e^{i\omega_l t}), \end{aligned} \tag{1.1}$$

where m refers to the mass of the oscillating end-mirror. The Hamiltonian has three parts: the first term (H_c) is the cavity field energy; the two terms in the middle (H_m) are for the mechanical harmonic oscillator and the last term (H_{dr}) describes the

coupling between the cavity field a and the input laser field $\mathcal{E}_l e^{-i\omega_l t}$.

Since the optical resonance frequency is a function of cavity length, it can be expanded with respect to the mirror displacement q:

$$\omega_c(q) = \omega_c(1 - \frac{q}{L} + \cdots), \tag{1.2}$$

with L the empty cavity length and ω_c the optical resonance frequency for $q = 0$. For convenience, we describe the mechanical oscillator using the dimensionless and normalized displacement operator $Q = q/(\sqrt{2}q_{\mathrm{zpf}})$ and momentum operator $P = p(\sqrt{2}q_{\mathrm{zpf}}/\hbar)$ with $q_{\mathrm{zpf}} = \sqrt{\hbar/(2m\omega_m)}$ being the size of the mechanical zero-point fluctuations, *i.e.* width of the mechanical displacement in the ground state. They obey the commutation relation $[Q, P] = [q, p]/\hbar = i$. Thus we can write the standard optomechanical Hamiltonian as

$$H = \hbar\omega_c a^\dagger a - \hbar\sqrt{2}g a^\dagger a Q + \frac{1}{2}\hbar\omega_m(Q^2 + P^2) + i\hbar\mathcal{E}_l(a^\dagger e^{-i\omega_l t} - a e^{i\omega_l t}). \tag{1.3}$$

Here we have identified $g \equiv \omega_c \frac{q_{\mathrm{zpf}}}{L}$ as the optomechanical single-photon coupling strength [1]. The optomechanical coupling term is written as

$$H_{\mathrm{int}} = -\hbar\sqrt{2}g a^\dagger a Q. \tag{1.4}$$

This can be interpreted as a radiation pressure force $F_{\mathrm{rad}} = \hbar\omega_c a^\dagger a/L$. Its full rigorous derivation uses the Maxwell stress tensor [36]. The simplest form can be explained using the momentum transfer due to the photon reflection by the end-mirror of the cavity. A single cavity photon with frequency ω_c carries momentum $h/\lambda = \hbar\omega_c/L$. Consequently, the radiation pressure force is equal to the single photon momentum transfer multiplied by the cavity photon number, *i.e.* $F_{\mathrm{rad}} = (\hbar\omega_c/L)a^\dagger a$. In essence, there are higher-order coupling terms, *e.g.* quadratic optomechanical coupling in a

[1] Note that the factor $\sqrt{2}$ in the interaction term appears as a result of the transformation $q = \sqrt{2}Q * q_{\mathrm{zpf}}$. In some papers, this factor $\sqrt{2}$ is not shown which indicates that they use a different convention of the optomechanical coupling rate g.

membrane in-the-middle setup [37–39]. However, they are much weaker than the first-order coupling term in most typical optomechanical systems.

It is convenient to work in a rotating frame, in which the Hamiltonian becomes

$$H = \hbar(\omega_c - \omega_l)a^\dagger a - \hbar\sqrt{2}ga^\dagger aQ + \frac{1}{2}\hbar\omega_m(Q^2 + P^2) + i\hbar\mathcal{E}_l(a^\dagger - a). \tag{1.5}$$

In many cases, we also second quantize the mechanical oscillator by writing $Q = (b + b^\dagger)/\sqrt{2}$ and $P = (b - b^\dagger)/(\sqrt{2}i)$. This is particularly convenient when we treat the mechanical oscillation as phonons and we analyze the photon-phonon interaction. With this description, the standard optomechanical Hamiltonian takes the form

$$H = \hbar\omega_c a^\dagger a - \hbar g a^\dagger a(b + b^\dagger) + \hbar\omega_m b^\dagger b + i\hbar\mathcal{E}_l(a^\dagger e^{-i\omega_l t} - ae^{i\omega_l t}). \tag{1.6}$$

This is frequently used as the starting point in OMS calculations and studies of it yield various interesting phenomena. If an OMS is driven by a red-detuned laser, the optical state is swapped with the mechanical state aided by the red detuned driving laser. Optomechanical cooling is realized when the cavity mode is a vacuum field with an effectively zero temperature and hence the mechanical mode is cooled down by exchanging energy with it. The coupling of optical and mechanical mode leads to a well-known phenomenon "normal-mode splitting" at high driving powers. A hybridization of the mechanical motion with the cavity field occurs and leads to a splitting of the mechanical and cavity output spectra. If a probe laser is applied at the cavity frequency together with the driving laser, they combine to create coherent phonons. This process is resonantly enhanced when the beating frequency of the lasers is identical to the mechanical frequency. This coherent process stimulates a plethora of phenomena and a prominent example is Electromagnetically Induced Transparency/Absorption (EIT/EIA) in OMS (*cf.* Secs. 2 and 3). If the driving laser is blue-detuned, it parametrically generates an entangled photon-phonon pair (*cf.* Sec. 5). It may serve as a promising building block for hybrid quantum networks and for quantum state engineering. This type of parametric process plays a central

role in generating nonclassical optical and mechanical states with negative Wigner density. When the driving laser is on-resonance, it does not enhance the process of photon creation or annihilation. The optical state experiences a shift proportional to the displacement. This translates into a phase shift of the reflected/transmitted light beam, which can be used to read out the mechanical motion in a Quantum non-demolition (QND) manner. It indicates that the Squeezed light can be generated with a single on-resonance driving laser in a standard OMS (*cf.* Sec. 6).

The increasing attention focused to optomechanics and the development of nanofabrication technology has been driving a plethora of experiments and pushing state of the art in this field. Here I list a few examples of the optomechanical coupling strengths in various setups. The single photon coupling strength is $g \sim 2\pi \times 7.7\text{Hz}$ in an OMS with a micromirror [40], and is an order of magnitude larger in an OMS with a membrane [37] $g \sim 2\pi \times 50\text{Hz}$ due to the light weight of the membrane. A remarkable achievement is demonstrated in the whispering gallery mode of a silica microsphere [19, 41] that g can reach $\sim 2\pi \times 0.2\text{MHz}$. Recently, g as high as $\sim 2\pi \times 11.5\text{MHz}$ has been realized in a sliced photonic crystal nanobeam [42].

1.2 Dynamics of an optomechanical system

The Hamiltonian (1.6) describes the interaction between the optical cavity mode a and the mechanical mode b subject to the coherent driving laser $\mathcal{E}_l$. Even with state of the art optomechanical technology, the cavity photon dissipation happens at a rate much larger than the coupling rate g. Therefore, one must take into account the optical and mechanical dissipation when studying the system evolution. This can be achieved either by focusing on the time evolution of the operators using the Heisenberg equations of motion, or analyzing the time evolution of the states using the master equation. These two approaches are equivalent to each other and can be adopted by choice.

Next we write down the nonlinear quantum Langevin equations by applying the Heisenberg equation of motion $\dot{A} = \frac{i}{\hbar}[H, A] + \frac{\partial A}{\partial t}$ for an operator A and adding the dissipation and noise terms, and we find

$$\begin{cases} \dot{Q} = \omega_m P, \\ \dot{P} = -\omega_m Q + \sqrt{2} g a^\dagger a - \gamma_m P + \xi, \\ \dot{a} = -i[\omega_c - \omega_l - \sqrt{2} g Q] a - \kappa a + \mathcal{E}_l + \sqrt{2\kappa_e} a_{\rm in} + \sqrt{2\kappa_i} a_{\rm int}, \end{cases} \tag{1.7}$$

Here, in conjunction with the external noise source $\sqrt{2\kappa_e} a_{\rm in}$ due to the input-output coupling, we also include an internal noise term $\sqrt{2\kappa_i} a_{\rm int}$ due to factors like non-perfect mirrors or scattered light from the residue air molecules in the cavity. We write the cavity field decay rate as $\kappa = \kappa_e + \kappa_i$, where κ_e and κ_i denote the external and internal decay rates. The intra-cavity field leaks through the partial reflective mirror of the Fabry-Pérot cavity at rate κ_e and the output field can be collected by a detector. On the contrary, the internal decay dissipates the cavity field into inaccessible channels at rate κ_i. To quantify the efficiency, a parameter $\eta = \kappa_e/(\kappa_e + \kappa_i)$ is defined to describe the output coupling ratio. One has to bear in mind that κ is the cavity field (amplitude) decay rate, while the cavity energy (photon) decay rate would be 2κ.[2] We use γ_m to represent the mechanical phonon decay rate. The operators $a_{\rm in}$ and $a_{\rm int}$ represents the input and internal quantum vacuum noises, respectively, and the operator ξ refers to the mechanical noise due to Brownian motion. They obey the following two-time correlation relations

$$\begin{aligned} \langle a_{\rm in}(t) a_{\rm in}^\dagger(t') \rangle &= \delta(t - t'), \qquad \langle a_{\rm in}^\dagger(t) a_{\rm in}(t') \rangle = 0, \\ \langle a_{\rm int}(t) a_{\rm int}^\dagger(t') \rangle &= \delta(t - t'), \qquad \langle a_{\rm int}^\dagger(t) a_{\rm int}(t') \rangle = 0, \\ \langle \xi(t) \xi(t') \rangle &= \frac{1}{2\pi} \frac{\gamma_m}{\omega_m} \int \omega e^{-i\omega(t-t')} [1 + \coth(\frac{\hbar\omega}{2K_B T})] {\rm d}\omega, \end{aligned} \tag{1.8}$$

where K_B is the Boltzmann constant. However, one has to bear in mind that the Brownian noise is a Gaussian stochastic force which describes a non-Markovian

[2] In many papers including Refs. [5, 43], the cavity energy (photon) decay rate is denoted as κ and hence the cavity field (amplitude) decay rate shall be $\kappa/2$.

stochastic process. It reduces to a Markovian description in two different limits [44]: (i) a finite bath temperature $K_BT/\hbar\omega_m \gg 1$, which is satisfied for typical OMS experimental parameters even at cryogenic temperatures; (ii) a high mechanical quality factor $\omega_m/\gamma_m \to \infty$, which is realized in most OMS to demonstrate the quantum effects. In these limits, the time correlation function for $\xi(t)$ reduces to a Dirac delta function form

$$\langle \xi(t)\xi(t')\rangle = \gamma_m(2\bar{n}_{\rm th}+1)\delta(t-t'), \tag{1.9}$$

where $\bar{n}_{\rm th} = [\exp(\hbar\omega_m/K_BT)-1)]^{-1}$ is the mean thermal phonon number at temperature T.

We solve the set of nonlinear equations (1.7) by expanding the operators P, Q and a to first order, so that $P \equiv P_0 + P_1$, $Q \equiv Q_0 + Q_1$ and $a \equiv a_0 + a_1$. We essentially separate the steady state of the system (denoted by c-numbers with subscript 0) from the fluctuations (denoted by operators with subscript 1). For the classical mean values we ignore the nonzero commutators using the mean field approximation and also ignore the quantum fluctuations. Then we obtain

$$P_0 = 0, \qquad Q_0 = \frac{\sqrt{2}g}{\omega_m}|a_0|^2, \qquad \text{and} \qquad a_0 = \frac{\mathcal{E}_l}{\kappa + i\Delta}, \tag{1.10}$$

where

$$\Delta = \omega_c - \omega_l - \sqrt{2}gQ_0 \tag{1.11}$$

denotes the detuning of the driving laser frequency to the effective cavity resonance frequency under radiation pressure. We can interpret $|a_0|^2$ as the mean cavity photon number $\bar{n}$, *i.e.* $|a_0|^2 = \bar{n}$. The steady state solution of the mechanical oscillator can be interpreted as the balance of the radiation pressure force $F_{\rm rad} = \hbar\omega_c|a_0|^2/L = \hbar g|a_0|^2/q_{\rm zpf}$ and the mechanical restoring force $F_{\rm res} = -m\omega_m^2 q = -m\omega_m^2 q_{\rm zpf}\sqrt{2}Q_0$. If we solve the equation $F_{\rm rad} + F_{\rm res} = 0$, we can immediately get $Q_0 = \frac{\sqrt{2}\hbar g|a_0|^2}{m\omega_m^2 q_{\rm zpf}^2} = \sqrt{2}g|a_0|^2/\omega_m$. In absence of the driving laser $\mathcal{E}_l \to 0$, the steady state solution $a_0 \to 0$ and $Q_0 \to 0$. When we apply a weak driving field, the mean cavity field amplitude a_0

increases, and consequently the increasing radiation pressure enhances the mechanical displacement Q_0. A larger mirror displacement Q_0 reduces the effective cavity resonance frequency $\omega_c - \sqrt{2}gQ_0$ which further results in a change of the effective driving laser detuning Δ. If the driving laser is red detuned ($\omega_c < \omega_l$), Δ deceases which causes an increase of the intracavity field amplitude $|a_0|^2$ and hence an increase of the radiation pressure force $F_{\rm rad}$. If $F_{\rm rad}$ increases faster than $F_{\rm res}$ at a large driving amplitude, we may observe an optomechanical bistability phenomenon [45–47].

After the expansion, the equations of motion for the first order fluctuations take the form

$$\begin{cases} \dot{Q}_1 = \omega_m P_1, \\ \dot{P}_1 = -\omega_m Q_1 + \sqrt{2}g(a_0^* a_1 + a_0 a^\dagger) - \gamma_m P_1 + \xi, \\ \dot{a}_1 = -i\Delta a_1 - \kappa a_1 + i\sqrt{2}g a_0 Q_1 + \sqrt{2\kappa_e}a_{\rm in} + \sqrt{2\kappa_i}a_{\rm int}, \end{cases} \tag{1.12}$$

In terms of photon and phonon annihilation operators a and b, the nonlinear quantum Langevin equations take the form

$$\begin{cases} \dot{a}_1 = -i\Delta a_1 - \kappa a_1 + i a_0 g(b_1 + b_1^\dagger) + \sqrt{2\kappa_e}a_{\rm in} + \sqrt{2\kappa_i}a_{\rm int}, \\ \dot{b}_1 = -i\omega_m b_1 - (\gamma_m/2)b_1 + ig(a_0 a_1^\dagger + a_0^* a_1) + f_{\rm in}, \end{cases} \tag{1.13}$$

where the operator $f_{\rm in}$ is related to ξ and it has the two-time correlation

$$\begin{aligned} \langle f_{\rm in}(t) f_{\rm in}^\dagger(t')\rangle &= \gamma_m(\bar{n}_{\rm th} + 1)\delta(t - t'), \\ \langle f_{\rm in}^\dagger(t) f_{\rm in}(t')\rangle &= \gamma_m \bar{n}_{\rm th}\delta(t - t'). \end{aligned} \tag{1.14}$$

Since a_0 is always multiplied to g, we can define an driving laser enhanced optomechanical coupling rate $G = a_0 g$ for the sake of a convenient notation. Cooperativity $C = \frac{2|G|^2}{\kappa\gamma_m}$ is another commonly used parameter to describe the optomechanical coupling strength compared with the dissipation rates.

1.3 Input-output relation

We can see from Eqs. (1.7) that the input fields include the driving field $\mathcal{E}_l$ and quantum fluctuation $a_{\rm in}$. The output fields should also conclude two components:

the classical output field $\mathcal{E}_{\rm out}$ and quantum fluctuation $a_{\rm out}$. These quantities are related by the input-output relation [48]

$$a_{\rm in} + \frac{\mathcal{E}_l}{\sqrt{2\kappa_e}} + a_{\rm out} + \frac{\mathcal{E}_{\rm out}}{\sqrt{2\kappa_e}} = \sqrt{2\kappa_e}a, \tag{1.15}$$

where a denotes the intra-cavity field which has multiple components in different frequencies. Very often we also apply a coherent but weak probe beam to the OMS, then one more term $\mathcal{E}_p/\sqrt{2\kappa_e}$ should be appended on the left hand side of Eq. (1.15).

As an example, we examine the cavity output field in response to a single input laser $\mathcal{E}_l$. We assume the laser frequency is on resonance with the cavity frequency, *i.e.* $\Delta = 0$. The quantum fluctuations can be ignored in the classical steady-state limit. Hence we obtain the output field by combining Eqs. (1.15) and (1.10)

$$\mathcal{E}_{\rm out} = 2\kappa_e\frac{\mathcal{E}_l}{\kappa} - \mathcal{E}_l = (2\eta - 1)\mathcal{E}_l, \tag{1.16}$$

where $\eta = \kappa_e/\kappa$ denotes the output coupling ratio. When $\eta = 1/2$, the so-called critical coupling regime is achieved so that the resulting output field goes to zero on resonance. This also refers to be the impedance matching condition in which the internal resonator loss (κ_i) and input-output coupling rate (κ_e) are equal. This limit is advantageous especially in the classical regime in the sense that the input laser couples into the cavity at the maximum rate and any output field directly reflects the field generated from optomechanical interaction. On contrary, any internal loss is supposed to be avoided in the quantum regime because the internal photon decay results in inaccessible channels and quantum correlation is partially lost. This places a serious limit on the optomechanical applications. We will show in later sections that the internal loss degrades the quantum squeezing magnitude.

1.4 Stability criteria

Before we continue to calculate the first order fluctuations a_1 and b_1, we must ensure the stability of the steady state solution (1.10). A small perturbation around a stable

steady state always damps while it grows in an unstable steady state. We note that Eqs. (1.13) can be written in the matrix form

$$\dot{\Phi}(t) = \mathbb{M}\Phi(t) + \mathbb{D}(t), \tag{1.17}$$

where $\Phi = (a_1, a_1^\dagger, b_1, b_1^\dagger)^T$ is the vector of the state operators and $\mathbb{D} = (\sqrt{2\kappa}a_{\rm in}, \sqrt{2\kappa}a_{\rm in}^\dagger, f_{\rm in}, f_{\rm in}^\dagger)^T$ is the vector of optical and mechanical noise inputs. The coefficient matrix $\mathbb{M}$ governs the evolution of the state vector and it reads

$$\mathbb{M} = -\begin{pmatrix} \kappa + i\Delta & 0 & -iG & -iG \\ 0 & \kappa - i\Delta & iG & iG \\ -iG^* & -iG & \gamma_m/2 + i\omega_m & 0 \\ iG^* & iG & 0 & \gamma_m/2 - i\omega_m \end{pmatrix}. \tag{1.18}$$

The necessary and sufficient condition of stability requires that each eigenvalue of matrix M has only negative real part. This can be examined by applying the Routh-Hurwitz criterion to the polynomial of its eigenvalues

$$\mathrm{Det}(\mathbb{M} - \lambda\mathbb{1}) = \lambda^4 + h_1\lambda^3 + h_2\lambda^2 + h_3\lambda + h_4. \tag{1.19}$$

After expanding the determinant $\mathrm{Det}(\mathbb{M} - \lambda\mathbb{1})$ for (1.17), we find that

$$\begin{aligned} h_1 &= 2\kappa + \gamma_m, \\ h_2 &= \kappa^2 + \Delta^2 + (\gamma_m/2)^2 + \omega_m^2 + 2\kappa\gamma_m, \\ h_3 &= 2\kappa[(\gamma_m/2)^2 + \omega_m^2] + \gamma_m(\kappa^2 + \Delta^2), \\ h_4 &= (\kappa^2 + \Delta^2)[(\gamma_m/2)^2 + \omega_m^2] - 2\Delta\omega_m|G|^2. \end{aligned} \tag{1.20}$$

Routh-Hurwitz criterion reads that all of the eigenvalues have a negative real part if and only if

- all the coefficients $h_i > 0$;
- *and* the determinants of all of the Hurwitz matrices $|H_i|$ are positive, where the

the Hurwitz matrices are defined as

$$H_1 = |h_1|, \qquad H_2 = \begin{pmatrix} h_1 & 1 \\ h_3 & h_2 \end{pmatrix}, \qquad H_3 = \begin{pmatrix} h_1 & 1 & 0 \\ h_3 & h_2 & h_1 \\ 0 & h_4 & h_3 \end{pmatrix}. \tag{1.21}$$

These criteria applied to our system results in the stability condition given as

$$2\Delta\omega_m|G|^2 < (\kappa^2+\Delta^2)[(\frac{\gamma_m}{2})^2+\omega_m^2], \tag{1.22}$$

$$2\Delta\omega_m|G|^2 > -2\kappa\gamma_m\left(\frac{2\kappa[(\frac{\gamma_m}{2})^2+\omega_m^2]+\gamma_m(\kappa^2+\Delta^2)}{2\kappa+\gamma_m}+\frac{[(\frac{\gamma_m}{2})^2+\omega_m^2-\kappa^2-\Delta^2]^2}{(2\kappa+\gamma_m)^2}\right). \tag{1.23}$$

We can see that for given driving laser detuning, only one of the criteria sets a limit to the driving amplitude, *i.e.* if the driving laser is red detuned ($\Delta < 0$) then (1.22) is the only condition; if the driving laser is blue detuned ($\Delta > 0$) then (1.23) is the only condition. In a typical OMS, the mechanical damping is usually negligibly small compared to other rates, $\gamma_m \to 0$, and hence condition (1.23) indicates that the OMS can easily settle into instability [49–51] under a blue detuned driving laser at relatively low power levels.

1.5 Outline of this dissertation

This dissertation aims at exploring the coherent interference effects in single- and double-cavity OMS as well as its possibility of generating significant amount of squeezed light. In the current chapter, I have explained the the basis of the theoretical model of a single-cavity OMS by deriving the Hamiltonian and Heisenberg equations of motion. The standard linearization procedure yields the equations for optical and mechanical fluctuations. Furthermore, I have shown the derivation of the stability condition based on the Routh-Hurwitz criterion.

Chapter 2 incorporates material from my publication [43] and submission [52]. I begin with introducing the EIT effect as well as its transient behavior in OMS by

using the coherent photon-phonon interaction processes. Based on this mechanism, I propose the use of a cavity OMS to achieve the storage and retrieval of optical pulses. Then, I adopt Ramsey's method of separated oscillatory fields to study coherences of the mechanical system in an optomechanical resonator. I develop a theory to describe the transient optomechanical behavior underlying the Ramsey fringes. By collaborating with experimental groups, we also perform the experimental demonstration using a silica microresonator.

Chapter 3 incorporates material from my publications [53, 54] and submission [52]. I predict in the double-cavity OMS the existence of the electromagnetically induced absorption (EIA), in which an absorption peak arises within the EIT window. I provide analytical results for the width and the height of the EIA peak. I then explain how this EIA effect can be generalized to different systems that can be described using three-coupled-oscillator model and how it was successfully demonstrated in metamaterials by collaborating with experimental groups. In the last section, I show how double-cavity OMS enables us to achieve the transduction process to several frequencies including, in principle, the possibility of transduction from optical to microwave frequencies.

Chapter 4 incorporates material from my publication [55]. I demonstrate the existence of Fano resonances in cavity optomechanics by identifying the interfering contributions to the fields generated at anti-Stokes and Stokes frequencies. I show the flexibility of the Fano resonance in OMS in contrast to atomic systems, as the width of the resonance is controlled by the coupling field. I further show how the double cavities coupled by a single optomechanical mirror can lead to the splitting of the Fano resonance and how the second cavity can be used to tune the Fano resonances. Such resonances can be studied by both pump probe experiments as well as via the spectrum of the quantum fluctuations of the output fields.

Chapter 5 incorporates material from my publication [56]. I propose a scheme for

generating squeezed light by using a double-cavity optomechanical system driven by a blue detuned laser in one cavity and by a red detuned laser in the other. I show that squeezing of the output fields, of the order of 10dB, can be achieved even for an effective mechanical mode occupation number of about 4 which for the chosen parameters corresponds to 10mK. I further describe such photon pair generation through an effective interaction which generally is used for generating squeezing using parametric downconversion and four-wave mixing.

Chapter 6 incorporates material from my publication [57]. I study a novel optomechanical interaction, namely, dissipative optomechanical coupling in which the mechanical displacement modulates the cavity decay rate, instead of resonance frequency. This is based on a recent demonstration of cooling of a macroscopic silicon nitride membrane placed in an interferometer. I theoretically show that such a system in a cavity can yield good squeezing, which is comparable to that produced by dispersive coupling. I also report the squeezing resulting from the combined effects of dispersive and dissipative couplings; thus the device can be operated in one regime or the other.

Chapter 7, I present the conclusions and the outlook for the field of optomechanics.

CHAPTER 2

OPTICAL MEMORY AND OPTOMECHANICAL RAMSEY INTERFEROMETRY

In the previous chapter, I presented the theoretical model of a single-cavity optomechanical system. The equations of motion for the OMS concentrate on the quantum dynamics of the coupled optical and mechanical state subject to quantum vacuum input noise and mechanical Brownian noise. This description is useful and important when analyzing quantum effects *e.g.* quantum ground state cooling, entangled photon pair preparation, quantum nondemolition detection, and etc in OMS. In 2010, Agarwal and Huang [58] for the first time studied the coherence effect in a cavity optomechanical system by introducing a weak probe laser in conjunction with an input field with a strong driving laser. Within such an optomechanical configuration, they were able to show a phenomenon analogous to the Electromagnetically Induced Transparency (EIT) in an atomic system based on the coherent photon-phonon coupling aided by the driving laser. Their proposal was almost immediately verified in various experimental setups [59–61] with excellent agreements. This study opened a whole new avenue of studying optomechanical effects based on coherence effects. Since then, several other theoretical proposals [53, 55, 62–65] and experimental demonstrations [66–68] have been reported.

In this chapter, I begin with a brief introduction of EIT and explain the transient behavior in a standard OMS. Then I make use of this mechanism and propose the applications to optical memories and transduction of electromagnetic fields. I will show that coherent interaction between the optical and mechanical modes al-

lows storage of light as mechanical excitations by applying a pair of "write" driving pulse and a probe pulse. This excitation can be retrieved as optical pulses after some storage time by applying a "read" driving pulse. In the latter part of this chapter, I will present my study of the Optomechanical Ramsey Interferometer which studies coherence of the mechanical system using two separated oscillatory fields. The high-resolution Ramsey fringes can be observed in the emission optical field, when two pulses separated in time are applied. For this study, I develop a theory and solve for the analytical expressions of the optomechanical states. By collaborating with experimental groups, we also perform the experimental demonstration of the optomechanical Ramsey interferometer using a silica microresonator.

2.1 Transient Electromagnetically Induced Transparency in OMS

The Electromagnetically Induced Transparency (EIT), in which the driving laser induces a narrow spectral transparency window for a probe laser, is a prominent example of utilizing quantum interference in different excitation pathways aided by coherent interaction of laser radiation. This peculiar mechanism applies to both classical coherent light and quantum state of light, which ensures a large number of applications ranging from optical storage to slowing down or advancing the speed of light. Its relevance to nonlinear optics and quantum information processing (QIP) has thrust EIT in OMS to the forefront of theoretical and experimental study during the past five years.

We first briefly review the EIT in optomechanics; a full derivation can be found in the theoretical study by Huang and Agarwal [58]. The optomechanical interaction among different frequency components is illustrated in Fig. 2.1a. A strong driving laser oscillating at frequency ω_l couples the cavity optical mode ω_c and the mechanical phonon mode ω_m. A phonon is removed upon the addition of a driving photon to the intra-cavity field which decays out of the cavity very fast. A second very weak

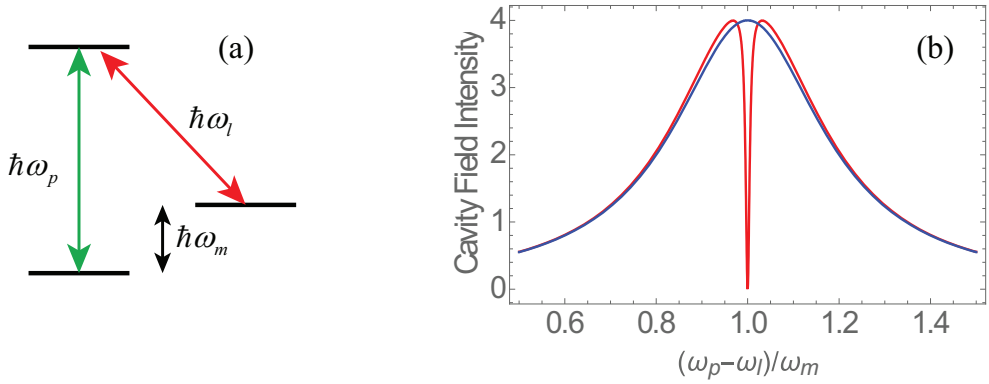

Figure 2.1: Electromagnetically Induced Transparency in OMS: (a) the energy level diagram, and (b) the intra-cavity field intensity with (red) and without (blue) the driving laser.

laser oscillating at ω_p at the vicinity of cavity resonance frequency ω_c probes the cavity optomechanical system. Due to the strong optomechanical coupling induced by the driving laser, it effectively interacts with a hybrid optomechanical resonance. This hybridization opens up a tunable transmission window for the probe laser at the center of the optical resonance. Therefore, this effect is also named "optomechanically induced transparency".

Next, we provide a short derivation of EIT using the standard theoretical model of OMS. In an OMS, which couples an optical mode a and a mechanical mode b, the time evolution of the system operators is governed by the coupled equations

$$\begin{aligned} \dot{a} &= -i(\omega_p - \omega_l)a + iG^*b - \kappa a + \mathcal{E}_p, \\ \dot{b} &= -i\omega_m b + iGa - (\gamma_m/2)b. \end{aligned} \tag{2.1}$$

Note that we are interested in the optomechanical response to a coherent probe laser beam and we ignore quantum fluctuations, hence the operators a and b in this chapter actually refer to their mean values, *i.e.* $a \equiv \langle a \rangle$ and $b \equiv \langle b \rangle$. We solve Eqs. (2.1) by taking the Fourier transform $A(t) = \frac{1}{2\pi}\int A(\omega)e^{-i\omega t}\mathrm{d}\omega$. We find that under the red-detuned driving condition $\omega_l + \omega_m = \omega_c$ the intra-cavity field $\mathcal{E}_c$ normalized to

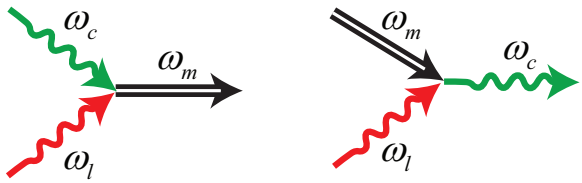

Figure 2.2: Left: the driving photon at frequency (ω_l) combining with a cavity photon ($\omega_c = \omega_p$) generates a phonon (ω_m); Right: the driving photon combining with a phonon generates a cavity photon.

the probe amplitude $\mathcal{E}_p$ is

$$\mathcal{E}_c = 2\kappa\langle a\rangle = \frac{2i\kappa\mathcal{E}_p}{(\omega_p - \omega_c + i\kappa) - \dfrac{|G|^2}{\omega_p - \omega_c + i\gamma_m/2}}. \tag{2.2}$$

This is the standard form of EIT transmission under a driving field. When the probe field is on resonance, the intra-cavity field is strongly dependent on the driving laser intensity. With large G, the intra-cavity field amplitude is suppressed. As shown in Fig. 2.1(b), we observe that the narrow contribution with an EIT width $\Gamma_{\mathrm{EIT}} = \frac{|G|^2}{\kappa} + \frac{\gamma_m}{2}$ is inverted relative to the broad Lorentzian profile.

Physically, the transparency window in EIT arises from the interference of two paths constructing the optical field in the cavity. Under the strong pump at ω_l, the probe field at ω_p beats with the driving field and excites the mechanical oscillation at frequency ω_m. This process is resonantly enhanced if $\omega_p - \omega_l = \omega_m$. In the quantum language, a probe photon and a driving photon combine to generate a phonon, as illustrated in Fig. 2.2. Once the phonon mode is built up, it combines with the driving photon to create a probe photon, as illustrated in Fig. 2.2. Therefore, the intra-cavity field, on one hand, comes from the input probe field; and on the other hand, comes from the photon-phonon-photon conversion process. These two processes interfere destructively to suppress the intra-cavity field, which leads to the EIT window due to optomechanical interaction.

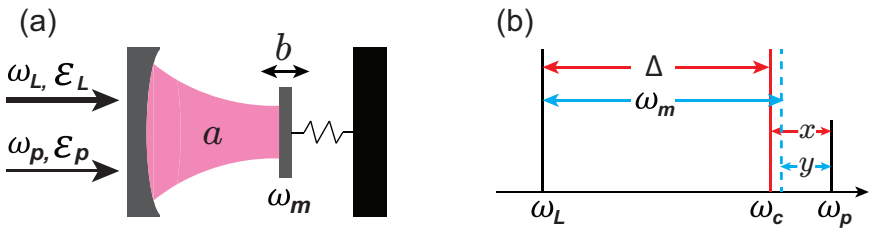

Figure 2.3: (a) Sketch of the OMS. (b)The frequency relations of different modes in OMS: the left mode is the driving laser in ω_l, the middle short one is the probe laser in ω_p, the right solid one is the cavity mode in ω_c and the dashed one is the anti-Stokes generation of the driving laser in $\omega_l + \omega_m$. x is the detuning between probe and the cavity modes, and y is between the probe and the anti-Stokes modes.

In order to fully understand EIT in OMS, let us study the transient EIT behavior. We start from the Heisenberg equations of motion of a time-dependent driving and probe fields in the frame rotating at the driving laser frequency

$$\begin{aligned} \dot{a} &= -i(\omega_c - \omega_l)a + iga(b + b^\dagger) - \kappa a + \mathcal{E}_l(t) + \mathcal{E}_p(t)\mathrm{e}^{-i(\omega_p - \omega_l)t} \\ \dot{b} &= -i\omega_m b + iga^\dagger a - (\gamma_m/2)b, \end{aligned} \tag{2.3}$$

assuming the change of laser beam amplitude is slow compared with any other decay or interaction. We consider the initial state of the cavity to be empty and $a(0) = b(0) = 0$. At time $t = 0$, we start to apply a constant strong driving laser and a weak probe laser into the cavity. As the laser beams are applied, the mean value of the intra-cavity field increases and approaches a constant which is determined by the decaying rate and the input. This process happens at a time scale of $1/\kappa$. At the same time when the cavity is fed with an optical field, it interacts with the mechanical mode. More specifically, the driving laser produces two side bands $\omega_l \pm \omega_m$ due to the scattering effect of the oscillating mirror. If the cavity resonance frequency overlaps with either one of the side bands, the frequency mixing process is enhanced. We expand the states to the first order using $a = a_0 + a_1\mathrm{e}^{-i(\omega_p - \omega_l)t}$ and $b = b_0 + b_1\mathrm{e}^{-i(\omega_p - \omega_l)t}$, where the zeroth order a_0 and b_0 denote their steady-state mean values. Since the

mean values approach the steady state rapidly, we ignore the process for the lasers to feed up the cavity and calculate the mean values by setting their time derivatives to zero and adding the damping terms,

$$\begin{aligned} 0 = \dot{a}_0 &= -i(\omega_c - \omega_l)a_0 + iga_0(b_0 + b_0^*) - \kappa a_0 + \mathcal{E}_l(t) \\ 0 = \dot{b}_0 &= -i\omega_m b_0 + ig|a_0|^2. \end{aligned} \tag{2.4}$$

Thus we can get the solution

$$a_0(t) = \frac{\mathcal{E}_l(t)}{\kappa + i\Delta} \qquad \text{and} \qquad b_0(t) = \frac{g}{\omega_m}|a_0(t)|^2, \tag{2.5}$$

where $\Delta = \omega_c - \omega_l - 2|a_0|^2 g^2/\omega_m$ denoting the effective detuning of the cavity frequency and the driving field. The first orders obey the differential equations

$$\begin{aligned} \dot{a}_1 &= -i(\Delta - \omega_p + \omega_L)a_1 - iG(t)(b_1 + b_1^\dagger e^{2i(\omega_p - \omega_L)t}) - \kappa a_1 + \mathcal{E}_p \\ \dot{b}_1 &= -i(\omega_m - \omega_p + \omega_L)b_1 - i(G^*(t)a_1 + G(t)a_1^\dagger e^{2i(\omega_p - \omega_L)t}) - (\gamma_m/2)b_1. \end{aligned} \tag{2.6}$$

In the resolved sideband regime, $\Delta \gg \kappa$, the exponential $e^{2i(\omega_p - \omega_L)t}$ becomes fast oscillating and we can ignore the counter rotating terms $b_1^\dagger$ and $a_1^\dagger$. We define two small frequency parameters: $x = \omega_p - \omega_l - \Delta$ as the detuning between the probe field and the cavity mode and $y = \omega_p - \omega_l - \omega_m$ as the detuning between the probe field and the anti-Stokes side band of the driving laser scattered by the mechanical mode. In order to achieve a large coupling rate, they are both chosen close to 0. We illustrate the frequency relations in Fig. 2.3(b). Then Eq. (2.6) can be written as

$$\begin{aligned} \dot{a}_1 &= ixa_1 + iG(t)b_1 - \kappa a_1 + \mathcal{E}_p(t) \\ \dot{b}_1 &= iyb_1 + iG^*(t)a_1 - (\gamma_m/2)b_1, \end{aligned} \tag{2.7}$$

where $G(t) = \alpha(t)g$ is the time-dependent driving-enhanced coupling rate. The output optical field at frequency ω_p and any time t can be derived from the input-output relation $\mathcal{E}_{\text{out}}(t) + \mathcal{E}_p(t) = 2\kappa a(t)$. Then the output field would be

$$\mathcal{E}_{\text{out}}(t) = 2\kappa[a_0(t)\mathrm{e}^{i(\omega_p - \omega_l)t} + a_1(t) + a_1^\dagger(t)\mathrm{e}^{2i(\omega_p - \omega_l)t}] - \mathcal{E}_p(t) - \mathcal{E}_l(t)\mathrm{e}^{i(\omega_p - \omega_l)t}. \tag{2.8}$$

The expression contains the optical fields in the driving frequency and its two sidebands. In our study, we are especially interested in the component in the probe laser frequency given by $\mathcal{E}_{\text{pout}}(t) = 2\kappa a_1(t) - \mathcal{E}_p(t)$.

The steady-state solutions to Eqs.(2.7) are well studied in the context of EIT in OMS. We are now interested in its transient behavior and study its dynamical evolution. During the process when the lasers are applied, the system is governed by differential equations (2.7), which can be written in the matrix form

$$\dot{\Psi}(t) = \mathbb{M}\Psi(t) + \mathbb{D}(t), \tag{2.9}$$

where $\Psi(t) = (a_1 \quad b_1)^T$, $\mathbb{D}(t) = (\mathcal{E}_p(t) \quad 0)^T$, and

$$\mathbb{M} = -\begin{pmatrix} \kappa - ix & -iG(t) \\ -iG^*(t) & \gamma_m/2 - iy \end{pmatrix}. \tag{2.10}$$

The matrix differential Eq.(2.9) which describes the evolution of the system between times t_1 and t_2 can be solved as

$$\Psi(t_2) = \mathrm{e}^{\mathbb{M}(t_2-t_1)}\Psi(t_1) + \int_{t_1}^{t_2} \mathrm{e}^{\mathbb{M}(t_2-t')} D(t')\mathrm{d}t'. \tag{2.11}$$

We assume initially the amplitudes of both the optical and mechanical modes to be zero, i.e. $\Psi(0) = 0$. The driving and probe lasers are applied at constant amplitudes respectively starting at $t = 0$. Then the integral can be carried out by using the knowledge that $\mathbb{D}(t)$ is a constant for $0 < t < \tau$. Let $\Psi_s \equiv \Psi(\tau)$ be the fields after the application of the input beams for a time τ; then it can be calculated as

$$\Psi_s(\tau) = \mathbb{M}^{-1}(\mathrm{e}^{\mathbb{M}\tau} - \mathbb{1})\mathbb{D}, \tag{2.12}$$

where $\mathbb{D} = (\mathcal{E}_p \quad 0)^T$. To explicitly calculate the optical and mechanical fields given in Eq.(2.12), we expand $\mathrm{e}^{\mathbb{M}\tau} = S\,\mathbf{diag}(\mathrm{e}^{\lambda_+\tau} \quad \mathrm{e}^{\lambda_-\tau})S^{-1}$ where S is determined by $\mathbb{M} = S\Lambda S^{-1}$, $\Lambda = \mathbf{diag}(\lambda_+ \quad \lambda_-)$ and $\lambda_\pm$ are the eigenvalues of $\mathbb{M}$. The full expression

of Ψ_s can be calculated after some lengthy algebra

$$\Psi_s(\tau) = \begin{pmatrix} (\mathbb{M}^{-1})_{11}[(\mathrm{e}^{\mathbb{M}\tau})_{11} - 1] + (\mathbb{M}^{-1})_{12}(\mathrm{e}^{\mathbb{M}\tau})_{21} \\ (\mathbb{M}^{-1})_{21}(\mathrm{e}^{\mathbb{M}\tau})_{11} + (\mathbb{M}^{-1})_{22}[(\mathrm{e}^{\mathbb{M}\tau})_{21} - 1] \end{pmatrix} \mathcal{E}_p$$

$$= \begin{pmatrix} \frac{(\gamma_m/2-iy)(\lambda_- - \lambda_+) + (|G|^2 - (\kappa+\lambda_+ - ix)(\gamma_m/2-iy))\mathrm{e}^{\lambda_- \tau}}{[|G|^2 + (\kappa - ix)(\gamma_m/2-iy)](\lambda_- - \lambda_+)} \\ \frac{iG^*[\lambda_- + \lambda_+(\mathrm{e}^{\lambda_- \tau} - 1)]}{[|G|^2 + (\kappa - ix)(\gamma_m/2-iy)](\lambda_- - \lambda_+)} \end{pmatrix} \mathcal{E}_p, \tag{2.13}$$

where $(..)_{ij}$ denotes the element in the ith row and jth column of a matrix.

Next we simplify the expression by making approximations within the typical OMS parameters. The eigenvalues are

$$\begin{aligned} \lambda_+ &\approx ix - \kappa + |G|^2/\kappa, \\ \lambda_- &\approx iy - \gamma_m/2 - |G|^2/\kappa = iy - \Gamma_{\mathrm{EIT}}. \end{aligned} \tag{2.14}$$

Then

$$\begin{aligned} \mathbb{M}^{-1} &= \frac{1}{|G|^2 + (\kappa - ix)(\gamma_m/2 - iy)} \begin{pmatrix} -\gamma_m/2 + iy & -iG \\ -iG^* & -\kappa + ix \end{pmatrix} \\ &\approx \frac{1}{\kappa(\Gamma_{\mathrm{EIT}} - iy)} \begin{pmatrix} -\gamma_m/2 + iy & -iG \\ -iG^* & -\kappa + ix \end{pmatrix}, \end{aligned} \tag{2.15}$$

and

$$\begin{aligned} e^{\mathbb{M}\tau} &= \frac{e^{\lambda_+\tau} - e^{\lambda_-\tau}}{\lambda_+ - \lambda_-}\mathbb{M} + \frac{-\lambda_+ e^{\lambda_+\tau} + \lambda_- e^{\lambda_-\tau}}{\lambda_+ - \lambda_-}\mathbb{1} \\ &\approx \frac{e^{\lambda_-\tau}}{\lambda_+ - \lambda_-} \begin{pmatrix} \kappa - ix + \lambda_+ & -iG \\ -iG^* & \gamma_m/2 - iy + \lambda_+ \end{pmatrix}. \end{aligned} \tag{2.16}$$

In the last step, we dropped the term proportional to $e^{\lambda_+\tau}$ which is a very good approximation. Also note that the real part of λ_- denotes the linewidth of the EIT window Γ_{EIT} in the steady state. Previous study shows that the coupling between the optical mode and mechanical mode is the strongest when $\Delta = \omega_m$ (*i.e.* $x = y$);

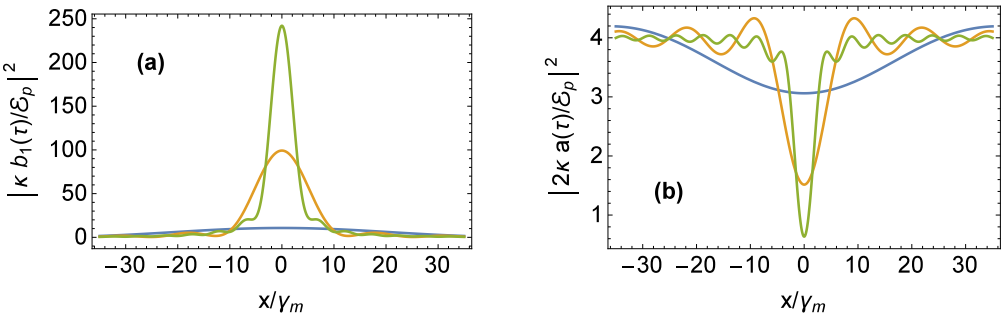

Figure 2.4: The mechanical field (a) and intra-cavity optical field (b) after different interaction times $\tau = 1\mu$s (blue curve), 4μs (orange curve) and 10μs (green curve). The parameters for the OMS are $\kappa/2\pi = 15$MHz, $|G|/2\pi = 0.58$MHz, $\gamma_m/2\pi = 0.02$MHz and the corresponding EIT width for the steady state is $\Gamma_{\rm EIT} = 1.6\gamma_m$. We also set $x = y$.

hence, we study the scenario $x,\, y \sim 0$. In the limit of $\kappa \gg \Gamma_{\rm EIT}$ and $\kappa \gg |G|$, we can make the approximation $\lambda_+ - \lambda_- \approx -\kappa$, so that (2.16) further simplifies to

$$e^{\mathbb{M}\tau} \approx \frac{-e^{-(\Gamma_{\rm EIT}+iy)\tau}}{\kappa} \begin{pmatrix} |G|^2/\kappa & -iG \\ -iG^* & -\kappa + \Gamma_{\rm EIT} \end{pmatrix}. \tag{2.17}$$

Thus we obtain $\Psi_s(\tau)$ after applying the driving and probe lasers

$$\Psi_s(\tau) \approx \frac{1}{\kappa(\Gamma_{\rm EIT} - iy)} \begin{pmatrix} \gamma_m/2 - iy + \frac{|G|^2}{\kappa} e^{\lambda_- \tau} \\ -iG^*(e^{\lambda_- \tau} - 1) \end{pmatrix} \mathcal{E}_p. \tag{2.18}$$

The intra-cavity optical field $\mathcal{E}_c(\tau)$ around $y \sim 0$ is

$$\mathcal{E}_c(\tau) = 2\kappa a_1(\tau) \approx 2\left[1 + \frac{|G|^2}{\kappa} \frac{e^{-(\Gamma_{\rm EIT}-iy)\tau} - 1}{\Gamma_{\rm EIT} - iy}\right] \mathcal{E}_p. \tag{2.19}$$

The mechanical mode can be calculated as

$$\kappa b_1(\tau) \approx iG^* \frac{e^{-(\Gamma_{\rm EIT}-iy)\tau} - 1}{\Gamma_{\rm EIT} - iy} \mathcal{E}_p. \tag{2.20}$$

We illustrate in Fig. 2.4 the mechanical mode and optical mode intensities after interaction time τ. We can see Eq.(2.19) contains two terms implying that the intra-cavity optical field has two contributions. The first term $\mathcal{E}_p$ denotes the direct optical

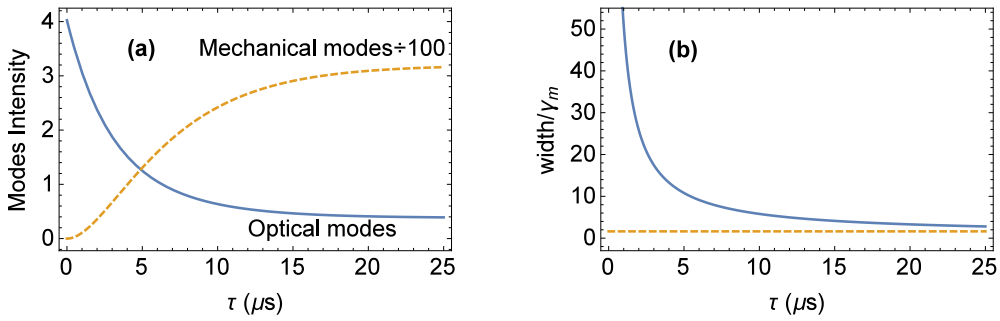

Figure 2.5: (a) The in-cavity optical mode (solid curve): $|\kappa b_2(\tau)/\mathcal{E}_{p1}|^2$ and mechanical mode (dashed curve): $|2\kappa a_2(\tau)/\mathcal{E}_{p1}|^2$ after different interaction time τ. (b) Widths of the EIT window in the output optical field after different interaction time τ. The dashed curve shows the asymptotic width $\Gamma_{\rm EIT}$ for steady states. The parameters are the same as in Fig. 2.4.

input field. The second term corresponds to the anti-Stokes scattering of the driving field at frequency ω_l by combining with a phonon with frequency ω_m. Its numerator also justifies that EIT is only prominent when $e^{\lambda_- \tau} \to 0$, which sets the characteristic time of EIT in OMS, i.e. $|\lambda_- \tau| > 1$. Physically, when the driving laser and the probe laser are sent to the cavity, they combine and produce mechanical phonons. Then the phonons combine with the driving laser and generate the anti-Stokes sideband which interferes with the input probe field leading to EIT. This process is illustrated in Fig. 2.5(a). Under constant driving and probe fields input, the degree of EIT is constrained by the phonon intensity, which increases with time before it saturates, as shown in Fig. 2.4(a). Consequently, the optical mode intensity in the cavity decreases with time and approaches zero. In this way, we can explain the characteristic time for the establishment of EIT. Wang *et al.* have also experimentally confirmed the same characteristic time.

In Fig. 2.5(b), we plot the widths of the EIT window in the intra-cavity optical field with different interaction time τ. For very small interaction time τ, the output field can be approximated as $2\kappa a_1(\tau) \sim 2\left[1 - (|G|^2/\kappa)\tau \mathrm{sinc}(y\tau)\right]\mathcal{E}_p$, and $|2\kappa a_1(\tau)|^2$

has a width $2\pi/\tau$. As τ increases, the EIT window gets narrower and approaches $\Gamma_{\rm EIT}$. Especially when τ is longer than the characteristic time $1/\Gamma_{\rm EIT} \approx 4.9\mu$s, the width of the EIT window becomes narrower than $10\gamma_m$.

2.2 Optical memory

The design of a good optical memory [69–71] depends very much on the underlying physical process as well as the system used to construct the memory. One needs the systems or storage elements with very long coherence times. Electromagnetically induced transparency (EIT) [58–61] has become an important physical mechanism to construct optical memories [72–76]. For example, the optical pulses can be stored in atomic coherences among long lived states. Many experiments have demonstrated the working of optical memories using typically atomic vapors. Optomechanical systems also have very long coherence times and hence one has the possibility of using such systems as optical memories as information is stored in coherent phonons. We have seen that one has an exact analog of EIT in OMS. Further phonons are generated coherently — this being the analog of atomic coherence in vapors. Thus, EIT in OMS along with the long coherence time for the generated phonons can be used for making optical memories.

In the last section, we studied the process of converting photons into phonons when a driving laser is applied along with a probe pulse. When the driving laser is turned off, the cavity fields decay to zero rapidly at the rate of κ and hence there is no optomechanical interaction while the mechanical mode evolves freely and decaying with a low rate γ_m. With typical parameters of OMS, the enhanced optomechanical interaction rate G is slower than the cavity decay rate κ but faster than the mechanical decay rate γ_m. The long decay time of the mechanical oscillator empowers itself to store information [52, 65]. The coherent interconversion between optical and mechanical excitations facilitates the storing and retrieving process. In this section, we

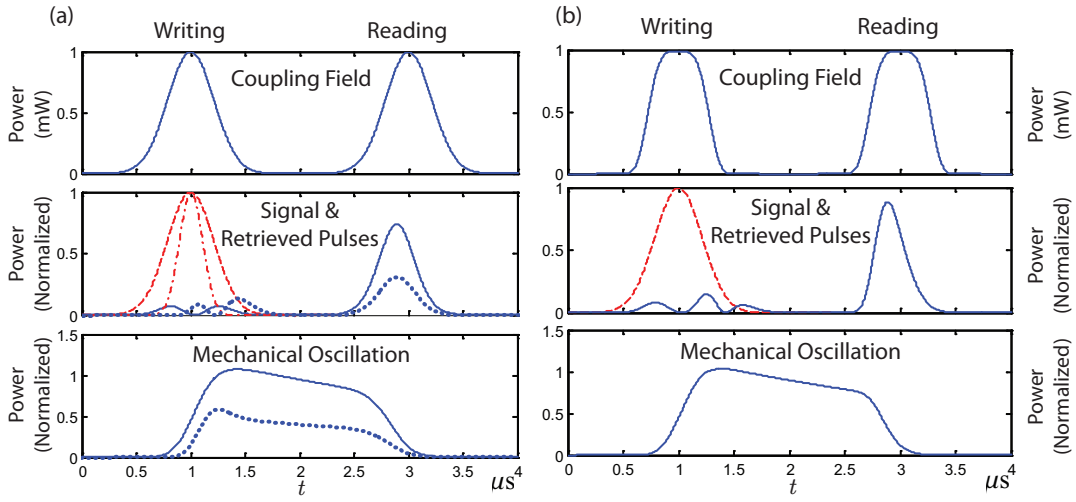

Figure 2.6: Numerical simulation of "writing" and "reading" Gaussian probe pulses using two red-detuned coupling laser pulses. (a) We plot two probe pulses with different width 0.15μs (red dot-dashed curve) and 0.3μs (red dashed curve). The Gaussian coupling pulses have width 0.3μs and their peak power is 1 mW. The powers of the output pulses and the mechanical oscillation are normalized to the peak power of the probe pulse, which is much less than the coupling pulses. In the middle and bottom panels, the blue solid curves illustrate the result corresponding to probe pulse with 0.15μs, and the blue dotted curves corresponding to 0.3μs. (b) Curves are defined similar to (a), except the coupling pulses are super-Gaussian and $\tau_l = \tau_p = 0.3\mu$s.

numerically examine the optical memory in OMS controlled by a driving laser using a Fourth-order Runge-Kutta method on Eqs. (2.4)-(2.6).

A driving laser is used to control the storage and retrieval process. It is red-detuned with respect to the cavity frequency, i.e. $\Delta = \omega_m$ and the probe field has a frequency on resonance with the cavity $\omega_p = \omega_c$. Before we send the laser pulses, the mean photon and phonon numbers are both zero. In the "writing" stage, we send in the coupling laser and the probe pulse simultaneously. For the probe pulse $\mathcal{E}_p(t)$ and

driving pulse $\mathcal{E}_l(t)$, we take Gaussian shapes

$$\mathcal{E}_p(t) = \mathcal{E}_p \mathrm{e}^{-\frac{(t-t_{wr})^2}{2\tau_p^2}}, \tag{2.21}$$

$$\mathcal{E}_l(t) = \mathcal{E}_l \mathrm{e}^{-\frac{(t-t_{wr})^2}{2\tau_l^2}} + \mathcal{E}_l \mathrm{e}^{-\frac{(t-t_{rd})^2}{2\tau_l^2}}, \tag{2.22}$$

where t_{wr} and t_{rd} are the central times of the "writing" and "reading" coupling lasers. We assume that the width τ_l of the coupling laser is no less than the width τ_p of the probe pulse. Furthermore, we assume that $\tau_p^{-1} < \Gamma_{\mathrm{EIT}}$. Clearly, if the input probe field is a pulse, then its spectral width has to be less than Γ_{EIT} in order to have distortionless propagation of the probe pulse. Two typical sets of numerical simulations are shown in Fig. 2.6(a) for the optical pulse storage and retrieval processes. We use the following parameters [59] $m = 20\mathrm{ng}$, $g/2\pi = 1.55\mathrm{kHz}$, $\gamma_m/2\pi = 41\mathrm{kHz}$, $\omega_m/2\pi = 51.8\mathrm{MHz}$, $\kappa/2\pi = 1.5\mathrm{MHz}$, $\lambda = 775\mathrm{nm}$. The stability of this set of parameters is checked using the Routh-Hurwitz criterion. In the example of the simulation, the width of the coupling laser is $\tau_l = 0.3\mu\mathrm{s}$; the widths of the probe pulses are $\tau_p = 0.3\mu\mathrm{s}$ (dashed curve and solid curve as corresponding result) and $\tau_p = 0.15\mu\mathrm{s}$ (dot-dashed curve and dashed curve as corresponding result). Assuming they are both Fourier-limited Gaussian pulses which have time-bandwidth product ~ 0.44, their spectral widths can be calculated as $\Delta\omega = 0.44/\tau_p = 2\pi \times 0.47\mathrm{MHz}$ and $2\pi \times 0.23\mathrm{MHz}$ for $\tau_p = 0.15\mu\mathrm{s}$ and $0.3\mu\mathrm{s}$, respectively. The peak power of the coupling pulse is $\mathcal{P}_l = 1\mathrm{mW}$. It produces an EIT window with width $\Gamma_{\mathrm{EIT}} = 2\pi \times 11\mathrm{MHz}$ which is much wider than the spectrum widths of the probe pulses. The optical field in the probe pulses are converted into coherent phonons of the mechanical oscillator as shown in the bottom panel of Fig. 2.6. This is because of the coherent process $\omega_p - \omega_l = \omega_m$. The coherent phonon survives over a time scale of the order of γ_m^{-1} which is much longer than the cavity lifetime κ_1^{-1}. The probe pulse can be retrieved by applying the "reading" pulse at a time later (within γ_m^{-1}). This application of "reading" pulse converts the coherent phonons into light field via the upconversion

process $\omega_l + \omega_m \rightarrow \omega_p = \omega_1$. Fiore et al. [65] demonstrated the storage and retrieval of light pulses.

We observe that the probe pulse with a larger temporal width $\tau_p = 0.3\mu$s ($\Gamma_{\rm EIT}\tau_p = 21$) is stored better than the pulse with width $\tau_p = 0.15\mu$s ($\Gamma_{\rm EIT}\tau_p = 10$). The conversion to phonons takes place more efficiently for $\tau_p = 0.3\mu$s. This then results in better retrieval of the probe pulse. The retrieved peak powers are $0.74|\mathcal{E}_p|^2$, $0.31|\mathcal{E}_p|^2$ for $\tau_p = 0.3\mu$s and $\tau_p = 0.15\mu$s, respectively.

Earlier work with atomic systems by Dey *et al.* [76] has shown that the storage and retrieval processes are more efficient if the Gaussian pulses are replaced by super-Gaussian pulses.

$$\mathcal{E}_l(t) = \mathcal{E}_l e^{-\frac{1}{2}(\frac{t-t_{wr}}{\tau_l})^\beta} + \mathcal{E}_l e^{-\frac{1}{2}(\frac{t-t_{rd}}{\tau_l})^\beta}. \tag{2.23}$$

For $\beta = 4$, we have adiabatic switching on and off of the coupling fields. It has a more rectangular tempo profile with sharp edges. Fig. 2.6(b) shows the result of numerical simulation using super-Gaussian shaped "writing" and "reading" laser pulses. Comparing Figs. 2.6(a) and (b), we find the super-Gaussian coupling pulses produce a retrieved pulse with sharper front edge and higher peak power $0.79|\mathcal{E}_p|^2$. The almost complete recovery of the weak probe pulse is especially significant in the context of single photon optical memories.

In an experiment by Wang [65], they used a silica microsphere and coupled the whispering gallery modes with the mechanical radial breathing mode at frequency $\omega_m/2\pi = 108.4$ MHz. They managed to achieve very high quality factors that the mechanical quality factor is around 3000 and the cavity quality factor is around 0.5×10^5. Correspondingly, the mechanical and optical decay rates are $\gamma_m/2\pi = 38$ kHz and 40 MHz. They drive the optomechanical interaction with a pair of "writing" and "retrieval" pulses and the effective coupling rate during the pulses are $|G|/2\pi = 2$ MHz. Thanks to the low mechanical decay rate, they stored an optical pulse for 3.5μs before retrieving it. Comparing to the life-time of the optical cavity field of $1/\kappa \approx 4$

ns, the optomechanical storage time is three orders longer!

2.3 Introduction to Ramsey interferometry

The Ramsey method of separated oscillatory fields is a highly successful method of precision spectroscopy and has been extensively used in a wide spectral range starting from the radio frequency to optical domain [67]. This method has yielded the and molecular transition frequencies with very high precision especially by using phase-coherent pulses with a duration that is short compared to the atomic decay times. The Ramsey technique is an interference technique in which one studies the result of the quantum-mechanical amplitudes in different domains where fields are applied. It has so far been used in the study of the phase coherence in atomic and molecular systems. Ramsey method has been especially successful in the detection of quantum coherences, such as in the detection of the Schrödinger-cat states of an electromagnetic field.

The optomechanical Ramsey Interferometry (RI) [43] contains two pairs of laser pulses interacting in an OMS. The interaction process during each pulse pair is similar to the optical memory explained in the last section. In a RI setup, two pairs of driving and probe pulses with separation T are sent to the cavity. This is in contrast to a pair of driving pulses and a single probe pulse in the optical memory. Two processes are taking place when a pulse pair is in the cavity: ① the coupling and probe photons combine and produce coherent phonons; and ⑪ the coherent phonons combine with the coupling photons and generate an anti-Stokes sideband near the cavity resonance. The application of the first pulse pair creates both coherent phonons and cavity photons. After the first pulse pair, the optical mode decays rapidly during the free evolution and it becomes negligible as $e^{-\kappa T} \sim 0$, where κ is the total decay rate of the cavity amplitude. On the other hand, the mechanical mode shows almost no decay as $e^{-(\gamma_m/2)T} \lesssim 1$, where γ_m is the mechanical damping rate. This is because

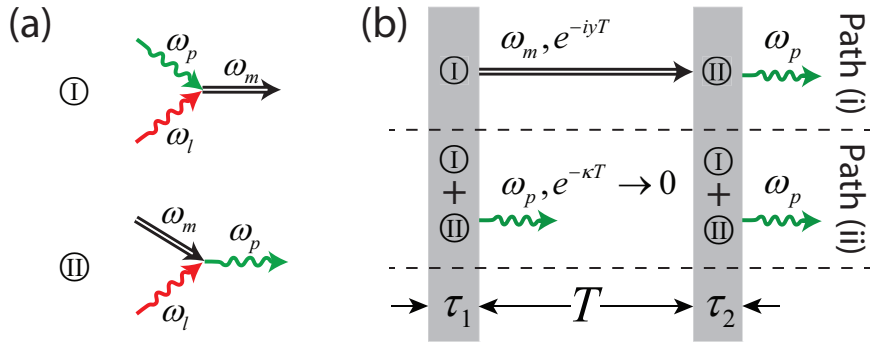

Figure 2.7: The physical process of the photons and phonons in the Ramsey setup. The wavy arrows refer to photons and double arrows refer to phonons. (a) The driving photon combining a probe photon generates a phonon and the driving photon combining a photon generates a probe photon. (b) The two paths of generating a photon at ω_p and $y = \omega_p - \omega_l - \omega_m$.

$\gamma_m \ll \kappa$. Thus, before the second pulse pair is applied, the mechanical mode barely decays but gathers a phase $\omega_m T$. Now we examine the two paths which lead to the interference in the optical field produced at ω_p. The phonon created in the zone "τ_1" survives and interacts with the driving laser to produce a photon at ω_p via process Ⅱ in the zone "τ_2". This is marked as path (i) in Fig. 2.9. Photons at ω_p can also be generated entirely in the zone "τ_2", as discussed earlier [path (ii) of Fig. 2.7]. These two paths are displayed in Fig. 2.7(b) and their coherent character leads to Ramsey fringes in the optical output field, which can be detected directly through heterodyne interference with a local oscillator. Note that the pattern does not arise from the direct interference of the two input probe pulses, since the free evolution time is much longer than the optical decay time, $T \gg 1/\kappa$. The mechanical oscillation is the only medium that can carry coherence during both pulses. Therefore, the fringes arise from the mechanical coherence effects although we observe such coherences in the optical fields.

2.4 Theoretical model of Ramsey Interferometry

For the implementation of Ramsey Interferometry in OMS, we enable the optomechanical coupling in two time-separated regions, during which a pair of laser pulses including both driving pulse and probe pulse are sent into the cavity. The probe laser with frequency ω_p is near the cavity resonance ω_c and the driving laser with frequency ω_l is near the red sideband of the cavity resonance $\omega_c - \omega_m$. The pulse sequence is shown in Fig. 2.7(b), where we denote the widths of the pulses by τ_1 and τ_2 and the separation by T. The time-dependent amplitudes of the driving and probe, $\mathcal{E}_l(t)$ and $\mathcal{E}_p(t)$, are both nonzero only during the pulses: $\mathcal{E}_l(t) = \mathcal{E}_l$ and $\mathcal{E}_p(t) = \mathcal{E}_p$ for $t \in [0, \tau_1] \cup [T + \tau_1, T + \tau_1 + \tau_2]$, and $\mathcal{E}_l(t) = \mathcal{E}_p(t) = 0$ otherwise. As discussed in the previous section, each pulse pair generates coherent phonons, and those generated by different pulse pairs interfere leading to Ramsey fringes. In this section, we assume the critical coupling condition, *i.e.* $\kappa_e = \kappa_i = \kappa/2$.

The optical output field can be solved by integrating Eq. (2.9). The states of the optical and mechanical mode after application of a single pulse have already been calculated in Eqs. (2.11)-(2.19). Between these two pulses, the intra-cavity optical fields reduce to zero rapidly and hence the effective coupling rate $G = 0$. The system is governed by the matrix differential equation

$$\dot{\Psi}(t) = \mathbb{N}\Psi(t), \qquad \mathbb{N} = -\begin{pmatrix} \kappa - ix & 0 \\ 0 & \gamma_m/2 - iy \end{pmatrix}. \tag{2.24}$$

By combining it with solution (2.11), we are able to obtain the fields after the application of both pulses, $\Psi_R \equiv \Psi(T + \tau_1 + \tau_2)$, as

$$\begin{aligned} \Psi_R &= \mathrm{e}^{\mathbb{M}\tau_2}\mathrm{e}^{\mathbb{N}T}\Psi_{s1}(\tau_1) + \int_{T+\tau_1}^{T+\tau_1+\tau_2} \mathrm{e}^{\mathbb{M}(T+\tau_1+\tau_2-t')}\mathbb{D}_2(t')\mathrm{d}t' \\ &= \mathrm{e}^{\mathbb{M}\tau_2}\mathrm{e}^{\mathbb{N}T}\Psi_{s1}(\tau_1) + \Psi_{s2}(\tau_2), \end{aligned} \tag{2.25}$$

where $\mathbb{D}_2 = (\mathcal{E}_{p2} \quad 0)^T$ and

$$\Psi_{si}(\tau_i) = \mathbb{M}^{-1}(\mathrm{e}^{\mathbb{M}\tau_i} - \mathbb{1})\mathbb{D}_i, \qquad \text{for } i = 1, 2, \tag{2.26}$$

which has been calculated in Eq. (2.18). We see that the expression of fields after two pulses, Ψ_R, contains two terms, each of which has a form of Ψ_{si} with one of them modulated by a phase difference associated with the free evolution time T between two pulses. Next we examine the mechanical and optical fields as given in Eq.(2.25) using Ramsey's scheme by applying two separated pulses to OMS. The component $\mathrm{e}^{\mathbb{N}T} = \mathbf{diag}(\mathrm{e}^{-(\kappa-ix)T} \quad \mathrm{e}^{-(\frac{\gamma_m}{2}-iy)T})$ can be easily obtained. Ramsey's proposal demands the free evolution time $T \gg \tau$, as long as it is still smaller than the relaxation time $(\gamma_m/2)T \lesssim 1$. The matrix exponential can be further simplified $\mathrm{e}^{\mathbb{N}T} \approx \mathbf{diag}(0 \quad \mathrm{e}^{-(\frac{\gamma_m}{2}-iy)T})$. Then the fields after the application of the pulse can be given as

$$\begin{aligned}\Psi_R &= \begin{pmatrix} (e^{\mathbb{M}\tau})_{12}e^{-(\frac{\gamma_m}{2}-iy)T}(\Psi_{s1})_2 + (\Psi_{s2})_1 \\ \\ (e^{\mathbb{M}\tau})_{22}e^{-(\frac{\gamma_m}{2}-iy)T}(\Psi_{s1})_2 + (\Psi_{s2})_2 \end{pmatrix} \\ &= \begin{pmatrix} \dfrac{(\kappa-ix+\lambda_+)(\lambda_+ + iy - \gamma_m/2)((\lambda_- - \lambda_+) + \lambda_+\mathrm{e}^{\lambda_-\tau_1})}{[|G|^2 + (\kappa - ix+)(\gamma_m/2 - iy)](\lambda_- - \lambda_+)^2}\mathrm{e}^{\lambda_-\tau_2-(\frac{\gamma_m}{2}-iy)T}\mathcal{E}_{p1} \\ \quad + \dfrac{(\gamma_m/2-iy)(\lambda_- - \lambda_+) + (|G|^2 - (\kappa - ix + \lambda_+)(\gamma_m/2 - iy))\mathrm{e}^{\lambda_-\tau_2}}{[|G|^2 + (\kappa - ix)(\gamma_m/2 - iy)](\lambda_- - \lambda_+)}\mathcal{E}_{p2} \\ \dfrac{iG^*[\lambda_- - \lambda_+(1-\mathrm{e}^{\lambda_-\tau_2})][(\lambda_- - \lambda_+)\mathcal{E}_{p2} + (\lambda_+ - iy - \gamma_m/2)\mathrm{e}^{\lambda_-\tau_1-(\frac{\gamma_m}{2}-iy)T}\mathcal{E}_{p1}]}{[|G|^2 + (\kappa - ix+)(\gamma_m/2 - iy)](\lambda_- - \lambda_+)^2} \end{pmatrix},\end{aligned} \tag{2.27}$$

where $(..)_{ij}$ follows the notation in Sec. 2.1 representing the element in the ith row and jth column of a matrix. Recall Eq. (2.17), from which we simplify Ψ_R by using the results (2.19) and (2.20)

$$\Psi_R = \begin{pmatrix} \frac{|G|^2}{\kappa^2}\frac{e^{-(\Gamma_{\mathrm{EIT}}-iy)\tau_1}-1}{\Gamma_{\mathrm{EIT}}-iy}e^{-(\Gamma_{\mathrm{EIT}}-iy)\tau_2-(\gamma_m/2-iy)T}\mathcal{E}_{p1} + \left[\frac{1}{\kappa} + \frac{|G|^2}{\kappa^2}\frac{e^{-(\Gamma_{\mathrm{EIT}}-iy)\tau_2}-1}{\Gamma_{\mathrm{EIT}}-iy}\right]\mathcal{E}_{p2} \\ \\ \frac{iG^*}{\kappa}\left[\frac{e^{-(\Gamma_{\mathrm{EIT}}-iy)\tau_1}-1}{\Gamma_{\mathrm{EIT}}-iy}e^{-(\Gamma_{\mathrm{EIT}}-iy)\tau_2-(\gamma_m/2-iy)T}\mathcal{E}_{p1} + \frac{e^{-(\Gamma_{\mathrm{EIT}}-iy)\tau_2}-1}{\Gamma_{\mathrm{EIT}}-iy}\mathcal{E}_{p2}\right] \end{pmatrix} \tag{2.28}$$

We can define a phase parameter ϕ and a damping parameter μ

$$\phi = -y(\tau_2 + T), \quad \mu = (\frac{\gamma_m}{2}T + \Gamma\tau_2). \tag{2.29}$$

In the critical coupling regime $\kappa_e = \kappa/2$, the final intra-cavity amplitude is

$$\begin{aligned}\mathcal{E}_c(T+\tau_1+\tau_2) &= 2\kappa_e a_1(T+\tau_1+\tau_2) \\ &\approx \left[1+\frac{|G|^2}{\kappa}\frac{e^{-(\Gamma_{\rm EIT}-iy)\tau_2}-1}{\Gamma_{\rm EIT}-iy}\right]\mathcal{E}_{p2} + \frac{|G|^2}{\kappa}\frac{e^{-(\Gamma_{\rm EIT}-iy)\tau_2}-1}{\Gamma_{\rm EIT}-iy}e^{-i\phi-\mu}\mathcal{E}_{p1}, \end{aligned} \tag{2.30}$$

and the final mechanical field is

$$\kappa_e b_1(T+\tau_1+\tau_2) \approx \frac{iG^*}{2}\left[\frac{e^{-(\Gamma_{\rm EIT}-iy)\tau_2}-1}{\Gamma_{\rm EIT}-iy}e^{-i\phi-\mu}\mathcal{E}_{p1} + \frac{e^{-(\Gamma_{\rm EIT}-iy)\tau_2}-1}{\Gamma_{\rm EIT}-iy}\mathcal{E}_{p2}\right]. \tag{2.31}$$

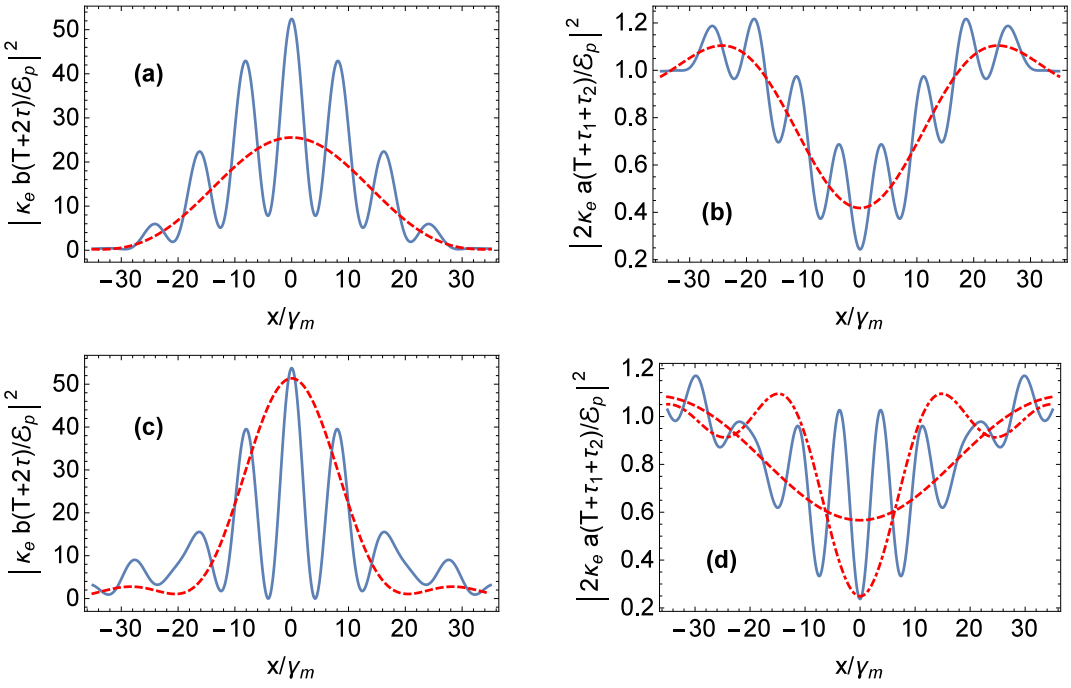

Figure 2.8: The mechanical field [panels (a) and (c)] and output optical field [panels (b) and (d)] after the application of a single pulse (dashed curves) and of two separated pulses (solid curves). The parameters for the OMS are $\kappa/2\pi = 20$MHz, $|G|/2\pi = 0.7$MHz, $\gamma_m/2\pi = 0.01$MHz and the corresponding EIT width for the steady state is $\Gamma_{\rm EIT} = 3\gamma_m$. We also set $\mathcal{E}_{p1} = \mathcal{E}_{p2}$ and $x = y$ and $2\kappa_e = \kappa$. In panels (a) and (b) we set the pulse lengths both $\tau_1 = \tau_2 = 3\mu$s and their separation is $T = 3\tau$; and in panels (c) and (d) the pulse lengths are optimized for best visibility: $\tau_1 = 5\mu$s, $\tau_2 = 1.9\mu$s and $T = 9\mu$s. In panel (d), the dot-dashed curve is for single pulse excitation with $\tau_2 = 1.9\mu$s.

We start by analyzing the mechanical mode given in Eq.(2.31). It denotes the mechanical excitation at the end of the second pulse τ_2. From the expression with a two-term structure, we see that it has two contributions: the excitation due to the first pulse (denoted as the first term) and the excitation due to the second pulse (denoted as the second term). The fraction in each term describes the mechanical excitation generated by the transient EIT during each pulse, whose detail has been explained in detail in the previous section. The optomechanical interactions result in two similar excitations; however, there is a phase factor $\mathrm{e}^{-i\phi}$ multiplied to the first term. As ϕ changes, the two terms in Eq.(2.30) interfere either constructively or destructively leading to Ramsey fringes. The phase $\phi = -y(T + \tau_2)$, *i.e.* the product of the frequency detuning and the evolution time, determines the fringe period $2\pi/(T+\tau_2)$. However, a longer τ_2 can result in a decay of the signal, which can be seen from the parameter $\mu = \Gamma_{\mathrm{EIT}}\tau_2 + \frac{\gamma_m}{2}T$. We especially remark that the damping due to $\exp(-\Gamma_{\mathrm{EIT}}\tau_2)$ is not negligible, because it is related to the generation rate of the mechanical excitation, *i.e.* $e^{-(iy+\Gamma_{\mathrm{EIT}})\tau_2} - 1$, during the second pulse. Considering $\Gamma_{\mathrm{EIT}} > \gamma_m$, one should reasonably choose $\tau_2 < 1/\Gamma_{\mathrm{EIT}}$. The numerator of each term $\mathrm{e}^{-(\Gamma_{\mathrm{EIT}}-iy)\tau_i} - 1 \sim 0$ for a short τ_i, and it increases along with τ_i. This justifies that the phonon excitation is only prominent when τ_1 is large, which sets the characteristic time of phonon excitation in OMS, i.e. $\Gamma_{\mathrm{EIT}}\tau_1 > 1$. The electromagnetically induced transparency occurs when $\Gamma_{\mathrm{EIT}}\tau_1 \gg 1$. In the optomechanical RI, a large τ_1 enhances the Ramsey fringes contrast, although the fringes can still be seen at a shorter τ_1. For a good contrast, the decay term μ in Eqs. (2.30) and (2.31) should be small and hence $\Gamma_{\mathrm{EIT}}\tau_2 < 1$. This is to keep the amplitude of the phonon, excited by the first pulse, significant during the interaction with the second pulse. Therefore, the conditions for the Ramsey fringes are $\tau_1\Gamma_{\mathrm{EIT}} \gtrsim 1$, $\tau_2\Gamma_{\mathrm{EIT}} < 1$, and $T\gamma_m \ll 1$. The optical field expressed in Eq.(2.30) exhibits the same interference fringes as in the mechanical mode. This is important as the measurement of the output optical field

becomes a direct probe of the Ramsey fringes in the mechanical system. In order to clearly show the Ramsey fringes in the mechanical oscillation, we have plotted the numerical result of Eq.(2.27) in Fig. 2.8(a). In the plot, the duration of each pulse is $\tau = 3\mu$s and their separation $T = 3\tau$. The dashed curve, which is the result using a single pulse excitation, exhibits a Lorentzian shape with half width $\sim 30\gamma_m$. The solid curve, which is using Ramsey's two separated pulses excitation, clearly shows the fast oscillating fringes over the broad Lorentzian envelope. The period of the fringes is $8\gamma_m \approx 2\pi/(T + \tau_2)$ and it agrees with our calculation.

The visibility of the Ramsey fringe for the mechanical mode is determined by difference between the two terms in Eq.(2.30). For an on-resonance probe pulse ($y = 0$) and identical driving pulse power, it can be written as

$$\begin{aligned}\mathcal{V} &= \frac{\mathcal{E}_{c\max} - \mathcal{E}_{c\min}}{\mathcal{E}_{c\max} + \mathcal{E}_{c\min}} \\ &= \frac{2(1 - e^{-\Gamma_{\rm EIT}\tau_1})e^{-(\frac{\gamma_m}{2}T + \Gamma_{\rm EIT}\tau_2)}\mathcal{E}_{p1} \times (1 - e^{-\Gamma_{\rm EIT}\tau_2})\mathcal{E}_{p2}]}{[(1 - e^{-\Gamma_{\rm EIT}\tau_1})e^{-(\frac{\gamma_m}{2}T + \Gamma_{\rm EIT}\tau_2)}\mathcal{E}_{p1}]^2 + [(1 - e^{-\Gamma_{\rm EIT}\tau_2})\mathcal{E}_{p2}]^2}\end{aligned} \tag{2.32}$$

In the case of our parameters, $1/\Gamma_{\rm EIT} \approx 5\mu$s and $\Gamma_{\rm EIT} = 3\gamma_m$, hence $2/\gamma_m = 6/\Gamma_{\rm EIT} \approx 30\mu$s. For $\tau_1 = \tau_2 = 3\mu$s and $T = 9\mu$s, the visibility $\mathcal{V} = 0.70$ which agrees with the curves in Fig. 2.8(a). In order to optimize the fringe visibility, we need to select pulse lengths such that $(1 - e^{-\Gamma_{\rm EIT}\tau_1})e^{-\mu}\mathcal{E}_{p1} = (1 - e^{-\Gamma_{\rm EIT}\tau_2})\mathcal{E}_{p2}$. For these parameters, the visibility approaches 100% when $\tau_1 = 5\mu$s, $\tau_2 \approx 1.9\mu$s and $T = 9\mu$s. We illustrate the mechanical mode and optical mode in Fig. 2.8(c) and (d) with this set of parameters and we find the visibility indeed reaches almost unity.

In order to appreciate the versatility of the Ramsey fringes in OMS, we show in Fig. 2.9 additional results of simulations under a range of parameters. As shown in Fig. 2.9(a), the interference fringes decrease with longer τ_2, which means no coherent phonons for interference. This is due to the decay term μ in Eq.(2.5). As noted in the previous two paragraphs we need $\Gamma_{\rm EIT}\tau_2$ to be small. In Fig. 2.9(b) we can see that, when τ_2 is short, the spectrum shows interference; but with long enough τ_2,

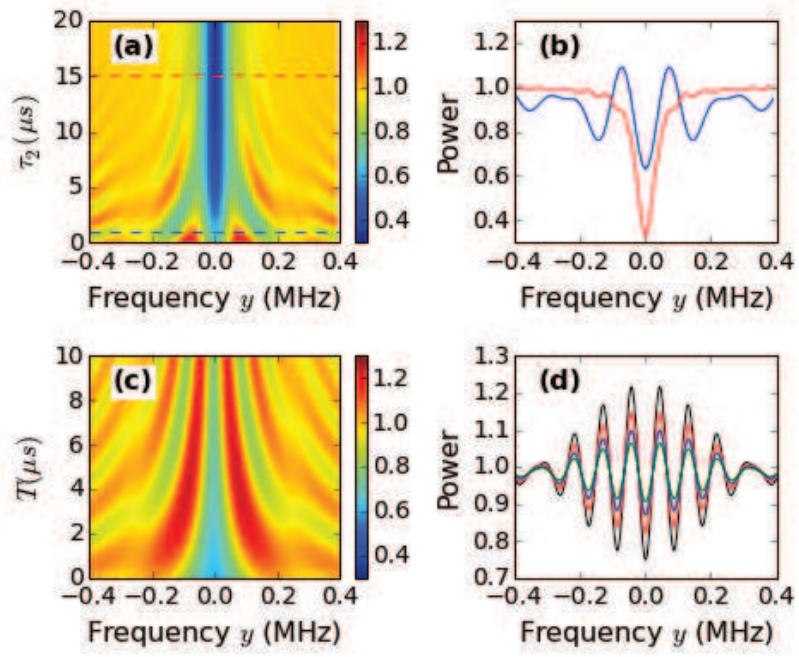

Figure 2.9: (a) Simulation of the normalized emission power as a function of τ_2 with fixed $\tau_1 = 4\mu$s, $T = 4\mu$s, $\kappa/2\pi = 30$MHz, $|G|/2\pi = 0.58$MHz, and $\gamma_m/2\pi = 20$kHz. (b) The spectra with $\tau_2 = 1\mu$s (blue curve) and $\tau_2 = 15\mu$s (red curve), as dashed line shown in (a). (c) The Ramsey fringe with different delay time T. Other parameters are the same as (a) except $\tau_2 = 0.1\mu$s. (d) The Ramsey fringes with $T = 10\mu$s and different $\gamma_m/2\pi = 10, 20, 30, 40k$Hz for black, red, blue and green curves, respectively. Other parameters are the same as in (c).

the fringes in the spectrum cannot be seen and the spectrum reduces to a steady-state result. With other parameters fixed, the increase in time T leads to a decease in the Ramsey fringe period. However, after long enough time, the Ramsey fringes disappear because of the damping of phonons, as shown in Fig. 2.9(c). Therefore, we should choose the γ_m as small as possible during the experiment for observing Ramsey fringes. This is demonstrated more clearly in Fig. 2.9(d), which shows the visibility of the Ramsey fringes with different γ_m.

2.5 Experimental implementation

In the experiment done in collaboration with Prof. Hailin Wang and Dr. Dong, we couple an optical WGM of a silica microsphere [$\kappa/2\pi \sim 15$MHz [1] and $\eta = 1/2$ (critical coupling regime)] to the (1, 2) radial-breathing mechanical mode ($\omega_m/2\pi \sim 94$MHz, $\gamma_m/2\pi \sim 20$kHz and the quality factor $\sim 1.3 \times 10^7$) of the microsphere. The WGM

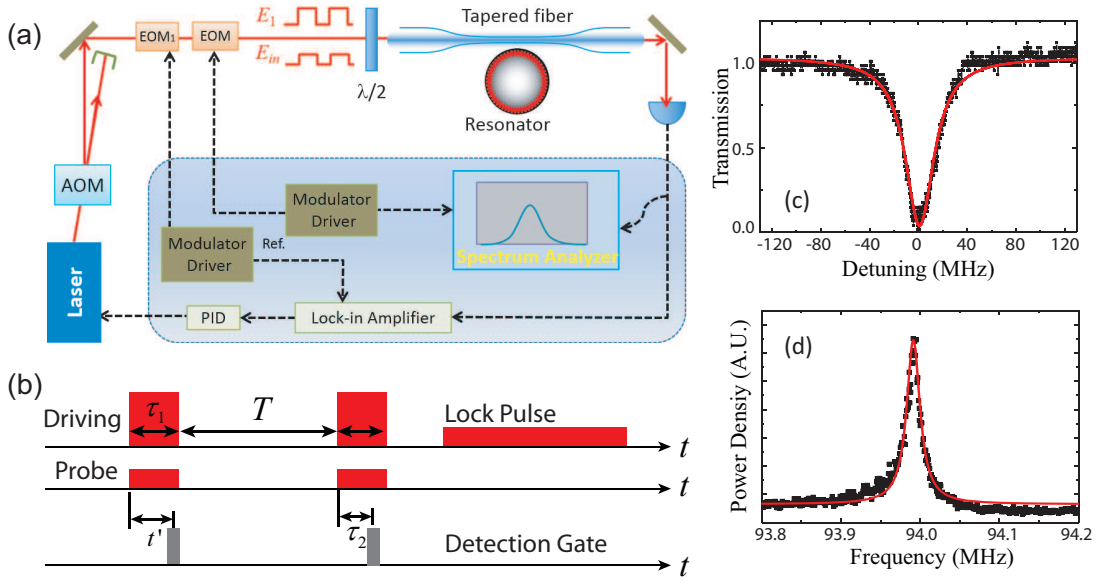

Figure 2.10: (a) Schematic of the experimental setup for the Ramsey Interferometry, with solid lines representing the optical paths and dashed lines representing the electrical connections. (b) Sketch of the Ramsey pulse sequence applied to OMS. (c) Transmission resonance for the WGM at ~ 780nm with $\kappa/2\pi = 15 \pm 0.65$MHz. (d) Displacement power spectrum of the $(1, 2)$ radial breathing mode with $\gamma_m/2\pi = 20 \pm 2$kHz, obtained from the same sample. No error bars are shown as these are negligible. The solid red lines show the Lorentzian fittings.

was excited through the evanescent field of a tapered optical fiber. A combination of an acoustic-optic modulator (AOM) and electro-optic modulators (EOMs) was used to generate optical pulses with the desired duration, timing, and frequencies.

[1] Note the definition of κ is different by a factor of 2 in paper [67].

The driving and the locking pulses came from a single-frequency tunable diode laser (Toptica DLPRO 780) with $\lambda \sim 780$ nm and with its frequency locked to the red sideband of a given WGM resonance using the Pound-Drever-Hall technique. The

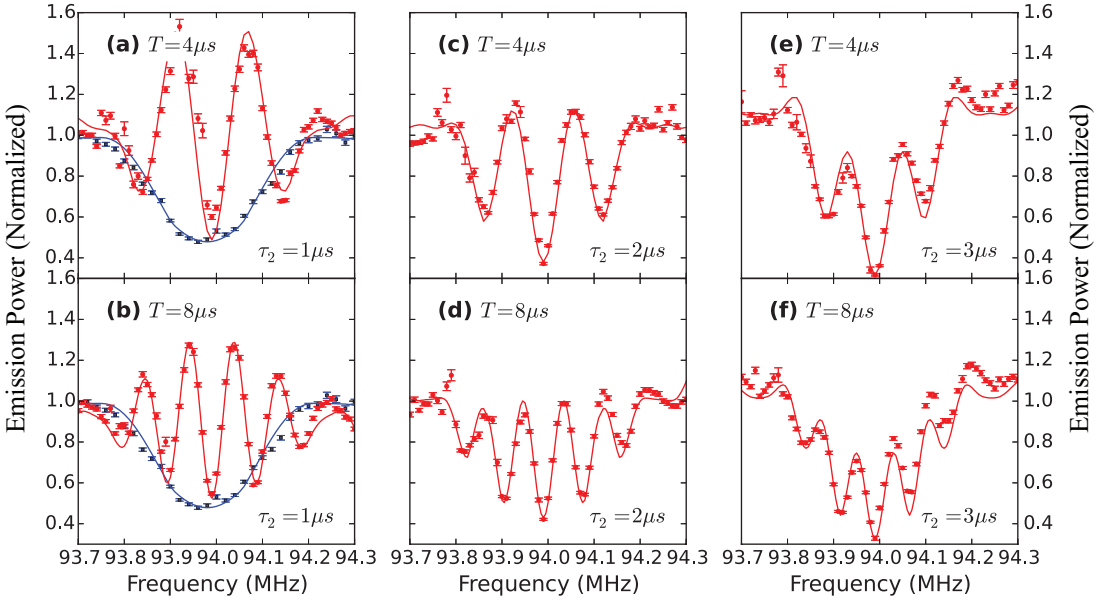

Figure 2.11: Heterodyne detected probe intensity as a function of the detuning between the probe and driving lasers. The blue dots in (a) and (b) are obtained with the detection gate positioned within the first pulse pair with the delay time $\tau_1 = 4\mu$s. The black dots in (a-f) are obtained with the detection gate positioned within the second pulse pair with T and τ_2 indicated in the figure. The incident driving power used is 3.4mW. The solid lines are results of theoretical calculations.

signal pulses were driven from the blue sideband generated by passing the driving pulses through EOM_0. For the experimental results reported here, both the driving and the probe pulses were square shaped, with the same timing and with duration of 4μs. The effective coupling strengths under the pulses are $|G|/2\pi = 0.58$MHz leading to the cooperativity $C = 2.2$. Heterodyne detection was used for the measurement of the optical emission from the microsphere near the WGM resonance, with the driving laser pulse serving as the local oscillator. A gated detection scheme was also used with a gate duration of 1μs. The timing of the gate determines the effective duration,

τ_2, of the second pulse pair involved in the RI.

Figure 2.11 shows the heterodyne detected probe intensity as a function of the detuning between the probe and the driving laser obtained with different durations τ_2. The separation time, T, between the first and second pulse pairs is set to 4μs in the left-hand column and 8μs in the right-hand column. The distinct spectral oscillations observed in these experiments demonstrate the Ramsey fringes for the OMS. The spectral position of the central Ramsey fringe overlaps exactly with the center of the OMIT dip and does not depend on either T or τ_2. This enables us to estimate the mechanical oscillation frequency ω_m by relating them to the detuning of the probe and driving laser $\omega_p - \omega_l$ using $y = \omega_p - \omega_l - \omega_m$. The dips in Figs. 2.11 all reveal that $\omega_p - \omega_l \approx 2\pi \times 93.9$MHz which agrees well with $\omega_m = 2\pi \times 94$MHz. In (a) with $T = 4\mu$s and $\tau_2 = 1\mu$s, the Ramsey fringe period is 160kHz. As $T + \tau_2$ increase from 5μs in (a) to 11μs in (f), the fringe period decreases from $\sim$ 160kHz to $\sim$ 80kHz. As a reference, we also show in Figs. 2.11(a) and 2.11(b) the experimental results (solid circles) obtained in the absence of the second pulse pair. Experimentally, these were obtained with the detection gate positioned within the duration of the first pulse pair. The spectral dip observed in this case arises from the *transient* optomechanically induced transparency (OMIT).

For a direct comparison with the experiments, over a wide range of parameters we show the results of the theoretical calculations as solid curves in Fig. 2.11. The parameters (within error bars) used include $\kappa/2\pi = 15$MHz, $|G|/2\pi = 0.58$MHz, $\gamma_m/2\pi = 20$kHz, and the corresponding characteristic time $1/\Gamma_{\rm EIT} = 4.9\mu$s. For the theory curves we use the equations of motion (2.3), but two pairs of pulses illustrated in Fig. 2.10(b) are used. As shown in Fig. 2.11, the spectral position of the central Ramsey fringe overlaps exactly with the center of the OMIT dip and does not depend on either T or τ_2. More importantly, the Ramsey fringes exhibit a period that is much smaller than the linewidth of the OMIT dip. In (a) with $T = 4\mu s$ and $\tau_2 = 1\mu s$, the

Ramsey fringe period is 160kHz. As $T + \tau_2$ increase from $5\mu s$ in (a) to $11\mu s$ in (f), the fringe period decreases from $\sim$ 160kHz to $\sim$ 80kHz. Overall, there is an excellent agreement between the theory (curves) and experiment (dots). The visibility of the Ramsey fringes is primarily determined by τ_2. Fig. 2.11. reveals the loss of fringe visibility with increasing τ_2. We note that for comparison with the experiments, we use directly Eqs.(2.28). It is only for understanding the physical behavior that we used the approximate Eqs.(2.30).

2.6 Summary

To summarize the results, I have developed a theory to study the transient behavior of EIT in OMS under control of a strong driving laser and a weak probe laser. The physics behind the effect is explained by using the coherent photon-phonon interaction processes. The dynamics of phonons shows clearly how the fields are stored and how these could be converted back into fields with frequencies which depend on the power and the detuning of the driving laser field. This mechanism enables us to design OMS-based optical memories and transduction of the optical fields. In the second part of this chapter, I demonstrated how the high-resolution Ramsey method of separated oscillatory fields can be adopted to study coherences in a macroscopic system like a nanomechanical oscillator. I presented the underlying theory and the experimental demonstration using silica microresonators. The method is quite versatile and can be adopted to different types of mechanical resonators and electromechanical resonators. More complex applications can include the study of the dynamical interaction between the mechanical oscillators. Future work may also include the demonstration of the Ramsey fringes using excitations at the single photon level which would imply excitation of a mechanical oscillator at the single phonon level. Needless to say, achieving the quantum regime experimentally would require at least the coherent fields at the single photon level as well as cooling to temperatures such that the mean phonon

number is less than 1. The Ramsey method is also expected to be useful in producing time-bin entanglement involving a phonon and a photon.

CHAPTER 3

ELECTROMAGNETICALLY INDUCED ABSORPTION AND TRANSDUCTION OF FIELDS

Optomechanical systems have been recognized as good systems for the purpose of optical memories as mechanical systems can have very long coherence times [62, 65, 77]. The realization that such systems can serve as memory elements became feasible by the prediction [58] of EIT and its experimental demonstration by several groups [59–61]. Much of this work was motivated by the corresponding work in atomic media [73–75]. In EIT, the driving laser induces a narrow spectral transparency window for a probe laser. Its counterpart, Electromagnetically Induced Absorption (EIA) was studied by Harris and Yamamoto [78] based on a four level atomic scheme where one of the ground levels of the Λ scheme was connected by an optical transition to a higher level. This allowed the possibility of two photon absorption while at the same time suppressing one photon transition. Lezama and coworkers [79–81] found that a simple three level Λ scheme cannot give rise to EIA. They considered optical transitions between the hyperfine states of atoms $F \to F' > F$ which showed the possibility of EIA. Clearly, if EIA was possible in OMS, then we need to consider a more complicated configuration than, say, considered in the context of EIT: One needs to add an additional pump and at least one additional transition. Hence we study a double-cavity configuration which is flexible enough to open up new pathways for the interaction with the probe field. Specifically, by adding one more cavity mode to the OMS, we are able to study the EIA [53] which creates a sharp peak inside the EIT transparency window.

The double-cavity OMS, which couples two cavity modes with common mechanical modes, represents another development in the study of optomechanics. By including one more cavity mode, the theoretical model of OMS becomes a three-coupled-oscillator model in the linearization approximation and new phenomena arise from the coherent coupling among different modes. Double-cavity configurations have attracted a lot of attention because of their wide applicability in state transfer [82, 83] and transduction of photons [66]. As a remarkable feature, these two cavity modes can be in completely different frequency regimes which may include even a microwave cavity. The mediating mechanical mode which couples the optical mode and the electrical mode functions as an active mode coupler provides the possibility to realize wavelength conversion [68, 84, 85].

In this chapter, I first briefly describe a few different experimental realizations of double-cavity OMS and provide the theoretical model of a general double-cavity OMS by utilizing the tools developed in Chap. 1. I solve for the system steady-states using Floquet analysis, instead of linearization, and transform the periodic oscillations of the modes into a traditional linear system with real constant amplitudes. This method yields a solution with multiple sidebands around the driving fields. Next, I provide a detailed analysis of the EIA in a double-cavity OMS including absorption peak width, dispersion property and its physical description. Since this model is quite generic, I present its experimental verification in metamaterials by collaborating with an experimental group. I show the peculiar property of the mechanical dark state in the EIA setup and its important application of coherent state transfer. The last section of this chapter illustrates the flexible applicability of this double-cavity OMS in optical memories and field transduction.

3.1 Experimental realizations of double-cavity OMS

Double-cavity OMS can be realized in several different ways. We mention three possible systems which have already been realized. The most direct realization is a "membrane-in-the-middle setup" [84, 85], illustrated in Fig. 3.1. In the setup by

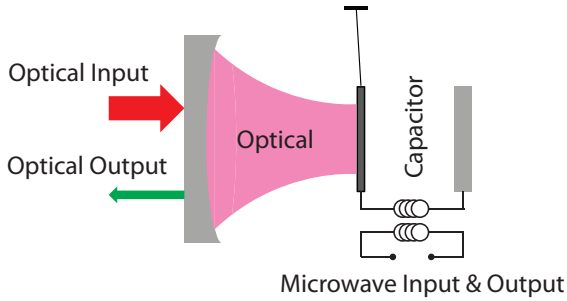

Figure 3.1: Schematic double-cavity OMS with a suspending mirror in the center. The mirror forms a Fabry-Pérot cavity with a fixed mirror on its left; and it forms an electric capacitor with a fixed conductive plate on the right.

Polzik's group [85], a silicon nitride membrane that has been coated with dielectric material is placed in front of a mirror thus forming an optical Fabry-Pérot cavity. On the other side, it interacts with an inductor-capacitor (LC) circuit that forms the microwave resonator. As the membrane vibrates it moves and modulates the resonant frequency of the optical cavity and also the capacitance of the microwave circuit, and thus the electrical resonant frequency. Lehnert's group adopted a similar setup but they use a partially transmissive membrane and place it in the middle of a Fabry-Pérot cavity. Inside the cavity, they also place a dielectric plate off the cavity axis which forms a capacitor with the moving membrane. While the membrane vibrates, it moves along with the intensity of the optical standing wave and modulates the optical resonant frequency. Therefore, the mechanical vibration mode is coupled to both the optical and electrical cavities realizing a double-cavity OMS.

The second type of double-cavity OMS is realized in a silica microresonator with

two preselected optical modes interacting with a mechanical mode [19, 21, 43, 65], illustrated in Fig. 3.2. Light is guided in whispering-gallery modes (WGM), which

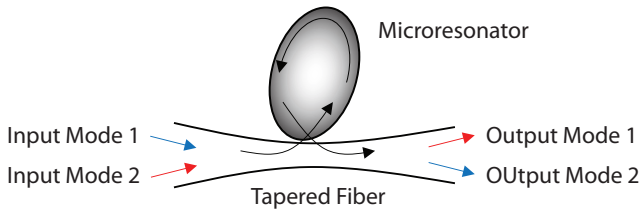

Figure 3.2: Schematic double-cavity OMS in a microresonator with two preselected optical modes interacting with a mechanical mode.

have very high quality factors, along the rim of a circular resonator. The optical path forms a circular shape bounded by the physical dimension of the microsphere. As the light changes direction when it propagates, it exerts radiation pressure onto the surface of the microsphere and this pressure force can be intense enough to deform the microsphere. A microsphere supports a large number of different mechanical normal modes of vibration or stretching. The resulting distortion of the microsphere structure directly modifies the optical path length and thereby shifting the optical resonance frequency. The small physical dimension of the microsphere and the low effective mass allow the appearance of a large single photon coupling strength g. Within such a setup, one can select two optical modes which couple to a common mechanical mode to realize a double-cavity OMS.

Two coupled waveguides enbedded in an optomechanical crystal [68] is another good playground for optomechanics. It is illustrated in Fig. 3.3. Photonic crystals are formed by a periodic modulation of the refraction index of a substrate material which forms the crystal lattice with its optical band(s). Defects are also introduced to form optical bandgaps in which light cannot propagate. With specially designed structure of defects, the bandgaps can localize light so that light does not decay into the continuum in the structure. When one prepares a thin layer of such photonic crystal, it can be stretched easily by the radiation pressure of the optical mode.

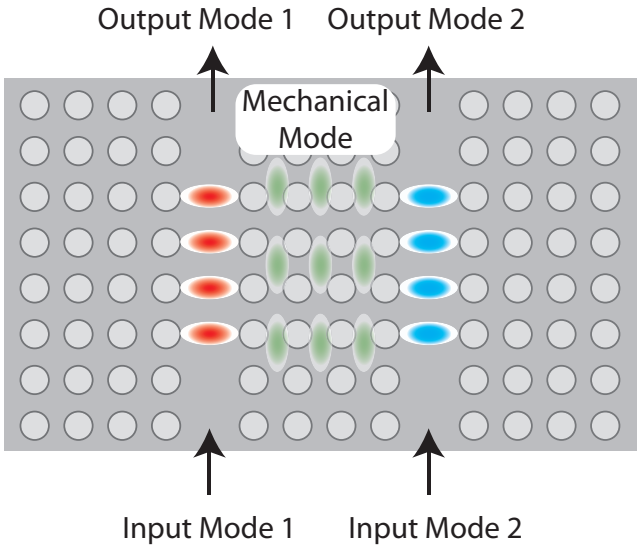

Figure 3.3: Schematic double-cavity OMS in photonic crystals with two optical modes coupled to a common mechanical mode between them.

The deformation of the lattice structure effectively modulates the optical resonance frequency leading to high optomechanical coupling strength. Considering defects can be fabricated flexibly with photolithography, one can prepare two optical waveguides adjacent to each other coupling to the same mechanical mode. Thus, a double-cavity OMS is realized.

3.2 Model of double-cavity OMS

Now we analyze the double-cavity OMS and provide its Hamiltonian. For the purpose of modelling its physics quantities, we show the schematic in Fig. 3.4. For each

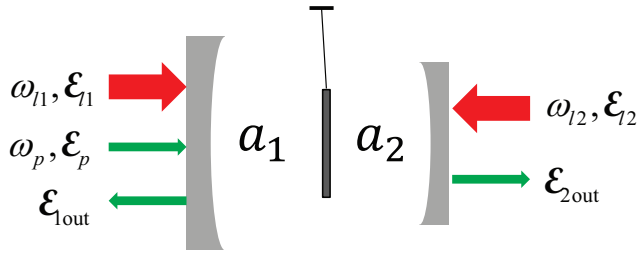

Figure 3.4: Schematic double-cavity OMS.

cavity, we denote its field by a_i, frequency by ω_{ci} and decay rate by κ_i, $i = 1, 2$. The field annihilation and creation operators satisfy the commutation relation $[a_i, a_j^\dagger] = \delta_{ij}$. In this section, we ignore the internal decay and set $\eta = 1$. A probe laser with frequency ω_p, is sent into cavity 1. The two cavities are coupled only via the oscillations of the mechanical mirror with the oscillations produced by the applied strong laser fields $\mathcal{E}_{li}$'s. Further the two cavities can be in different frequency regimes. We use the normalized coordinates $Q = \sqrt{m\omega_m/\hbar}q$ and $P = \sqrt{1/(m\hbar\omega_m)}p$ for the mechanical oscillator with commutation relations $[Q, P] = [q, p]/\hbar = i$. We also define the coupling coefficients g_i, driving laser amplitude $\mathcal{E}_{li}$ for each cavity $i = 1, 2$. The probe laser is applied only to cavity 1. Then the Hamiltonian for this system is given by

$$
\begin{aligned}
H &= H_1 + H_2 + H_m + H_{\text{diss}}, \\
H_1 &= \hbar(\omega_{c1} - \omega_{l1})a_1^\dagger a_1 - \hbar\sqrt{2}g_1 a_1^\dagger a_1 Q + i\hbar\mathcal{E}_{l1}(a_1^\dagger - a_1) + i\hbar(\mathcal{E}_p a_1^\dagger \mathrm{e}^{-i\delta t} - \mathcal{E}_p^* a_1 \mathrm{e}^{i\delta t}) \\
H_2 &= \hbar(\omega_{c2} - \omega_{l2})a_2^\dagger a_2 + \hbar\sqrt{2}g_2 a_2^\dagger a_2 Q + i\hbar\mathcal{E}_{l2}(a_2^\dagger - a_2) \\
H_m &= \frac{1}{2}\hbar\omega_m(P^2 + Q^2),
\end{aligned}
\tag{3.1}
$$

where $\delta = \omega_p - \omega_{l1}$ is the detuning between the probe field and the driving field in cavity 1. All the dissipative interactions are denoted by H_{diss}. These include the leakage of photons from both cavities and the damping of the mirror oscillation. Note that the optomechanical coupling terms g_1 and g_2 are different by their signs because a certain mechanical displacement Q increases the resonance frequency of one cavity while decreases that of the other one. The Hamiltonian (3.1) has been written by working in a picture in which the very fast frequencies ω_{li}'s are removed. This results in detuning terms like $(\omega_{ci} - \omega_{li})a_i^\dagger a_i$. The equations of motion for Q, P, a_i and $a_i^\dagger$

are found to be

$$\begin{aligned}
\dot{Q} &= \omega_m P, \\
\dot{P} &= \sqrt{2}(g_1 a_1^\dagger a_1 - g_2 a_2^\dagger a_2) - \omega_m Q - \gamma_m P, \\
\dot{a}_1 &= -i(\omega_{c1} - \omega_{l1} - \sqrt{2} g_1 Q) a_1 - \kappa_1 a_1 + \mathcal{E}_{l1} + \mathcal{E}_p \mathrm{e}^{-\mathrm{i}\delta \mathrm{t}}, \\
\dot{a}_2 &= -i(\omega_{c2} - \omega_{l2} + \sqrt{2} g_2 Q) a_2 - \kappa_2 a_2 + \mathcal{E}_{l2}.
\end{aligned} \tag{3.2}$$

We notice that the coupled equations contain nonlinear terms including $g_1 a_1^\dagger a_1$, $g_1 Q a_1$ and similar terms involving a_2. However, Eqs. (3.2) involve periodically oscillating terms hence in the long time limit, any of the fields and the mechanical coordinates will have a solution of the form $A = \sum_{n=-\infty}^{+\infty} \mathrm{e}^{-in\delta t} A_n$. The A_n's can be obtained by Floquet analysis. In the long-time limit, $\dot{A} = 0$ and the time differentiations can be expanded as

$$\dot{A} = -i\delta e^{-i\delta t} A_+ + i\delta e^{i\delta t} A_-, \qquad A = Q, P, a_1, a_2. \tag{3.3}$$

We expand the nonlinear terms to the first order such that

$$\begin{aligned}
a_1^\dagger a_1 &= (a_{10}^* + a_{1-} e^{-i\delta t} + a_{1+} e^{i\delta t})(a_{10} + a_{1-} e^{i\delta t} + a_{1+} e^{-i\delta t}) \\
&\cong |a_{10}|^2 + (a_{10}^* a_{1+} + a_{10} a_{1-}) e^{-i\delta t} + (a_{10} a_{1+} + a_{10}^* a_{1-}) e^{i\delta t},
\end{aligned} \tag{3.4}$$

and similarly we get

$$a_2^\dagger a_2 \cong |a_{20}|^2 + (a_{20}^* a_{2+} + a_{20} a_{2-}) e^{-i\delta t} + (a_{20} a_{2+} + a_{20}^* a_{2-}) e^{i\delta t}. \tag{3.5}$$

In the last step, I dropped the higher order terms. We assume that the probe is much weaker than the coupling field; then the A_n's can be obtained perturbatively. The equations of motion up to first order perturbation in $|\mathcal{E}_p/\mathcal{E}_{li}|$ in the long time limit

can be given as

$$
\begin{aligned}
&-i\delta e^{-i\delta t}Q_+ + i\delta e^{i\delta t}Q_- = \omega_m P_0 + \omega_m e^{-i\delta t}P_+ + \omega_m e^{i\delta t}P_-,\\
&-i\delta e^{-i\delta t}P_+ + i\delta e^{i\delta t}P_- = \sqrt{2}g_1(|a_{10}|^2 + (a_{10}^* a_{1+} + a_{10}a_{1-})e^{-i\delta t} + (a_{10}a_{1+} + a_{10}^* a_{1-})e^{i\delta t})\\
&\quad - \sqrt{2}g_2(|a_{20}|^2 + (a_{20}^* a_{2+} + a_{20}a_{2-})e^{-i\delta t} + (a_{20}a_{2+} + a_{20}^* a_{2-})e^{i\delta t})\\
&\quad - \omega_m(Q_0 + Q_- e^{i\delta t} + Q_+ e^{-i\delta t}) - \gamma_m(P_0 + P_- e^{i\delta t} + P_+ e^{-i\delta t}).
\end{aligned}
\tag{3.6}
$$

If we compare the terms oscillating as $e^{\pm i\delta t}$, we can obtain the steady-state solution of the mechanical states

$$
P_0 = 0, \qquad Q_0 = \frac{\sqrt{2}}{\omega_m}(g_1|a_{10}|^2 - g_2|a_{20}|^2), \tag{3.7}
$$

and

$$
\omega_m P_+ = -i\delta Q_+, \qquad \omega_m P_- = i\delta Q_-. \tag{3.8}
$$

The vanishing value of P_0 means the mechanical mirror stays at a certain displacement Q_0, which is typically small. The steady state value of Q_0 is determined by the mechanical restoring force and the difference of radiation pressures from both cavities. We continue to write down the equations for the optical modes

$$
\begin{aligned}
&-i\delta e^{-i\delta t}a_{1+} + i\delta e^{i\delta t}a_{1-} = -\kappa_1(a_{10} + a_{1-}e^{i\delta t} + a_{1+}e^{-i\delta t}) + \mathcal{E}_{l1} + \mathcal{E}_p \mathrm{e}^{-\mathrm{i}\delta \mathrm{t}}\\
&\quad - i[\omega_{c1} - \omega_{l1} - \sqrt{2}g_1(Q_0 + Q_- e^{i\delta t} + Q_+ e^{-i\delta t})](a_{10} + a_{1-}e^{i\delta t} + a_{1+}e^{-i\delta t}),\\
&-i\delta e^{-i\delta t}a_{2+} + i\delta e^{i\delta t}a_{2-} = -\kappa_2(a_{20} + a_{2-}e^{i\delta t} + a_{2+}e^{-i\delta t}) + \mathcal{E}_{l2}\\
&\quad - i[\omega_{c2} - \omega_{l2} + \sqrt{2}g_2(Q_0 + Q_- e^{i\delta t} + Q_+ e^{-i\delta t})](a_{20} + a_{2-}e^{i\delta t} + a_{2+}e^{-i\delta t}).
\end{aligned}
\tag{3.9}
$$

By comparing the terms oscillating at different frequencies and combining Eqs. (3.6), we obtain the mean value steady state of the cavity field

$$
a_{10} = \frac{\mathcal{E}_{l1}}{\kappa_1 + i\Delta_1}, \qquad a_{20} = \frac{\mathcal{E}_{l2}}{\kappa_2 + i\Delta_2}, \tag{3.10}
$$

and the first order results in $|\mathcal{E}_p/\mathcal{E}_{li}|$

$$
\begin{aligned}
Q_+ &= -\frac{1}{d(\delta)}\frac{\sqrt{2}g_1 a_{10}^* \mathcal{E}_p}{(\kappa_1 + i\Delta_1 - i\delta)}, \\
d(\delta) &= \sum_{i=1,2}\frac{2\Delta_i g_i^2 |a_{i0}|^2}{(\kappa_i - i\delta)^2 + \Delta_i^2} - \frac{\omega_m^2 - \delta^2 - i\delta\gamma_m}{\omega_m}, \\
a_{1+} &= \frac{i\sqrt{2}g_1 a_{10}}{(\kappa_1 + i\Delta_1 - i\delta)}Q_+ + \frac{\mathcal{E}_p}{(\kappa_1 + i\Delta_1 - i\delta)}, \\
a_{1-} &= \frac{-i\sqrt{2}g_1 a_{10}^*}{(\kappa_1 - i\Delta_1 - i\delta)}Q_+^*, \\
a_{2+} &= \frac{-i\sqrt{2}g_2 a_{20}}{(\kappa_2 + i\Delta_2 - i\delta)}Q_+, \\
a_{2-} &= \frac{i\sqrt{2}g_2 a_{20}^*}{(\kappa_2 - i\Delta_2 - i\delta)}Q_+^*,
\end{aligned}
\tag{3.11}
$$

where $\Delta_1 = \omega_1 - \omega_{c1} - \sqrt{2}g_1 Q_0$ and $\Delta_2 = \omega_2 - \omega_{c2} + \sqrt{2}g_2 Q_0$ are the detunings of the coupling lasers to the effective cavity frequencies. The driving laser enhanced coupling coefficient is defined as $G_i = a_{i0}g_i$ for each cavity. The fields $a_{i\pm}$'s are the anti-Stokes and Stokes fields in the i'th cavity. The output fields from the two cavities are given by

$$
\begin{aligned}
\mathcal{E}_{1out} &= 2\kappa_1(a_{10}\mathrm{e}^{-i\omega_{l1}t} + a_{1+}\mathrm{e}^{-i(\omega_{l1}+\delta)t} + a_{1-}\mathrm{e}^{-i(\omega_{l1}-\delta)t}) - \mathcal{E}_p\mathrm{e}^{-i\omega_p t} - \mathcal{E}_{l1}\mathrm{e}^{-i\omega_{l1}t}, \\
\mathcal{E}_{2out} &= 2\kappa_2(a_{20}\mathrm{e}^{-i\omega_{l2}t} + a_{2+}\mathrm{e}^{-i(\omega_{l2}+\delta)t} + a_{2-}\mathrm{e}^{-i(\omega_{l2}-\delta)t}) - \mathcal{E}_{l2}\mathrm{e}^{-i\omega_{l2}t}.
\end{aligned}
\tag{3.12}
$$

The form of the output fields shows that it has multiple components oscillating at different frequencies. The terms outside the brackets are the input fields including the probe field $\mathcal{E}_p$ and the driving fields $\mathcal{E}_{li}$. The terms inside the brackets denote the fields generated by the optomechanical interactions and they include the field mean values at frequency ω_{li}, the anti-Stokes sideband at frequency $\omega_{li} - \delta$ and the Stokes sideband at frequency $\omega_{li} + \delta$. Their coefficients a_{i0} and $a_{i\pm}$ refer to the amplitudes of these frequency components. Recalling the frequency relation $\omega_p = \omega_{l1} + \delta$, we find that the anti-Stokes sideband of the driving field overlaps the probe field in its frequencies. Coherent effects in OMS can be enhanced and observed when the amplitude a_{10} is prominent. We also find that, although no probe field is injected to

cavity 2, multiple components arise in it.

3.3 Electromagnetically Induced Absorption in OMS

We now focus on analyzing the intracavity field by using Eqs.(3.12). If both of the driving fields are red-detuned by the mechanical resonance frequency, *i.e.* $\Delta_1 = \Delta_2 = \omega_m$, the field a_{i+} would be oscillating at the probe frequency ω_p. After the approximation $\Delta + \delta \approx 2\Delta$, the intra-cavity optical field amplitude $\mathcal{E}_c$ at frequency ω_p can be calculated as

$$\begin{aligned}
\mathcal{E}_c &= 2\kappa_1 a_{1+} \\
&\cong \frac{2i\kappa_1 \mathcal{E}_p}{(\delta - \omega_m + i\kappa_1) - \dfrac{|G_1|^2}{(\delta - \omega_m + i\gamma_m/2) - \dfrac{|G_2|^2}{(\delta - \omega_m + i\kappa_2)}}} \\
&= \frac{2\mathcal{E}_p}{(1 - i\frac{\delta-\omega_m}{\kappa_1}) + \dfrac{C_1}{(1 - i\frac{\delta-\omega_m}{\gamma_m/2}) + \dfrac{C_2}{(1 - i\frac{\delta-\omega_m}{\kappa_2})}}}.
\end{aligned} \tag{3.13}$$

Note that $\delta = \omega_p - \omega_{l1}$ is detuning from the probe laser frequency to the driving laser frequency and it is close to ω_m. $C_{1,2} = 2|G_{1,2}|^2/(\kappa_{1,2}\gamma_m)$ is the cooperativity parameter for each cavity i. The structure of Eq. (3.13) is very interesting. It shows how the resonant character of the output field changes from that of an empty cavity ($C_1 = C_2 = 0$) to that of a single cavity ($C_2 = 0, C_1 \neq 0$) and further to that of double cavities ($C_1, C_2 \neq 0$). Its denominator is linear in ω_p for an empty cavity, quadratic in ω_p for a single cavity, and cubic in ω_p for double cavities. These changes determine the physical behavior of the OMS. We first note that for $C = 0$, we have the standard EIT behavior (black dotted curves and the insets). Below the strong

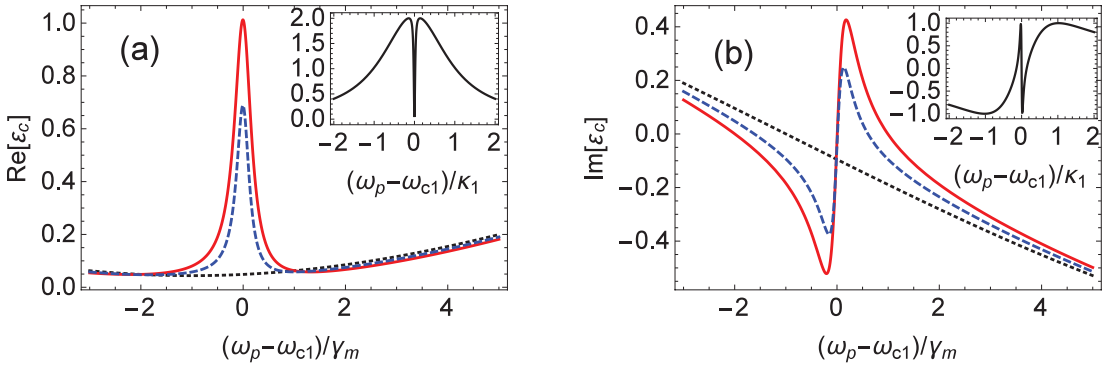

Figure 3.5: The real (a) and imaginary (b) part of the intra-caity field amplitude $\mathcal{E}_c$. The black dotted, blue dashed and red solid curves are corresponding to the cooperativity ratios $C_2/C_1 = 0, 0.5, 1$, respectively, and $C_1 = 40$. The response shows EIT when only one coupling field is present, and the emergence of EIA at the line center when both coupling fields are present. The insets show the EIT in a large frequency span with $C_2 = 0$, i.e. with no coupling field applied to the second cavity.

coupling regime ($|G_1| < \kappa_1$ in the limit $\gamma_m \to 0$), the two roots of the denominator in Eq. (3.13 are purely imaginary. The interference then leads to the EIT window with a width $\Gamma_{\rm EIT} = (1 + C_1)\gamma_m/2$. The usual normal-mode splitting [86] occurs when the two roots have nonzero real parts, i.e. $|G_1| > \kappa_1$. Clearly, if we want to produce an absorption peak within the EIT window, then we need to choose C_2 such that the third root of the denominator in Eq. (3.13) lies within the EIT window. For the results shown in Fig. 3.5, we choose $C_2 = C_1/2$ (blue dashed curves) and $C_2 = C_1$ (red solid curves). In Fig. 3.6, we show how the roots of the denominator in Eq. (3.13) change for $|G_1| < \kappa_1$ and if the driving field in cavity 2 is increased. For $C_2 = 0$, the width of the EIT window is $20.5\gamma_m$. Curve **c** gives the overall width within which the transparency window appears. Curve **a** gives the width of the EIA peak within the EIT window.

We now examine quantitatively the width of the absorption peak. When $G_2 = 0$, $|G_1| < \kappa_1$, the two roots of the denominators in (3.13) are κ_1 and $\Gamma_{\rm EIT}$, and $\Gamma_{\rm EIT} \ll \kappa_1$.

In the presence of the additional coupling field $a_{20} \neq 0$, the root $\Gamma_{\rm EIT}$ splits into two parts

$$\Gamma_{\rm EIT} \rightarrow \Gamma_{\pm} = \frac{1}{2}\Gamma_{\rm EIT} \pm \frac{1}{2}\sqrt{\Gamma_{\rm EIT}^2 - 4|G_2|^2},$$
$$\Gamma_{-} = \Gamma_{\rm EIA} \approx \kappa_2 + \frac{|G_2|^2}{2\Gamma_{\rm EIT}}, \quad \text{if } \frac{|G_2|^2}{4\Gamma_{\rm EIT}^2} \ll 1. \tag{3.14}$$

The existence of an additional splitting in roots $\Gamma_{\pm}$, especially when $\kappa_2 \ll \Gamma_{\rm EIT}$, leads to the absorption peak within the transparency window. The half width of the absorption peak is given by $\kappa_2 + |G_2|^2/(2\Gamma_{\rm EIT})$. It should be borne in mind that the microwave cavity is especially useful as $\kappa_2 \ll \gamma_m, \Gamma_{\rm EIT}$. Root Γ_{-} has the behavior given by curve **a** in Fig. 3.6.

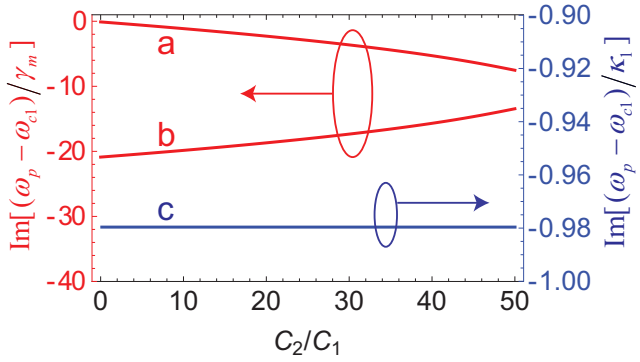

Figure 3.6: The real (a) and imaginary (b) part of the field amplitude $2\kappa_1 a$. The blue curves show the Lorentzian response to the probe of an empty cavity; the red curves show EIT of a single driven OMS; and the black curves show the EIA peak when both the optical and electric cavities are driven by red-detuned fields.

Figure 3.5 also illustrates the absorption and dispersion character of the OMS under the condition $\kappa_1 \gg \gamma_m \gg \kappa_2$. In Fig. 3.5(a), we see that the Lorentzian profile (blue curves) for an non-driven empty cavity turns into an EIT profile (red curve) when a single driving field is applied in the optical cavity. When we turn on also the electro driving field, an extremely sharp absorption window (black curve) emerges in the center of the EIT profile. According to the Kramers-Kronig relations, an anomaly

in the absorption spectrum is always accompanied by an anomaly in the dispersion. In the case of EIT/EIA, the signal field experiences a large normal/anomaly dispersion, which implies reduction/enhancing of the group velocity. In Fig. 3.5(b), the red curve, corresponding to the case when a single optical driving field is applied, shows a large anomaly dispersion in the central frequency indicating the existence of slow light effect. When both the optical and electro driving fields are applied, the black curve shows an extremely sharp normal dispersion. This implies an enhancement of the dispersion by a large factor and one can realize superluminal effects.

The EIA within the transparency window is quite generic and is applicable to a variety of systems. We are able to show the existence of EIA using three coupled oscillators. Note that the coupled oscillator models can very often mimic a variety of physical phenomena. In fact two coupled oscillators [87–89] have been used to understand EIT as well as EIA. It turns out that the EIA of the type discussed in this chapter has to be understood in terms of three coupled oscillators — in our case two of these (u and v) would represent cavity modes and the third one (w) would represent the mechanical oscillator. The three effective oscillators can be described by equations (written in rotating wave approximation) as

$$\begin{cases} \dot{u} = -\mathrm{i}\Delta_1 u - \mathrm{i}G_1 w - \kappa_1 u + \mathcal{E}_p \mathrm{e}^{-\mathrm{i}\delta t}, \\ \dot{v} = -\mathrm{i}\Delta_2 v - \mathrm{i}G_2 w - \kappa_2 v, \\ \dot{w} = -\mathrm{i}\omega_m w - \mathrm{i}G_1 u - \mathrm{i}G_2 v - (\gamma_m/2) w. \end{cases} \tag{3.15}$$

These three coupled equations can exhibit a variety of phenomena depending on the couplings G_1, G_2 and the relaxation parameters κ_1, κ_2 and γ_m. For the existence of the EIA, it is simple to have $\kappa_1 \gg \gamma_m \gg \kappa_2$. Note that a whole class of hybrid systems coupling optical and microwave systems can be described by Eqs. (3.15) and their quantum version in terms of Langevin equations [*cf.* Eqs. (1.13)].

3.4 Experimental implementation in Metamaterials

Collaborating with Prof. Weili Zhang, we experimentally realized EIA in three-layered metamaterials. The schematic diagram of a three-layered metamaterial unit cell is shown in Fig. 3.7(a), (b), and (c). The three resonators, namely, an I-shaped structure on the top layer, a four-SRR (Split-ring resonator) at the middle layer and a cut wire structure on the bottom layer. The resonator on each layer has a single resonance peak all with different widths. When they are fabricated together so that they couple coherently, we successfully observe the EIA peak in the transmission spectra as illustrated in Fig. 3.7d.

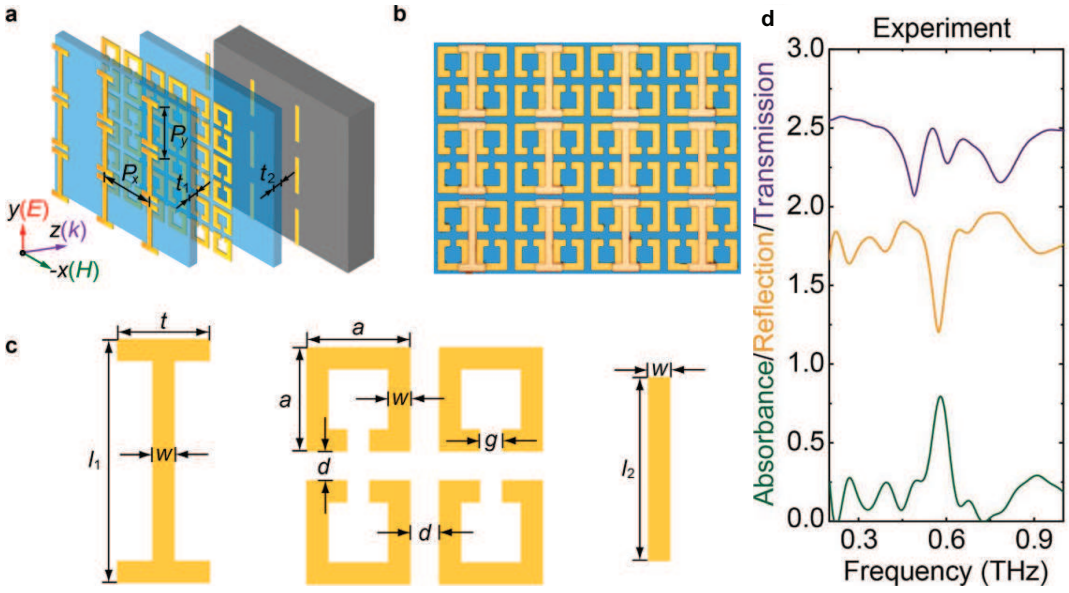

Figure 3.7: (a) Schematic diagram of the three-layered EIA metasurface unit cell. (b) Microscopic image of the EIA sample. It was fabricated on a silicon substrate and the dielectric spacer is made from polyimide. (c) Schematic of the individual resonators. (d) The experiment spectra of the amplitude transmission, reflection and absorbance.

The EIA in metamaterials gives a way for a strong absorption resonance in the transmission spectrum to occur without compromising high transmission amplitude

except at the EIA window. This three-resonator design delivers a strong EIA up to 78% which is much stronger than that in existing two resonator metamaterial systems. Besides, along with the EIA resonance, the original transparent window splits into a double-peak EIT-like behavior, which could be useful in developing slow-light devices with dual band transparency. From simulations, we also found that the response of the EIA system reveals strong interlayer distance dependence. As in other coupled-resonator systems, the transmission and reflection spectra are very sensitive to the position of the SRRs in the polyimide layer which determines its coupling strength to the top and the bottom structures. A very small variation in the vertical or horizontal position of the SRRs leads to an apparent modification in the spectral response.

3.5 Coherent state transfer

Whenever there is an absorption window, one would naturally ask "where do the energies go?". The answer is that the energy transfers from cavity 1 to cavity 2 via the mediating mechanical oscillating resonator. Let us take an example of an experimentally realized double-cavity OMS, whose cavity 1 is an optical cavity with a large decay rate and cavity 2 is an electric cavity with a very low decay rate. In Fig. 3.8, the dashed curves show the case that the double-cavity OMS is solely driven by the optical drive, in which case we find the probe field to be perfectly reflected to the optical output due to the EIT and the mechanical mode to be excited. When we turn on both the optical and electrical driving fields, we find the optical probe field to be totally absorbed in the EIA window and the energy to be transferred to the electrical cavity. More interestingly, the mechanical mode is in a "dark state" [19], *i.e.* it is not excited. Overall, the optical probe field is transferred to the electric field via the mechanical mode without exciting the mechanical mode!

In a publication [84] by Lehnert's group, they demonstrate a converter that provides a bidirectional, coherent and efficient conversion of classical signals between

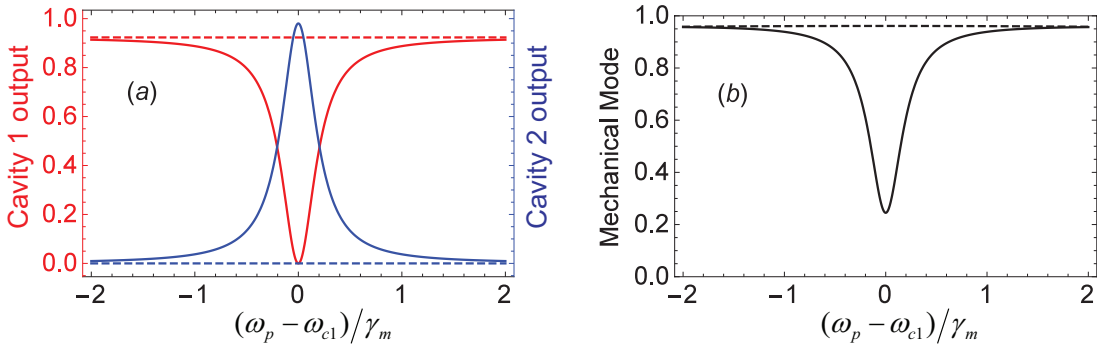

Figure 3.8: (a) The normalized output from the first cavity (optical) and from the second cavity (electrical); and (b) the amplitude of the mechanical displacement normalized to $|\mathcal{E}_p|^2$. The system behaves (almost) as a perfect reflection with a bright mechanical mode when $C_2 = 0$ (dashed curves); and it behaves as a perfect transmission with a nearly dark mechanical mode when $C_1 = C_2$ (solid curves).

microwave (of 7 GHz) and optical light (of 282 THz) assisted by a mechanical mode (of the order of 1 MHz). The conversion efficiencies are $\sim 10\%$ at an environment temperature of 4 K. This unique design which couples an optical cavity with an electric cavity could even be useful to convert microwave and optical photons, a wavelength conversion problem that has attracted more and more interest [14, 68, 82, 83, 90]. Recently, Superconducting Josephson junction-based qubits and superconducting resonant cavities have emerged as the ideal realization of quantum two-level systems interacting with a single mode of the electromagnetic spectrum. It provides a highly flexible platform for creating on-demand complex quantum states of a light field. Combining with the EIA-based wavelength conversion technique, one can efficiently convert the microwave quantum state to optical wavelengths, hence they could be transmitted over kilometer distances with negligible loss. They could then be stored for long times in, for instance, atomic ensembles or even an OMS.

3.6 Transduction of fields in a double-cavity OMS

Converting low-frequency electrical signals into much higher-frequency optical signals has greatly boosted the development of modern communication networks. It leverages the strengths of both the microelectrical circuits and optical fibre transmission. Current technologies of the conversion are mainly based on modulating the output of a laser diode controlled by electrical input signals. However, this method is subject to non-unitary, non-coherent transformation properties and large environmental bath noise. In light of the demands, I present the transduction of electromagnetic fields in a double-cavity OMS. The double-cavity OMS brings larger flexibility to the optical pulse storage protocol and applications. One can optimize these two independent cavities for their own functions with different parameters, like cavity decay rate, resonance frequency and coupling rate.

In this section, we focus on the system shown in Fig. 3.4, in which a mechanical resonator is coupled to two cavities. We display in Figs. 3.9 and 3.10 a series of output fields when the second cavity is red detuned, on resonance and blue detuned. We take $\kappa_2 = \kappa_1$ though additional flexibility in the operation of the memory device is possible by making them different. The fields at the output of the second cavity $\mathcal{E}_{2out}$ have Stokes and anti-Stokes components, whose central frequencies are given by $\omega_{c2} \pm \omega_m$. Their amplitudes a_{2+} and a_{2-} are related, respectively, by Eq. (3.12).

When the second cavity is red detuned, the anti-Stokes pulse is on resonance with the second cavity whereas the Stokes pulse is far off resonance. This is the reason of very little Stokes output. The anti-Stokes output can be comparable to the input probe pulse $\mathcal{E}_p$ depending on the power used to pump the second cavity. With higher applied power, the conversion of phonons to the anti-Stokes field is more efficient. If the second cavity is on resonance, then, as expected, the generated Stokes and anti-Stokes are of comparable magnitude. These curves clearly show that using the second cavity on resonance produces better coherent outputs than the case when

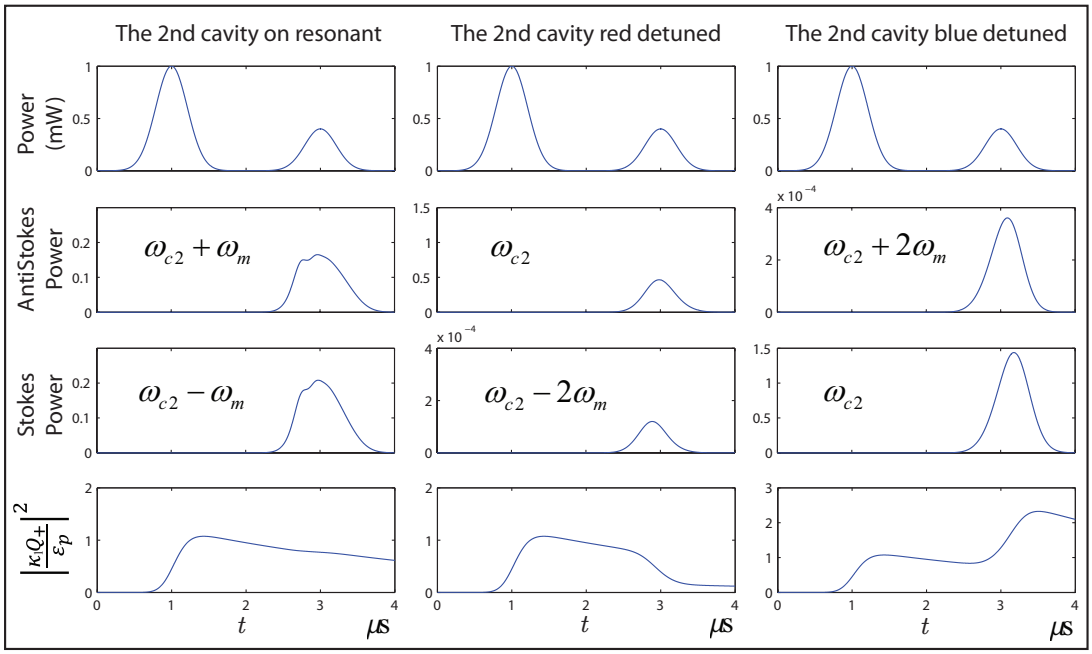

Figure 3.9: Numerical simulation of the optical memory using double-cavity OMS when the "reading" cavity frequency ω_{c2} is on resonant, red detuned and blue detuned with the reading laser frequency ω_R. The peak power is $P_L = 1\text{mW}$ for the writing coupling laser and $P_R = 0.4\text{mW}$ for the reading coupling laser.

the second cavity is red detuned. Note that the incident probe has a frequency $\omega_p = \omega_{l1} + \omega_m \approx \omega_{c1}$ whereas the outputs from the second cavity have frequencies $\omega_{l2} \pm \omega_m$. We have here phonon induced transduction of photon fields from a frequency ω_{l1} to frequency $\omega_{l2} \pm \omega_m$. We also produce two outputs.

For the case of the blue detuning of the second cavity $\omega_{c2} \approx \omega_{l2} + \omega_m$, the generated anti-Stokes field is far off resonance whereas the Stokes field is on resonance. Therefore a very significant amount of the Stokes field is generated. Furthermore, the blue detuned laser leads to the generation of coherent phonons as shown by Fig. 3.9. The nonlinear mixing process involving the field at ω_{l2} and phonons at ω_m produces the Stokes field at ω_{c2}. The increase of the phonon excitation can be understood from a quantum mechanical description of the process—the radiation matter interaction for

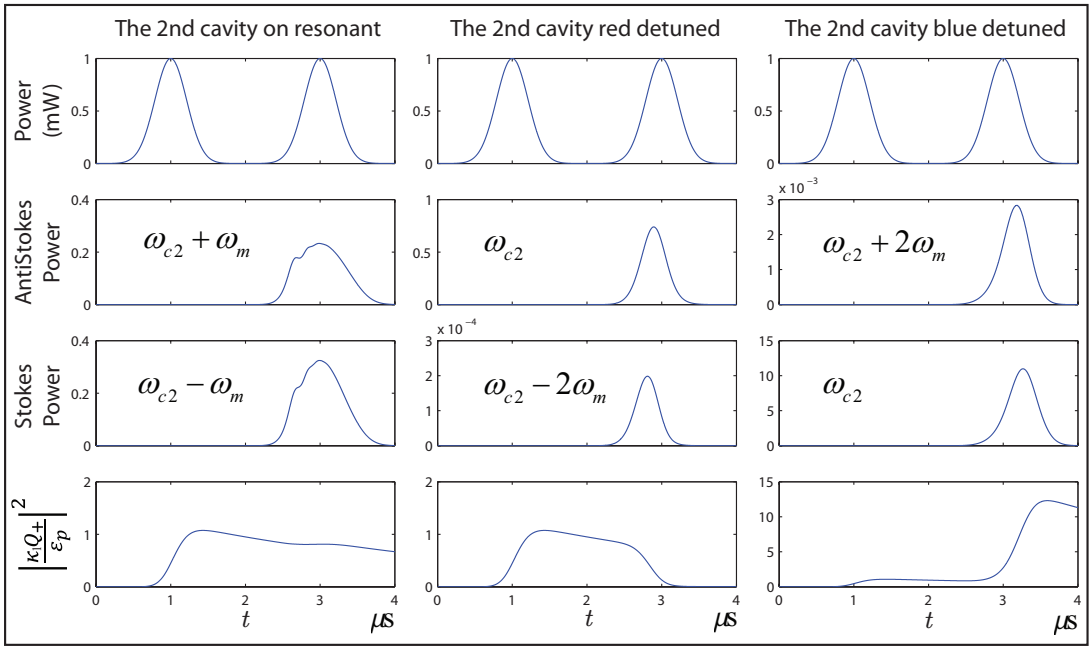

Figure 3.10: Numerical simulation of the optical memory using double-cavity OMS. Curves are defined similar to Fig. 3.9 except the peak power is $P_R = 1\text{mW}$ for the reading laser.

the second cavity is

$$(a_R e^{-i\omega_R t} + a_2 e^{-i\omega_2 t})^\dagger (a_R e^{-i\omega_R t} + a_2 e^{-i\omega_2 t})(Q_+ e^{-i\omega_m t} + Q_+^\dagger e^{i\omega_m t})$$
$$= (Q_+^\dagger a_2^\dagger a_R + H.c.) + \text{non resonant terms.} \tag{3.16}$$

This clearly shows how a photon of frequency ω_R gets converted into a phonon and a photon of frequency ω_{l2}. In Fig. 3.10, we show the output fields from the second cavity when the field driving the second cavity is large. The idea here is to see how well a very weak pulse applied at the frequency ω_p from the left would be recovered. Fig. 3.10 shows that the recovery is good. This should be especially relevant for the transduction of single photons. These results show how the coherently generated phonons in the first cavity can be used for the transduction of the optical fields. If the second cavity were a microwave cavity driven by microwave field, then one has the possibility of converting incident optical fields into microwave fields.

3.7 Summary

To summarize the results, we have demonstrated the possibility of EIA within the transparency window of the optomechanical systems. For the OEMS we studied, the EIA results in the transduction of optical fields to microwave fields. Note however that the transduction of fields at single photon levels would require a full quantum treatment as in [63]. The EIA within the transparency window is quite generic and is applicable to a variety of systems, and can effectively be described by three coupled oscillators. These systems would include other types of optomechanical systems such as those containing two mechanical elements [91, 92], two qubits [93], or very different classes of systems such as plasmonic structures [94, 95] and metamaterials [54].

CHAPTER 4

FANO RESONANCE IN OMS

Fano line profiles, originally discovered in the context of photoionization, have been found to occur in a large class of systems such as resonators, metamaterials, and plasmonics. Optomechanics which couples an optical oscillator to a mechanical one is not the only way to observe such resonances by identifying the interfering contributions to the fields generated at anti-Stokes and Stokes frequencies. However, unlike the atomic systems, OMS provides great flexibility as the width of the resonance is controlled by the coupling field. In this chapter, I first briefly introduce the origin and concept of Fano resonances. Then I present my study of Fano resonances in both single-cavity OMS and double-cavity OMS. In the end, I find the quantum signature of Fano resonance, *i.e.* quantum vacuum fluctuation of the cavity output field showing Fano resonance.

4.1 Physical model of Fano resonance

In the classic work [96], Fano considered the photoionization process when a weakly bound state $|a\rangle$ lies in the continuum $|E\rangle$. The weakly bound state has a finite life time due to its coupling with the continuum. Thus, in the simplest case, there are two transition amplitudes leading to photoionization: one involves a direct transition to the continuum and the other involves transition via the autoionizing state to the continuum. These two transition amplitudes interfere leading to the famous Fano

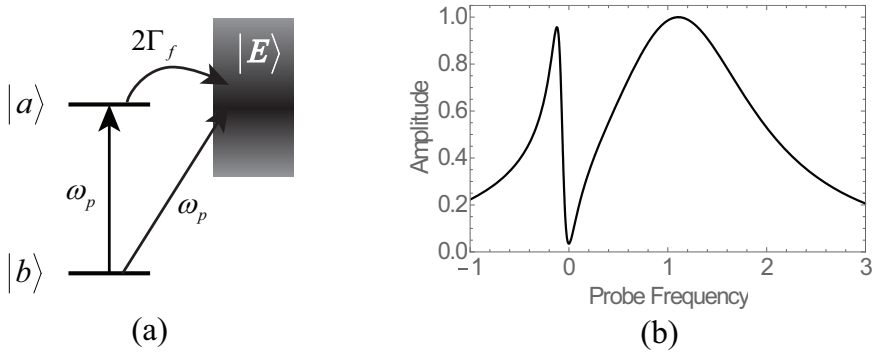

Figure 4.1: (a) Fano interference between the transitions $|b\rangle \to |E\rangle$ and $|b\rangle \to |a\rangle \to |E\rangle$. (b) Shape of Fano resonance.

formula for the probability p for the photoionization

$$p(E) = \frac{(\epsilon + q_f)^2}{\epsilon^2 + 1}, \qquad \epsilon = \frac{2(E - E_a)}{\Gamma_f}, \tag{4.1}$$

where q_f is called the Fano asymmetry parameter and Γ_f is the width of the state $|a\rangle$. The Fano minimum occurs at $\epsilon = -q_f$. The parameter q_f depends on the relative strengths of the independent transitions to the states $|a\rangle$ and $|E\rangle$. If q_f is large, interference disappears.

In order to observe Fano resonance in OMS, we concentrate on the same double-cavity optomechanical system shown in Fig. 4.2 as we studied in the previous section. For each cavity, we denote its field by a_i, frequency ω_{ci} and decay rate κ_i, $i = 1, 2$. The

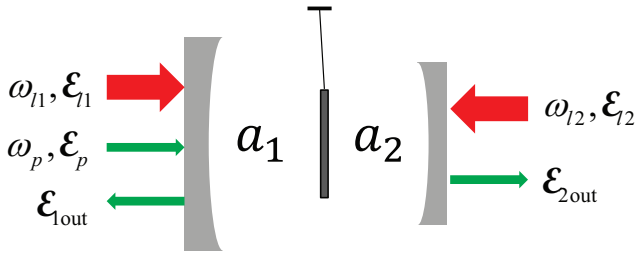

Figure 4.2: Schematic double-cavity OMS.

field annihilation and creation operators satisfy the commutation relation $[a_i, a_j^\dagger] = \delta_{ij}$. In this section, we ignore the internal decay and set $\eta = 1$. The probe laser

with frequency ω_p, is sent into cavity 1. The two cavities are coupled only via the oscillations of the mechanical mirror which are produced by the applied strong laser fields $\mathcal{E}_{li}$'s. Further the two cavities can be in different frequency regimes. We use the normalized coordinates $Q = \sqrt{m\omega_m/\hbar}q$ and $P = \sqrt{1/(m\hbar\omega_m)}p$ for the mechanical oscillator with commutation relations $[Q, P] = [q, p]/\hbar = i$. We define the coupling coefficients g_i, driving laser amplitude $\mathcal{E}_{li}$ for each cavity $i = 1, 2$. The probe laser is applied only to cavity 1. Then the Hamiltonian for this system is given by

$$\begin{aligned}
H &= H_1 + H_2 + H_m + H_{\text{diss}}, \\
H_1 &= \hbar(\omega_{c1} - \omega_{l1})a_1^\dagger a_1 - \hbar\sqrt{2}g_1 a_1^\dagger a_1 Q + i\hbar\mathcal{E}_{l1}(a_1^\dagger - a_1) + i\hbar(\mathcal{E}_p a_1^\dagger \mathrm{e}^{-i\delta t} - \mathcal{E}_p^* a_1 \mathrm{e}^{i\delta t}) \\
H_2 &= \hbar(\omega_{c2} - \omega_{l2})a_2^\dagger a_2 + \hbar\sqrt{2}g_2 a_2^\dagger a_2 Q + i\hbar\mathcal{E}_{l2}(a_2^\dagger - a_2) \\
H_m &= \frac{1}{2}\hbar\omega_m(P^2 + Q^2),
\end{aligned} \tag{4.2}$$

where $\delta = \omega_p - \omega_{l1}$ is the detuning between the probe field and the driving field in cavity 1. All the dissipative interactions are denoted by H_{diss}. These include the leakage of photons from both cavities and the damping of the mirror oscillation. Note that the optomechanical coupling terms g_1 and g_2 are different by their signs because a certain mechanical displacement Q increases the resonance frequency of one cavity while decreases that of the other one. The Hamiltonian (3.1) has been written by working in a picture so the very fast frequencies ω_{li}'s are removed. This results in detuning terms like $(\omega_{ci} - \omega_{li})a_i^\dagger a_i$. The equations of motion for Q, P, a_i and $a_i^\dagger$ are found to be

$$\begin{aligned}
\dot{Q} &= \omega_m P, \\
\dot{P} &= \sqrt{2}(g_1 a_1^\dagger a_1 - g_2 a_2^\dagger a_2) - \omega_m Q - \gamma_m P, \\
\dot{a}_1 &= -i(\omega_{c1} - \omega_{l1} - \sqrt{2}g_1 Q)a_1 - \kappa_1 a_1 + \mathcal{E}_{l1} + \mathcal{E}_p \mathrm{e}^{-\mathrm{i}\delta\mathrm{t}}, \\
\dot{a}_2 &= -i(\omega_{c2} - \omega_{l2} + \sqrt{2}g_2 Q)a_2 - \kappa_2 a_2 + \mathcal{E}_{l2}.
\end{aligned} \tag{4.3}$$

The output fields from the two cavities are given by

$$\begin{aligned}\mathcal{E}_{1out} &= 2\kappa_1(a_{10}\mathrm{e}^{-i\omega_{l1}t} + a_{1+}\mathrm{e}^{-i(\omega_{l1}+\delta)t} + a_{1-}\mathrm{e}^{-i(\omega_{l1}-\delta)t}) - \mathcal{E}_p\mathrm{e}^{-i\omega_p t} - \mathcal{E}_{l1}\mathrm{e}^{-i\omega_{l1}t},\\ \mathcal{E}_{2out} &= 2\kappa_2(a_{20}\mathrm{e}^{-i\omega_{l2}t} + a_{2+}\mathrm{e}^{-i(\omega_{l2}+\delta)t} + a_{2-}\mathrm{e}^{-i(\omega_{l2}-\delta)t}) - \mathcal{E}_{l2}\mathrm{e}^{-i\omega_{l2}t}.\end{aligned} \tag{4.4}$$

The output fields in the form of Eq. (4.4) contain components at three different frequencies: the driving frequency ω_{l1}; the anti-Stokes frequency, which is also the probe frequency, $\omega_{l1} + \delta = \omega_p$; and the Stokes frequency $\omega_{l1} - \delta$. Among these three components, we are most interested in the generated anti-Stokes and Stokes sidebands and we display them as the normalized quantities defined by $\mathcal{E}_{ias} = 2\kappa_i a_{i+}/\mathcal{E}_p$ and $\mathcal{E}_{is} = 2\kappa_i a_{i-}/\mathcal{E}_p$. The actual normalized output field at the anti-Stokes frequency from the cavity 1 is given by $(\mathcal{E}_{1as} - 1)$, *cf.* Eq. (4.4). The anti-Stokes field would be resonantly enhanced in the vicinity of the cavity frequency ω_1, when both the coupling fields are tuned by an amount close to the mechanical frequency below their corresponding cavity frequency, i.e. $\Delta_1 \sim \omega_m$. The driving laser enhanced coupling efficient is defined as $G_i = a_{i0}g_i$ for each cavity. We work in the regime with cooperativity $C_i = 2|G_i|^2/\kappa_i\gamma_m > 1$ in which the OMS is strongly coupled, then the anti-Stokes and Stokes fields in cavity 1 are given by

$$\mathcal{E}_{1as} = \frac{2\kappa_1}{[\kappa_1 - i(\delta - \Delta_1)] + \dfrac{|G_1|^2}{[\frac{\gamma_m}{2} - i(\delta - \omega_m)] + \dfrac{|G_2|^2}{[\kappa_2 - i(\delta - \Delta_2)]}}}, \tag{4.5}$$

$$\mathcal{E}_{1s} = \frac{-i\kappa_1/\omega_m}{1 + \dfrac{[\kappa_1 + i(\delta - \Delta_1)]}{|G_1|^2}\left\{[\frac{\gamma_m}{2} + i(\delta - \omega_m)] + \dfrac{|G_2|^2}{[\kappa_2 + i(\delta - \Delta_2)]}\right\}}. \tag{4.6}$$

Similarly, the anti-Stokes and Stokes fields in cavity 2 are found to be

$$\mathcal{E}_{2as} = \frac{-2\kappa_2 \dfrac{G_1^*}{[\kappa_1 - i(\delta - \Delta_1)]} \dfrac{G_2}{[\kappa_2 - i(\delta - \Delta_2)]}}{\dfrac{|G_1|^2}{[\kappa_1 - i(\delta - \Delta_1)]} + \dfrac{|G_2|^2}{[\kappa_2 - i(\delta - \Delta_2)]} + [\frac{\gamma_m}{2} - i(\delta - \omega_m)]}, \tag{4.7}$$

$$\mathcal{E}_{2s} = \frac{\kappa_2 \dfrac{G_2^*}{\omega_m} \cdot \dfrac{G_1}{[\kappa_1 - i(\delta - \Delta_1)]}}{\dfrac{|G_1|^2}{[\kappa_1 + i(\delta - \Delta_1)]} + \dfrac{|G_2|^2}{[\kappa_2 + i(\delta - \Delta_2)]} + [\frac{\gamma_m}{2} + i(\delta - \omega_m)]}. \tag{4.8}$$

4.2 Fano resonance in single-cavity OMS

We examine now Fano resonances in the output fields. We have four different fields $\mathcal{E}_{ias}$, $\mathcal{E}_{is}$, and $i = 1, 2$. We first decouple cavity 2 by setting $G_2 = 0$. For this system, the anti-Stokes field is

$$\mathcal{E}_{1as} = \frac{2\kappa_1[\frac{\gamma_m}{2} - i(\omega_p - \omega_{l1} - \omega_m)]}{[\kappa_1 - i(\omega_p - \omega_{c1})][\frac{\gamma_m}{2} - i(\omega_p - \omega_{l1} - \omega_m)] + |G_1|^2}. \tag{4.9}$$

Typically the mechanical damping is much smaller than the cavity damping, $\gamma_m \ll \kappa_1$, and we work in the resolved sideband limit, $\omega_m \gg \kappa_1$. We expect two resonances: (i) when the probe is around the cavity frequency $\omega_p \approx \omega_{c1}$, and (ii) when it is around the anti-Stokes sideband of the driving laser $\omega_p \approx \omega_{l1} + \omega_m$. In order to keep these two resonances distinct, we define a nonzero frequency offset $\Omega_1 = \Delta_1 - \omega_m \neq 0$, *i.e.* $\omega_{c1} \neq \omega_{l1} + \omega_m$. For clarity, we show the relations between different frequencies in Fig. 4.3. The resonance at $\omega_p = \omega_{l1} + \omega_m$ would have a width in the order of $\Gamma_{\rm EIT}(\ll \kappa_1)$. The frequency offset factor Ω_1 plays an important role in the production of the Fano line shapes. Physically it means that the anti-Stokes process is not resonant with the cavity frequency. We examine the structure of $\mathcal{E}_{as1}$ near the resonance $\omega_p = \omega_{l1} + \omega_m = \omega_{c1} - \Omega_1$ for a fixed value of Ω_1, and we define $y = \omega_p - \omega_{c1} + \Omega_1$.

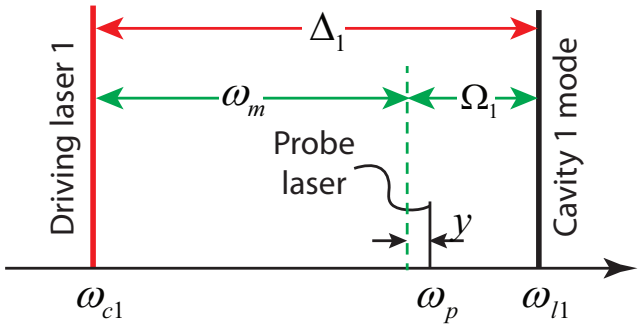

Figure 4.3: Schematic illustration of frequencies used in obtaining Fano lineshapes. Fano asymmetry parameter q_f is defined in terms of detuning $q_f = -\Omega_1/\kappa_1$. The effective damping is defined by $\Gamma_{f1} = |G_1|^2/[\kappa_1(1+q_f^2)]$.

In the vicinity of this resonance, $y \sim 0$ and Eq. (4.9) can be approximated to

$$\begin{aligned}\mathcal{E}_{1as} &\approx \frac{2\kappa_1(\gamma_m/2 - iy)}{(\kappa_1 + i\Omega_1)(\gamma_m/2 - iy) + |G_1|^2} \\ &\approx \frac{2\kappa_1}{\kappa_1 + i\Omega_1} \cdot \frac{y}{y + \frac{i|G_1|^2}{\kappa_1 + i\Omega_1}},\end{aligned} \tag{4.10}$$

and hence it can be simplified to such a form similar to (4.1)

$$Re[\mathcal{E}_{1as}] = \frac{2}{1+q_f^2} \cdot \frac{(\bar{y}+q_f)^2}{\bar{y}^2+1}, \tag{4.11}$$

where $\bar{y} = y/\Gamma_f - q_f$, $\Gamma_f \cong \frac{\kappa_1|G_1|^2}{\Omega_1^2+\kappa_1^2}$, and $q_f = -\Omega_1/\kappa_1$. The profile (4.11) has exactly the same form as the classic profile of Fano resonance with maximum at $\bar{y} = 1/q_f$ and zero at $\bar{y} = -q_f$. The asymmetry parameter q_f is related to the frequency offset Ω_1. Keep in mind that this is derived in the vicinity of $y \sim 0$, i.e. $\omega_p \simeq \omega_{c1} - \Omega_1$. In order to see explicitly the nature of the output fields, we use the following set of experimentally realizable parameters $\omega_m = 2\pi \times 10$MHz, $\gamma_m = 2\pi \times 0.01$MHz, $\kappa_1 = 2\pi \times 1$MHz, and $G_1 = 2\pi \times 0.3$MHz. We display the full profile of the output fields in Fig. 4.4(a) as a function of $(\omega_p - \omega_{c1})/\kappa_1$ for a single cavity OMS. It shows the narrow Fano profile as well as the relatively broad resonance near $\omega_p \sim \omega_{c1}$. For detuning $\Delta_1 = \omega_m$ (dotted curve), we obtain the standard EIT profiles [58–60]. As we increase the detuning, the Fano resonance shifts away from the cavity resonance

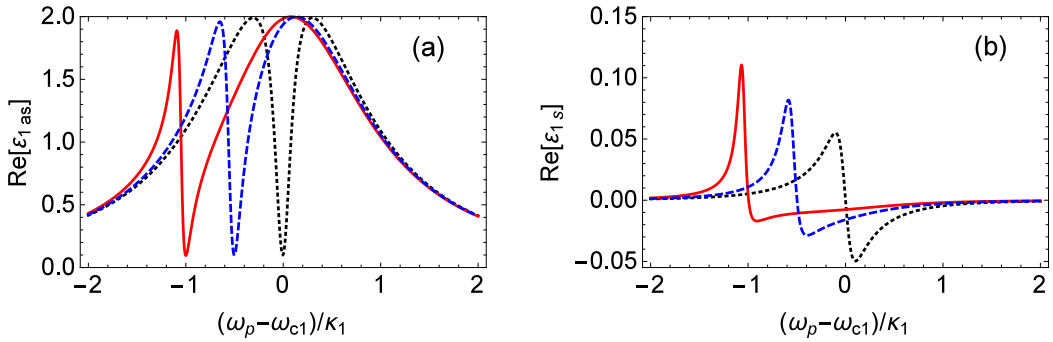

Figure 4.4: The anti-Stokes field $\mathcal{E}_{as}$ (a) and the Stokes field $\mathcal{E}_s$ (b) as a function of frequency of the probe laser input ω_p for the OMS. The black dotted, blue dashed and red solid curves are corresponding to $\Omega_1 = 0$, $\Omega_1 = 0.5\kappa_1$ and $\Omega_1 = \kappa_1$, respectively.

frequency and becomes asymmetric. Each of these Fano lineshapes has a zero point exactly at the frequency $\bar{y} = -q_f$ or equivalently $\omega_p - \omega_{c1} = -\Omega_1$. Our approximation formula (4.11) and the numerical curves obtained directly from (4.5) agree well.

Safavi-Naeini *et al.* [60] have observed such profiles for a broad range of q_f values. What we have demonstrated in this section is how Fano line shapes can arise in OMS under the condition $\gamma_m \ll \kappa_1$. When γ_m starts increasing, the character of the line shape starts changing in a manner similar to changes in the Fano line profiles when the radiative effects are included.

It is also noteworthy to study the Stokes sideband generated by the coupling laser and the mechanical oscillator, although it is suppressed because it is an off-resonantly process. In Fig. 4.4(b), we plot the Stokes sideband. The line shape is asymmetric though a good signature of interference is missing. This is because Fano resonance requires two coherent routes for building up the cavity field, which can interfere with each other, whereas the only route producing Stokes sideband is via the combination of coupling field and the mechanical phonons.

4.3 Double Fano resonances in an optomechanical system

Recently double cavity configurations have attracted a lot of attention because of their wide applicability in photon switching [68], state transfer [82, 83] and transduction of photons [66]. We discuss yet another possibility, making use of double cavities to tune the Fano resonances. In this section, we will show how we can change and control the Fano resonance by adding a second cavity in the OMS. When the coupling fields exist in both cavities, the denominator of Eq. (4.5) becomes cubic and hence the number of roots increases from two to three. This is because we have three coupled systems: two cavity modes and one mechanical mode. At the same time, the numerator in (4.5) becomes a quadratic function of y suggesting the possibility of two different minima in the output fields. Therefore, a single Fano resonance goes over to a double Fano resonance.

Next we examine the quantitative features of the double Fano resonance in OMSs. The parameter space is large and therefore we begin by fixing the detuning in cavity 1 as $\Delta_1 = \omega_m + \kappa_1$ so that its Fano asymmetry parameter $q_f = -1$, and we let the detuning of cavity 2 arbitrary such that $\Delta_2 = \omega_m + \Omega_2$. In the vicinity of $y = \omega_p - \omega_{c1} + \kappa_1 \sim 0$, the roots of the numerator in Eq. (4.5) determine the existence of the Fano minima. We first discuss the case when $|G_2|^2 \gg \Omega_2^2$. Then to first order in dampings, the roots are

$$y_\pm \simeq \pm G_2 + \frac{\Omega_2}{2} - i\frac{\kappa_2 + \gamma_m/2}{2}, \tag{4.12}$$

leading to the splitting of the Fano resonances into two. The power of the coupling field in cavity 2 determines their frequency splitting. In Fig. 4.5(a), we explicitly show the splitting of the Fano resonance in the double-cavity OMS using the same parameters for cavity 1 and $\kappa_2 = 0.05\kappa_1$, $\Omega_2 = 0.1\kappa_1$ for cavity 2 with different coupling strengths. In Fig. 4.5(a), the thin curve shows a single Fano resonance when the coupling field in cavity 2 is absent. As we increase the coupling field in cavity

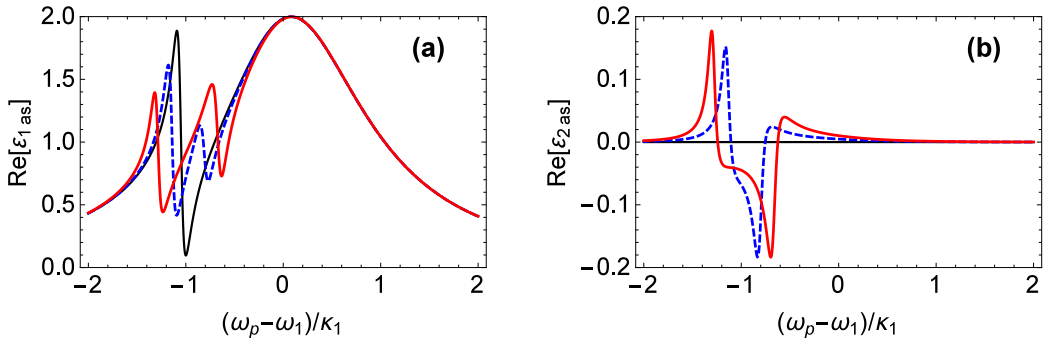

Figure 4.5: The anti-Stokes fields $\mathcal{E}_{as}$ in cavity 1 (a) and in cavity 2 (b) as a function of frequency of the probe laser input in a double-cavity OMS. The thin black, blue dashed and red solid curves are corresponding to different coupling strengths of cavity 2 that $|G_2|/\kappa_1 = 0$, 0.15 and 0.3, respectively. We set $\Omega_2 = 0.1\kappa_1$ and $\kappa_2 = 0.05\kappa_1$.

2, the Fano resonance splits and the splitting increases linearly as we increase the coupling power. Apart from the splitting, their resonance frequency center is shifted by an amount $\Omega_2/2$. The frequency splittings of the two Fano resonances are $0.3\kappa_1$ and $0.6\kappa_1$, which respectively equals to $2|G_2|$. The frequency splitting is independent of the detuning of cavity 2, as long as it is close to ω_m. Therefore, one can always obtain the coupling strength, as well as the coupling power, by measuring the double Fano resonances. In the figure, the minimum values of the double Fano resonances do not go to zero due to the finite values of κ_2 and γ_m. In an OMS with lower κ_2, we should be able to obtain a lower minimum and a higher maximum in the double Fano resonances. This is reminiscent of the result in the context of photoionization in which the value of the minimum depends on the radiative effects.

In Fig. 4.5(b), we plot the anti-Stokes field in cavity 2 in response to the probe laser input in cavity 1. We see asymmetric peaks generated around the frequency of the Fano resonances in $\mathcal{E}_{1as}$ and their widths are similar to the corresponding Fano resonances. Both the peaks heights and peaks splitting increase with the increasing of the coupling power. Physically, this can be interpreted as the probe energy in

cavity 1 is transferred to cavity 2 via the mechanical resonator. The anti-Stokes field in cavity 2 shows anti-symmetric split Fano resonances.

The characteristics of the double Fano resonances are different in the weak coupling limit. When $|G_2|^2 \ll \Omega_2^2$, the roots of the numerator in Eq. (4.5) determining the Fano minima are

$$\begin{aligned} y_+ &\simeq -\frac{|G_2|^2}{\Omega_2} - i\kappa_2\frac{|G_2|^2}{\Omega_2^2} - i\frac{\gamma_m}{2}(1-\frac{|G_2|^2}{\Omega_2^2}) \\ y_- &\simeq \Omega_2 - i\kappa_2(1-\frac{|G_2|^2}{\Omega_2^2}) - i\frac{\gamma_m}{2}\frac{|G_2|^2}{\Omega_2^2}. \end{aligned} \tag{4.13}$$

The root y_+ indicates a frequency shift of the Fano resonance with an amount $-|G_2|^2/\Omega_2$, and the root y_- implies the emergence of a new Fano resonance around $y \sim \Omega_2$ besides the original Fano resonance around $y \sim 0$. In Fig. 4.6, we illustrate both the anti-Stokes and Stokes field in cavity 1 using the following parameters $\kappa_2 = 0.5\gamma_m = 0.005\kappa_1$, $\Omega_2 = -5\gamma_m = -0.05\kappa_1$, and $G_2 = 0.02\kappa_1$, (compared with $G_2 = 0$ for the single cavity case as dashed curves) and parameters for cavity 1 are identical to Fig. 4.5. Using these parameters, the zero point frequency shift of the

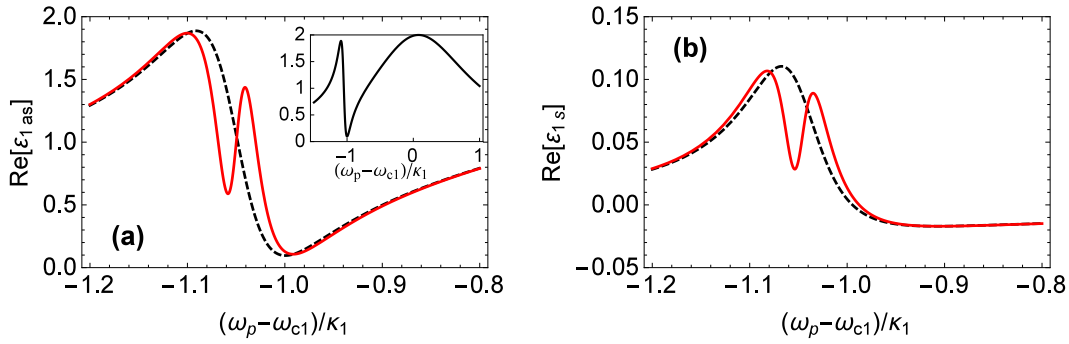

Figure 4.6: The anti-Stokes field (a) and Stokes field (b) in cavity 1 as a function of frequency of the probe laser input in a double-cavity OMS. The solid curves: double-cavity OMS with $G_2 = 0.02\kappa_1$ shows the emergence of a the second Fano resonance, compared to the dashed curve: single cavity OMS. The inset in (a) shows the full profile in a large scale. We set $\Omega_2 = -0.05\kappa_1$ and $\kappa_2 = 0.5\gamma_m = 0.005\kappa_1$.

original Fano resonance is calculated to be $\sim 0.008\kappa_1$ and the width increase to be neg-

ligible. In Fig. 6.7(a), the new Fano resonance emerges around $\omega_p - \omega_{c1} + \Omega_1 \simeq -0.06\kappa_1$ which matches our calculation.

In Fig. 4.6(b), we also plot the Stokes field in cavity 1. It is interesting that a narrow dip is created inside the original single-peak lineshape when cavity 2 is coupled to the OMS. The widths of the broad lineshape and the narrow dip are close to the widths of the original and newly-emerged Fano resonances of the anti-Stokes field in cavity 1, respectively. The dip is caused by cavity 2 adding an extra damping mechanism to the mechanical resonator and destructively interfering with the mechanical damping, so that it prevents the mechanical mode from aiding the generation of the Stokes field in cavity 1.

4.4 Fano resonances in quantum fluctuations of fields

In the previous sections, we studied the OMS when the optical cavity is fed by both a detuned coupling field and a weak probe field, and found its output exhibits Fano resonance. Now we will study the quantum fluctuation of the cavity field without any input probe field, as illustrated in Fig. 4.7. The quantum fluctuation of the

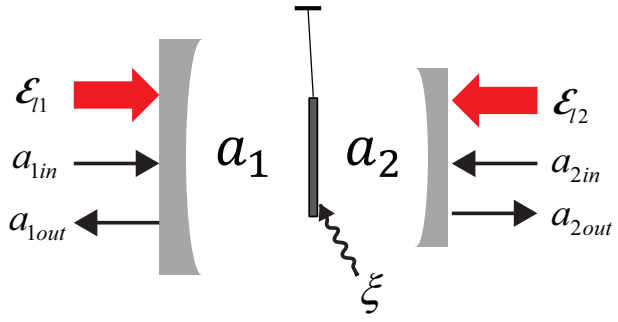

Figure 4.7: Schematic double-cavity OMS. Here $\mathcal{E}_{ci}$'s are coherent fields and $a_{i\text{in}}$'s are the quantum vacuum fields. ξ is the Brownian noise.

cavity fields arises (i) directly from the fluctuation of the vacuum input and (ii) from the process of photon creation via an oscillating mirror subjected to thermal noise.

Those two mechanisms can interfere destructively creating a zero amplitude in the fluctuations of the cavity field.

In a double-cavity OMS, the quantum Langevin equations governing the operators Q, P, a_i and $a_i^\dagger$ are given by

$$\begin{aligned}
\dot{Q} &= \omega_m P, \\
\dot{P} &= \sqrt{2}(g_1 a_1^\dagger a_1 - \sqrt{2} g_2 a_2^\dagger a_2) - \omega_m Q - \gamma_m P + \xi, \\
\dot{a}_1 &= -i(\omega_1 - \omega_{c1} - \sqrt{2} g_1 Q) a_1 - \kappa_1 a_1 + \mathcal{E}_{c1} + \sqrt{2\kappa_1} a_{1\text{in}}, \\
\dot{a}_2 &= -i(\omega_2 - \omega_{c2} + \sqrt{2} g_2 Q) a_2 - \kappa_2 a_2 + \mathcal{E}_{c2} + \sqrt{2\kappa_2} a_{2\text{in}}.
\end{aligned} \tag{4.14}$$

where $a_{i\text{in}}$ and $a_{i\text{in}}^\dagger$ are the input noise from cavity i and ξ stems form the thermal noise of the mechanical resonator at finite temperature. Their correlation functions in frequency domain are given in Eq. (1.8) and they can be written in the frequency domain as

$$\langle a_{i\text{in}}(\omega) a_{i\text{in}}^\dagger(\omega') \rangle = 2\pi\delta(\omega - \omega') \langle \xi(\omega)\xi(\omega') \rangle = 2\pi \frac{\gamma_m}{\omega_m} \omega \left[1 + \coth\left(\frac{\hbar\omega}{2k_B T} \right) \right] \delta(\omega + \omega'), \tag{4.15}$$

where k_B is the Boltzmann constant and T is the temperature of the environment of the mirror.

Equations. (4.14) are difficult to solve because they are nonlinear. However, considering that the quantum fluctuation values around their steady states are relatively small, we can adopt the standard linearization method by separating the fluctuations from their mean values,

$$Q = Q_0 + \delta Q, \quad P = P_0 + \delta P, \quad a_i = a_{i0} + \delta a_i, \tag{4.16}$$

for $i = 1, 2$. When expanding the products of two operators A and B, we can make the approximation $\delta(AB) \approx A_0 \delta B + B_0 \delta A$ so that quantum Langevin equations are

modified as

$$\begin{aligned}
\delta\dot{Q} &= \omega_m \delta P, \\
\delta\dot{P} &= \sqrt{2} g_1 (a_{10}^* \delta a_1 + a_{10} \delta a_1^\dagger) - g_2 (a_{20}^* \delta a_2 + a_{20} \delta a_2^\dagger) - \omega_m \delta Q - \gamma_m \delta P + \xi, \\
\delta\dot{a}_1 &= -(\kappa_1 + i\Delta_1)\delta a_1 + i\sqrt{2} g_1 a_{10} \delta Q + \sqrt{2\kappa_1} a_{1\mathrm{in}}, \\
\delta\dot{a}_2 &= -(\kappa_2 + i\Delta_2)\delta a_1 - i\sqrt{2} g_2 a_{20} \delta Q + \sqrt{2\kappa_2} a_{2\mathrm{in}},
\end{aligned} \tag{4.17}$$

The coupling fields are absorbed in the steady state mean values, so they do not show explicitly in Eq. (4.17). a_{i0}'s and Δ_i are defined identically to Sec. 4.1. In order to get the spectra of the fluctuations in the quantities δQ, δP, δa_i and $\delta a_i^\dagger$, we Fourier transform them into the frequency domain using $f(t) = \frac{1}{2\pi}\int_{-\infty}^{+\infty} f(\omega) \mathrm{e}^{-i\omega t} \mathrm{d}\omega$. By solving them, we obtain the fields in cavity 1 containing the signature of the quantum fluctuations

The fields in cavity 1 containing the signature of the quantum fluctuations can be calculated as

$$\begin{aligned}
\sqrt{2\kappa_1}\delta a_1(\omega) = {} & E_1(\omega) a_{1\mathrm{in}}(\omega) + F_1(\omega) a_{1\mathrm{in}}^\dagger(-\omega) \\
& + E_2(\omega) a_{2\mathrm{in}}(\omega) + F_2(\omega) a_{2\mathrm{in}}^\dagger(-\omega) + V(\omega)\xi(\omega),
\end{aligned} \tag{4.18}$$

and fluctuations $\delta a_2(\omega)$ in cavity 2 can be calculated similarly using the symmetry property of the double-cavity configuration. Note that the term $E_1(\omega)$ physically means that a noise photon at $\omega + \omega_{c1}$ produces a photon at frequency $\omega + \omega_{c1}$ where as the term $F_1(\omega)$ corresponds to the four wave mixing process where a photon of frequency $\omega_{c1} - \omega$ produces a photon of frequency $\omega_{c1} + \omega$. Similar interpretations apply to $E_2(\omega)$ and $F_2(\omega)$. Thus $E_1(\omega)$ and $F_1(-\omega)$ would have direct relation to the anti-Stokes and Stokes fields discussed in the earlier sections. The mechanical noise can be suppressed by cooling down the environment temperature, though it is the dominant contribution to the fluctuations at high temperatures, and hence we omit

the $\xi(\omega)$ term. Here $E_i(\omega)$'s, and $F_i(\omega)$'s are the functions given by

$$\begin{aligned}
E_1(\omega) &= \frac{2\kappa_1}{D(\omega)}\frac{-2i|G_1|^2}{(\kappa_1+i\Delta_1-i\omega)^2}+\frac{2\kappa_1}{\kappa_1+i\Delta_1-i\omega},\\
F_1(\omega) &= \frac{2\kappa_1}{D(\omega)}\frac{2i|G_1|^2}{(\kappa_1-i\omega)^2+\Delta_1^2},\\
E_2(\omega) &= \frac{\sqrt{2\kappa_1 2\kappa_2}}{D(\omega)}\frac{2iG_1^*G_2}{(\kappa_1+i\Delta_1-i\omega)(\kappa_2+i\Delta_2-i\omega)},\\
F_2(\omega) &= \frac{\sqrt{2\kappa_1 2\kappa_2}}{D(\omega)}\frac{2iG_1G_2^*}{(\kappa_1-i\Delta_1+i\omega)(\kappa_2-i\Delta_2-i\omega)},\\
D(\omega) &= \sum_{i=1,2}\frac{2\Delta_i|G_i|^2}{(\kappa_i-i\omega)^2+\Delta_i^2}-\frac{\omega_m^2-\omega^2-i\omega\gamma_m}{\omega_m}.
\end{aligned} \tag{4.19}$$

The quadratures of the field in cavity 1, which can be measured using homodyne detection, have the spectra defined as $\langle X_1(\Omega)X_1(\omega)\rangle = 2\pi S_{1X}\delta(\omega+\Omega)$ and $\langle Y_1(\Omega)Y_1(\omega)\rangle = 2\pi S_{1Y}\delta(\omega+\Omega)$ with $X_1=(\delta a_1^\dagger+\delta a_1)/\sqrt{2}$ and $Y_1=i(\delta a_1^\dagger-\delta a_1)/\sqrt{2}$. Now we calculate the fluctuation spectrum in the X quadrature as

$$\begin{aligned}
2\kappa_1 S_{1X}(\omega) &= \frac{1}{2}|E_1^*(-\omega)+F_1(\omega)|^2+\frac{1}{2}|E_2^*(-\omega)+F_2(\omega)|^2\\
&= \frac{1}{2}\left|\frac{2\kappa_1}{\kappa_1+i\Delta_1+i\omega}\right|^2\left|1-\frac{1}{D(\omega)}\frac{4\Delta_1 G_1^2}{(\kappa_1+i\omega)^2+\Delta_1^2}\right|^2\\
&\quad+\frac{1}{2}\left|\frac{\sqrt{2\kappa_1 2\kappa_2}}{\kappa_2+i\Delta_2+i\omega}\right|^2\left|\frac{1}{D(\omega)}\frac{4\Delta_1 G_1 G_2}{(\kappa_1+i\omega)^2+\Delta_1^2}\right|^2.
\end{aligned} \tag{4.20}$$

We first study single-cavity OMS when $G_2=0$. The cavity field fluctuation in X quadrature is given as

$$2\kappa_1 S_{1X}(\omega)\approx\frac{\kappa_1^2}{2\omega_m^2}\frac{(\omega-\omega_m)^2}{(\omega-\omega_m-\frac{\Omega_1 G_1^2}{\Omega_1^2+\kappa_1^2})^2+(\frac{\kappa_1 G_1^2}{\Omega_1^2+\kappa_1^2})^2}. \tag{4.21}$$

We do not show the expressions of fluctuations $S_{1Y}(\omega)$ or $S_{1a}(\omega)$ since they do not exhibit a Fano minimum. Equation (4.21) indicates a Fano lineshape, which has a minimum at $\omega=\omega_m$ and a maximum at $\omega=\omega_m+\frac{\Omega_1 G_1^2}{\Omega_1^2+\kappa_1^2}$ with width $\Gamma_f=\frac{\kappa_1 G_1^2}{\Omega_1^2+\kappa_1^2}$ and asymmetry parameter $q_f=-\Omega_1/\kappa_1$. To see the Fano resonance, it is important to have $\kappa_1\gg\gamma_m$ and $G_i^2\gg\kappa_i\gamma_m$. The spectra $S_{1\mathrm{Xout}}(\omega)$ and $S_{1\mathrm{Yout}}(\omega)$ of the output field are different from the cavity fields by an amount of $a_{1\mathrm{in}}$ using the input-output relation $a_{1\mathrm{out}}=\sqrt{2\kappa_1}\delta a_1-a_{1\mathrm{in}}$.

We illustrate the spectra of the quadrature $S_{1\mathrm{X}}(\omega)$, $S_{1\mathrm{Y}}(\omega)$, $S_{1\mathrm{Xout}}(\omega)$, and $S_{1\mathrm{Yout}}(\omega)$ for both single-cavity OMS (solid curves) and double-cavity OMS (dashed curves) in Fig. 4.8 using parameters as in Fig. 4.5. From the solid curves in the figure, we see

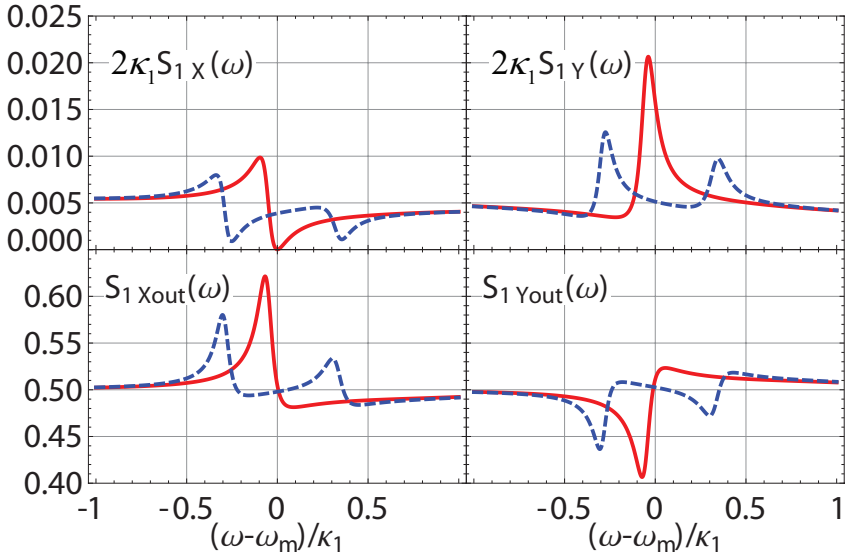

Figure 4.8: The spectra of the quadratures for the cavity fields and output fields for both single-cavity OMS (solid curves) and double-cavity OMS (dashed curves). The parameters used are the same to Fig. 4.5.

that the $S_{1\mathrm{X}}(\omega)$ quadrature exhibits a clear Fano resonance. The Fano resonance has a zero point at frequency $\omega - \omega_m = 0$ and has width $\Gamma_f = 0.1\kappa_1$, both of which match our calculation. The spectrum of the quadratures $S_{1\mathrm{Xout}}(\omega)$ and $S_{1\mathrm{Yout}}(\omega)$ of the output field also have typically asymmetric line shapes which are signatures of interferences. These spectra have similarities to the spectra for the Stokes field (Fig. 4.5b). Note that a formula like Eq. (4.21) shows that the quadrature spectra are determined by the interference of the Stokes and anti-Stokes terms. The reason is that in the region of interest in the spectrum $S_{1\mathrm{X}}(\omega)$, the term $E_1^*(-\omega)$ is approximately flat. When the second cavity is coupled to the system, we expect a splitting of the Fano lineshape in the spectrum of fluctuations following the classical analysis of Sec. 4.3. The splittings of the resonances separated by $0.6\kappa_1 = 2G_2$ appear in the dashed

curves in Fig. 4.8. The splittings are due to the enhance coupling strength by the increasing photon number in the cavities, which induced normal mode splitting of the cavity states.

4.5 Summary

To summarize the results, we have shown how the asymmetric Fano line shapes can arise in optomechanics. We identify interfering pathways leading to the Fano resonances. In contrast to atomic systems, the coupling field can be used to tune Fano resonances using both the frequency and the power of coupling field. In fact, as displayed in Fig. 1.1b the coupling field opens up another coherent path way. We give explicit expressions for the width and the asymmetry parameter. The Fano resonances can be studied both via pump probe experiments and via the study of the quantum fluctuations in the output fields. The Fano minima are much more pronounced in the results of pump probe experiments.

CHAPTER 5

GENERATION OF TWO-MODE SQUEEZED LIGHT

In the previous chapters, we have seen how coherent interaction between cavity photons and mechanical phonons plays an important role in various phenomena in cavity optomechanical systems. Using the coupled-oscillator models we are able to design several optomechanics applications [52, 53, 55, 58] based on the coherence of different fields. Those proposals have all been experimentally demonstrated directly [43, 54, 84, 91] or indirectly thanks to the evolutionary development of optomechanics techniques and the versatility of our proposal.

The field of cavity optomechanics has evolved very rapidly over the past years and is on the verge of becoming the field of cavity quantum-optomechanics [39, 97–100]. In this chapter, we go beyond the semiclassical description and adopt the quantum theory of driven optomechanics by taking account of the quantum fluctuations of vacuum noise and Brownian noise. As we mentioned in the previous chapter, OMS can be treated as an effective Kerr medium, *i.e.* providing nonlinear interaction of photon, subject to dissipation which is non-negligible and even tunable. It is natural to consider the role of OMS in generating or engineering quantum states of light or oscillators. One of the simplest non-trivial quantum states is a squeezed state [101–103]—for a harmonic oscillator, the displacement or momentum uncertainty is below the ground state uncertainty, *i.e.* the so called Heisenberg bound; and for the light field, the fluctuation of its amplitude or phase or a quadrature is below the vacuum field fluctuation. Squeezed field of light is widely used in the context of quantum optics enabling one to perform interferometric measurements with precisions beyond the

standard quantum limit. Recently, the use of squeezed states has also been recognized as an essential resource for quantum information processing (QIP) [104, 105] in the continuous variable (CV) regime [106] to realize quantum communication [107, 108], unconditional quantum teleportation [109] and one-way quantum computing [110, 111].

In this chapter, we use a double-cavity optomechanical system and develop a quantum optical analog of the method of producing two mode squeezing which is based on the usage of an entangled pair of photons. We effectively mimic the behaviour of a downconverter for producing squeezing in an optomechanical system. In a downconverter [36, 48, 112], the coupling Hamiltonian, which leads to two mode squeezing, is given by $\xi a_1 a_2 + \xi^* a_1^\dagger a_2^\dagger$, where the a_i's are the annihilation operators for two light fields. The entangled photon pairs a_i's are spontaneously produced from the pump. An appropriate linear combination of a_i's produces quadrature squeezing. Any system, whose effective interaction can be reduced to this form, becomes a good candidate for two mode squeezing. Thus the goal is to find systems where different interactions can be reduced to the form $\xi a_1 a_2 + \xi^* a_1^\dagger a_2^\dagger$. The third order nonlinearities in optical fibers can also give rise to such an interaction leading to squeezing. We now describe how such an effective Hamiltonian can be realized in cavity optomechanics. A cavity driven by a blue detuned pump can spontaneously produce a photon and a phonon. Under the usual approximations—undepleted pump and rotating wave approximation—this process would be described by the effective Hamiltonian $\xi a_1 b + \xi^* a_1^\dagger b^\dagger$ where a_1 stands for the cavity photon and b stands for the phonon. Though this Hamiltonian has the form of a downconverter, it cannot be used to produce squeezing since the phonon frequency is many orders less than the optical frequency.[1] Then one would like to replace the phonon mode by another

[1]For observation of two mode squeezing, one needs to superpose externally two modes and this can be done only if the modes are close in frequency. Within the blue cavity the two modes phonon

optical mode. This will be achieved by using another parametric process where a red detuned pump photon combines with a coherent phonon and produces a cavity photon via an up-conversion process. In the undepleted pump and rotating wave approximations, this is described by $\zeta a_2^\dagger b + \zeta^* a_2 b^\dagger$. Effectively, a cavity driven by a red detuned pump swaps the cavity photon and phonon. In what follows, we use both these mechanisms to produce a pair of photons in a double-cavity optomechanical system. Thus we produce a photon pair by using phonons. It should be kept in mind that although we produce a photon pair, the mediating mechanism is an active mechanism which puts a limit on the amount of achievable squeezing. This is in contrast to the situation with a downconverter where the crystal participates in a passive manner in the sense that it does not contribute to quantum noise. We show generation of very large two mode squeezing even at an effective mechanical mode temperature like 10mK (phonon occupancy $\bar{n}_{\rm th} = 3.7$) which can be obtained either by precooling or by using cooling techniques such as side band cooling. The large squeezing is a consequence of active phonon nonlinearities which become large due to the resonant nature of the underlying processes.

5.1 Theoretical model

As mentioned, we need an optomechanical system with two optical modes interacting with a common mechanical mode. Several possible experimental realizations have been discussed in Sec. 3.1 including *e.g.* the "membrane-in-the-middle setup" [Fig. 5.1(a)], silica microresonator with two preselected optical modes [Fig. 5.1(b)], and two coupled waveguides enbedded in an optomechanical crystal. In what follows we continue to use the notation of double-cavity systems, though the discussion would apply to several other two mode systems. We adopt the same double-cavity OMS

and photon are resonant but it is hard to probe the properties of the linear combination of the phonon-photon mode.

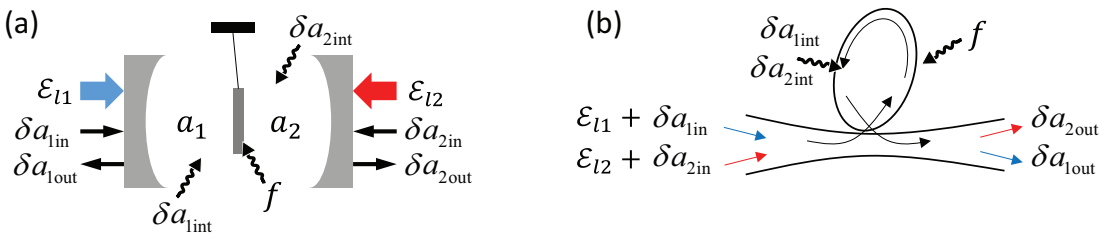

Figure 5.1: (a) Schematic of the proposed double-cavity optomechanics where cavity 1 (2) fed by blue (red) detuned driving lasers and the vacuum inputs are coupled to the same mechanical resonator mediated in thermal bath. $\mathcal{E}_{li}$, a_i, $\delta a_{i\text{in}}$, $\delta a_{i\text{int}}$ and $\delta a_{i\text{out}}$ denote the classical driving field, in-cavity optical field, input quantum vacuum noise, internal quantum vacuum noise and output quantum fluctuation for cavity i, respectively, and f denotes the mechanical noise. (b) An alternative realization in a silica microresonator: Two preselected optical modes interacting with a mechanical mode and the driving lasers frequencies are chosen as in (a).

described in Sec. 3.2. However, the driving laser is blue detuned in cavity 1 and red detuned in cavity 2, as illustrated in Fig. 5.1. The Hamiltonian is written as

$$H = \sum_{i=1,2} [\hbar\omega_{ci} a_i^\dagger a_i + i\hbar\mathcal{E}_{li}(a_i^\dagger e^{-i\omega_{li}t} - a_i e^{i\omega_{li}t})] + \frac{1}{2}\hbar\omega_m(Q^2+P^2) - \hbar\sqrt{2}(g_1 a_1^\dagger a_1 - g_2 a_2^\dagger a_2)Q. \tag{5.1}$$

The driving laser amplitude is related to its power $\mathcal{P}_{li}$ by $\mathcal{E}_{li} = \sqrt{2\kappa_i \frac{\mathcal{P}_{li}}{\hbar\omega_{li}}}$ and $2\kappa_i$ is the decay rate of the cavity i. The second term in (5.1) represents how the external coherent fields enter the cavity (Chaps. 7 and 9 in [48]). It is convenient to rewrite the Hamiltonian into a new picture using transformation $\exp[-i\sum(\omega_{li} a_i^\dagger a_i t)]$, then

$$H = \sum_{i=1,2} [\hbar(\omega_{ci} - \omega_{li}) b_i^\dagger b_i + i\hbar\mathcal{E}_{li}(b_i^\dagger - b_i)] + \frac{1}{2}\hbar\omega_m(Q^2+P^2) - \hbar\sqrt{2}(g_1 b_1^\dagger b_1 - g_2 b_2^\dagger b_2)Q, \tag{5.2}$$

with b_i's defined by $a_i = b_i e^{-i\omega_{li}t}$. We consider the cavity to be subject to both internal loss and external loss, we write the decay rate of the cavity i as $\kappa_i = \kappa_{ei} + \kappa_{ii}$,

where κ_{ei} and κ_{ii} denotes the external and internal decay rate of cavity i, respectively. Then the quantum Langevin equations governing the system become,

$$\begin{aligned}
\dot{Q} &= \omega_m P, \\
\dot{P} &= \sqrt{2}g(b_1^\dagger b_1 - b_2^\dagger b_2) - \omega_m Q - \gamma_m P + \xi, \\
\dot{b_1} &= -i(\omega_{c1} - \omega_{l1} - \sqrt{2}g_1 Q)b_1 - \kappa_1 b_1 + \mathcal{E}_{l1} + \sqrt{2\kappa_{e1}}b_{1\text{in}} + \sqrt{2\kappa_{i1}}b_{1\text{int}}, \\
\dot{b_2} &= -i(\omega_{c2} - \omega_{l2} + \sqrt{2}g_2 Q)b_2 - \kappa_2 b_2 + \mathcal{E}_{l2} + \sqrt{2\kappa_{e2}}b_{2\text{in}} + \sqrt{2\kappa_{i2}}b_{2\text{int}},
\end{aligned} \tag{5.3}$$

where $b_{i\text{in}}$ and $b_{i\text{int}}$ for $i = 1, 2$ is the input and internal vacuum noise with correlation fluctuations

$$\langle b_{i\text{int}}(t) b_{j\text{int}}^\dagger(t')\rangle = \delta_{ij}\delta(t-t'), \qquad \langle b_{i\text{int}}(t) b_{j\text{int}}^\dagger(t')\rangle = \delta_{ij}\delta(t-t'). \tag{5.4}$$

By taking the same Fourier transformation, the correlation fluctuations in the frequency domain can be expressed as

$$\langle \tilde{b}_{i\text{int}}(\omega)\tilde{b}_{j\text{int}}^\dagger(-\omega')\rangle = 2\pi\delta_{ij}\delta(\omega+\omega'), \qquad \langle \tilde{b}_{i\text{int}}(\omega)\tilde{b}_{j\text{int}}^\dagger(-\omega')\rangle = 2\pi\delta_{ij}\delta(\omega+\omega'). \tag{5.5}$$

The input-output relation is related only to the external decay rate

$$\tilde{b}_{i\text{out}} = \sqrt{2\kappa_{ei}}\tilde{b}_i - \tilde{b}_{i\text{in}}. \tag{5.6}$$

The noise term ξ stems from the thermal noise of the mechanical resonator at a finite temperature T, which obeys

$$\langle \xi(t)\xi(t')\rangle = \frac{\gamma_m}{2\pi\omega_m}\int \omega \mathrm{e}^{-i\omega(t-t')}\left[1 + \coth\left(\frac{\hbar\omega}{2K_B T}\right)\right]\mathrm{d}\omega,$$

where K_B is the Boltzmann constant. We follow the standard procedure and solve (5.3) perturbatively by separating the classical mean value and the fluctuation of each operator,

$$Q = Q_s + \delta Q, \qquad P = P_s + \delta P, \qquad b_i = b_{is} + \delta b_i, \tag{5.7}$$

for $i = 1, 2$. In this way, we can solve for the classical mean values of the optical fields as $b_{is} = \frac{\mathcal{E}_{li}}{\kappa_i + i\Delta_i}$ and $Q_s = \sqrt{2}(|b_{1s}|^2 g_1 - |b_{2s}|^2 g_2)/\omega_m$ where $\Delta_i = \omega_{ci} - \omega_{li} \mp \sqrt{2}g_i Q_s$

are the mean detuning of the cavities and $-$ is for $i = 1$ and $+$ for $i = 2$. Then the linearized quantum Langevin equations are given by

$$\begin{aligned}
\delta\dot{Q} &= \omega_m \delta P, \\
\delta\dot{P} &= \sqrt{2}g_1(b_{1s}^*\delta b_1 + b_{1s}\delta b_1^\dagger) - \sqrt{2}g_2(b_{2s}^*\delta b_2 + b_{2s}\delta b_2^\dagger) - \omega_m\delta Q - \gamma_m\delta P + \xi, \\
\delta\dot{b}_1 &= -(\kappa_1 + i\Delta_1)\delta b_1 + i\sqrt{2}g_1 b_{1s}\delta Q + \sqrt{2\kappa_{e1}}b_{1\text{in}} + \sqrt{2\kappa_{i1}}b_{1\text{int}}, \\
\delta\dot{b}_2 &= -(\kappa_2 + i\Delta_2)\delta b_1 - i\sqrt{2}g_2 b_{2s}\delta Q + \sqrt{2\kappa_{e2}}b_{2\text{in}} + \sqrt{2\kappa_{i2}}b_{2\text{int}}.
\end{aligned} \tag{5.8}$$

It is convenient to work with new optical and mechanical annihilation operators defined as

$$\begin{aligned}
\tilde{b}_1 &= \delta b_1 \mathrm{e}^{-i\omega_m t}, \qquad & c\mathrm{e}^{-i\omega_m t} &= (\delta Q + \delta P)/\sqrt{2}, \\
\tilde{b}_2 &= \delta b_2 \mathrm{e}^{i\omega_m t}, \qquad & c^\dagger\mathrm{e}^{i\omega_m t} &= (\delta Q - \delta P)/(\sqrt{2}i),
\end{aligned} \tag{5.9}$$

and the input field fluctuations defined as $\tilde{b}_{i\text{in}} = \delta b_{i\text{in}}\mathrm{e}^{\mp i\omega_m t}$, with $\mp$ for $i = 1, 2$. These operators obey the equations

$$\begin{aligned}
\dot{c} &= -\frac{\gamma_m}{2}(c - c^\dagger\mathrm{e}^{2i\omega_m t}) + f(t) + ig_1(b_{1s}^*\tilde{b}_1\mathrm{e}^{2i\omega_m t} + b_{1s}\tilde{b}_1^\dagger) - ig_2(b_{2s}^*\tilde{b}_2 + b_{2s}\tilde{b}_2^\dagger\mathrm{e}^{2i\omega_m t}), \\
\dot{\tilde{b}}_1 &= -(\kappa_1 + i\Delta_1 + i\omega_m)b_1 + \sqrt{2\kappa_{e1}}b_{1\text{in}} + \sqrt{2\kappa_{i1}}b_{1\text{int}} + ig_1 b_{1s}(c\mathrm{e}^{-2i\omega_m t} + c^\dagger), \\
\dot{\tilde{b}}_2 &= -(\kappa_2 + i\Delta_2 - i\omega_m)b_2 + \sqrt{2\kappa_{e2}}b_{2\text{in}} + \sqrt{2\kappa_{i2}}b_{2\text{int}} - ig_2 b_{2s}(c + c^\dagger\mathrm{e}^{2i\omega_m t}).
\end{aligned} \tag{5.10}$$

The rapidly rotating terms in (5.10) correspond to nonresonant FWM processes. For example for cavity 2 (equation for $\tilde{b}_2$), a red pump photon $\omega_c - \omega_m$ can produce a photon of frequency $\omega_c - 2\omega_m$ and another photon of frequency ω_c by absorbing or releasing a phonon ω_m. The anti-Stokes generation at the cavity resonance frequency ω_c is a resonant process, whereas the Stokes generation at $\omega_c - 2\omega_m$ is highly nonresonant with the cavity resonance, since $\omega_m \gg \kappa_i$ in the resolved side-band regime. Similar arguments apply to cavity 1 (equation for $\tilde{b}_1$). We drop all the nonresonant

processes, i.e. the rapidly rotating terms at frequencies $2\omega_m$, and obtain

$$\begin{aligned}
\dot{c} &= -\frac{\gamma_m}{2}c + iG_1\tilde{b}_1^\dagger - iG_2^*\tilde{b}_2 + f(t),\\
\dot{\tilde{b}}_1^\dagger &= -(\kappa_1 - i\delta_1)\tilde{b}_1^\dagger - iG_1^* c + \sqrt{2\kappa_{e1}}b_{1\text{in}} + \sqrt{2\kappa_{i1}}b_{1\text{int}},\\
\dot{\tilde{b}}_2 &= -(\kappa_2 + i\delta_2)\tilde{b}_2 - iG_2 c + \sqrt{2\kappa_{e2}}b_{2\text{in}} + \sqrt{2\kappa_{i2}}b_{2\text{int}},
\end{aligned} \tag{5.11}$$

where $\delta_1 = \Delta_1 + \omega_m$, $\delta_2 = \Delta_2 - \omega_m$ and $G_i = b_{is}g_i$ for $i = 1, 2$. Notice that G_i is a pure imaginary number by the definition of b_{is} under the resolved side-band regime, $\Delta \gg \kappa_i$. Since the coupling laser in cavity 1(2) is blue(red) detuned by an amount ω_m, $\delta_1 \sim \delta_2 \sim 0$, *i.e.* $-\Delta \sim \Delta_2 \sim \omega_m$. The correlation relation of $f(t)$ was given in (1.14). In order to solve these equations, we transform them into the frequency domain using $A(t) = \frac{1}{2\pi}\int_{-\infty}^{+\infty} A(\omega)\mathrm{e}^{-i\omega t}\mathrm{d}\omega$, and $A^\dagger(t) = \frac{1}{2\pi}\int_{-\infty}^{+\infty} A^\dagger(-\omega)\mathrm{e}^{-i\omega t}\mathrm{d}\omega$, so that $A^\dagger(-\omega) = [A(-\omega)]^\dagger$. Then the correlation relation is

$$\begin{aligned}
\langle\tilde{b}_{i\text{in}}(\omega)\tilde{b}_{j\text{in}}^\dagger(-\omega')\rangle &= 2\pi\delta_{ij}\delta(\omega+\omega'),\\
\langle\tilde{b}_{i\text{int}}(\omega)\tilde{b}_{j\text{int}}^\dagger(-\omega')\rangle &= 2\pi\delta_{ij}\delta(\omega+\omega'),\\
\langle f^\dagger(-\omega)f(\omega')\rangle &= 2\pi\gamma_m\bar{n}_{\text{th}}\delta(\omega+\omega'),\\
\langle f(\omega)f^\dagger(-\omega')\rangle &= 2\pi\gamma_m(\bar{n}_{\text{th}}+1)\delta(\omega+\omega').
\end{aligned} \tag{5.12}$$

The input-output relation is related only to the external decay rate

$$\tilde{b}_{i\text{out}} = \sqrt{2\kappa_{ei}}\tilde{b}_i - \tilde{b}_{i\text{in}}, \tag{5.13}$$

using which we can obtain the output optical fields following a similar procedure as in the main text,

$$\begin{aligned}
\tilde{b}_{1\text{out}}(\omega) = -\tilde{b}_{1\text{in}}(\omega) + \sqrt{2\kappa_{e1}}\Big[&\sqrt{2\kappa_{e1}}E_{s1}(\omega)\tilde{b}_{1\text{in}}(\omega) + \sqrt{2\kappa_{e2}}F_{s1}(\omega)\tilde{b}_{2\text{in}}^\dagger(-\omega)\\
&+ \sqrt{2\kappa_{i1}}E_{s1}(\omega)\tilde{b}_{1\text{int}}(\omega) + \sqrt{2\kappa_{i2}}F_{s1}(\omega)\tilde{b}_{2\text{int}}^\dagger(-\omega) + V_{s1}(\omega)f^\dagger(-\omega)\Big],
\end{aligned} \tag{5.14}$$

$$\begin{aligned}
\tilde{b}_{2\text{out}}(\omega) = -\tilde{b}_{2\text{in}}(\omega) + \sqrt{2\kappa_{e2}}\Big[&\sqrt{2\kappa_{e2}}E_{s2}(\omega)\tilde{b}_{2\text{in}}(\omega) + \sqrt{2\kappa_{e1}}F_{s2}(\omega)\tilde{b}_{1\text{in}}^\dagger(-\omega)\\
&+ \sqrt{2\kappa_{i2}}E_{s2}(\omega)\tilde{b}_{2\text{int}}(\omega) + \sqrt{2\kappa_{i1}}F_{s2}(\omega)\tilde{b}_{1\text{int}}^\dagger(-\omega) + V_{s2}(\omega)f(\omega)\Big],
\end{aligned} \tag{5.15}$$

where

$$
\begin{aligned}
E_{s1}(\omega) &= \frac{1}{D^*(-\omega)}\frac{|G_1|^2}{(\kappa_1+ix_1+i\omega)^2}+\frac{1}{\kappa_1+ix_1+i\omega},\\
F_{s1}(\omega) &= -\frac{G_1^*G_2^*}{D^*(-\omega)(\kappa_1+ix_1+i\omega)(\kappa_2+ix_2-i\omega)},\\
E_{s2}(\omega) &= -\frac{1}{D(\omega)}\frac{|G_2|^2}{(\kappa_2+ix_2-i\omega)^2}+\frac{1}{\kappa_2+ix_2-i\omega},\\
F_{s2}(\omega) &= \frac{G_1G_2}{D(\omega)(\kappa_1-ix_1+i\omega)(\kappa_2+ix_2-i\omega)},\\
V_{s1}(\omega) &= -\frac{iG_1}{D^*(-\omega)(\kappa_1+ix_1+i\omega)},\\
V_{s2}(\omega) &= -\frac{iG_2}{D(\omega)(\kappa_2+ix_2-i\omega)},\\
D(\omega) &= -\frac{|G_1|^2}{\kappa_1-ix_1+i\omega}+\frac{|G_2|^2}{\kappa_2+ix_2-i\omega}+(\frac{\gamma_m}{2}-i\omega).
\end{aligned}
\tag{5.16}
$$

We now give the meaning of the coefficients E, F and V in (5.14)-(5.15). These coefficients are obtained to all orders in the strengths of the blue and red pumps. The E's and F's to second order in G can be given simple physical interpretations. Let us first consider an incoming vacuum photon from cavity 1. It should be borne in mind that the frequency ω from the cavities corresponds to $\omega_c+\omega$ according to the relation $\delta a_{i\text{out}} = \tilde{b}_{i\text{out}}\mathrm{e}^{-i\omega_c t}$. This produces a vacuum photon of frequency $\omega_c+\omega$ in cavity 1 and a photon of frequency $\omega_c-\omega$ in cavity 2. The reason for the production of a photon of frequency $\omega_c-\omega$ can be understood as follows: A blue detuned photon of frequency $\omega_c+\omega_m$ produces a phonon of frequency $\omega_m-\omega$ and a photon of frequency $\omega_c+\omega$. The phonon of frequency $\omega_m-\omega$ interacts with the red detuned pump of frequency $\omega_c-\omega_m$. This is shown in the diagram in Fig 5.2. The term $F_2(-\omega)$ in (5.14) represents the combined effect of these two processes. We can similarly understand $F_1(-\omega)$ in (5.14) by considering an incoming vacuum photon from cavity 2. Note that these are the diagrams contributing to the lowest order in G_1G_2 in the expression for $F_2(-\omega)$. The term proportional to $|G_1|^2$ in $E_1(\omega)$ arises from the diagram Fig. 5.2(a). The V_i terms in (5.14) and (5.15) correspond to the quantum noise which is added by either the thermal phonons or vacuum phonons. Note that in

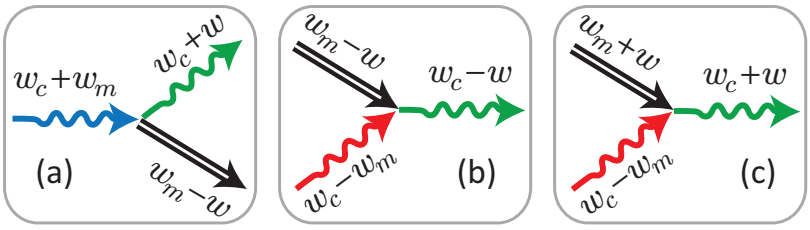

Figure 5.2: The photon-phonon interaction processes in cavity 1 **(a)** and in cavity 2 **(b)** and **(c)** . The curly arrows represent photons and double-line arrows represent phonons. In contrast to the processes in **(a)** and **(b)**, the process in **(c)** involves incoherent phonons.

lowest order in G_i's, we can interpret the last term in (5.15) by saying that a thermal phonon of frequency $\omega_m + \omega$ combines with a red photon of frequency $\omega_c - \omega_m$ to produce a photon of frequency $\omega_c+\omega$ as shown in the Fig. 5.2(c). Similarly in (5.15) a thermal phonon or a vacuum phonon of frequency $\omega_m - \omega$ and a photon of frequency $\omega_c + \omega$ combine to create a blue photon $\omega_c + \omega_m$. This is the reverse of the process shown in Fig. 5.2(a). The net result is the production of the entangled pair of photons with frequencies $\omega_c + \omega$ and $\omega_c - \omega$. These two outputs will be combined in the next section to generate two mode squeezing.

5.2 Squeezing spectra

For studying the squeezing spectra, we combine the output fields $\delta a_{1\text{out}}$ and $\delta a_{2\text{out}}$ to construct the field d as shown in Fig. 5.3. To make it more general, we add a phase difference θ between the output fields, then $d(t)$ can be written as

$$d(t) = \frac{1}{\sqrt{2}}[\delta a_{1\text{out}}(t) + \mathrm{e}^{i\theta}\delta a_{2\text{out}}(t)] = \frac{1}{\sqrt{2}}[\tilde{b}_{1\text{out}}(t) + \mathrm{e}^{i\theta}\tilde{b}_{2\text{out}}(t)]\mathrm{e}^{-i\omega_c t}. \tag{5.17}$$

In the frame rotating with the cavity frequency ω_c,

$$\tilde{d}(t) = d(t)\mathrm{e}^{i\omega_c t} = \frac{1}{\sqrt{2}}[\tilde{b}_{1\text{out}}(t) + \mathrm{e}^{i\theta}\tilde{b}_{2\text{out}}(t)], \tag{5.18}$$

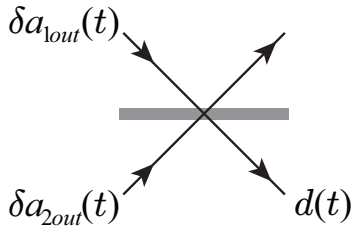

Figure 5.3: The combination of the output fields $\delta a_{i\text{out}}$'s from two cavities using a 50/50 beam splitter.

which obeys the commutation relation $[\tilde{d}(t), \tilde{d}^\dagger(t')] = \delta(t-t')$. We define as usual the quadrature variable $X_\phi(t) = [\tilde{d}(t)\mathrm{e}^{-i\phi} + \tilde{d}^\dagger(t)\mathrm{e}^{i\phi}]/\sqrt{2}$, and hence in the frequency domain

$$\begin{aligned}
X_\phi(\omega) &= \frac{1}{\sqrt{2}}[\tilde{d}(\omega)\mathrm{e}^{-i\phi} + \tilde{d}^\dagger(-\omega)\mathrm{e}^{i\phi}] \\
&= \frac{1}{2}\Big[\Big(\tilde{b}_{1\text{out}}(\omega) + \mathrm{e}^{i\theta}\tilde{b}_{2\text{out}}(\omega)\Big)\mathrm{e}^{-i\phi} + \Big(\tilde{b}^\dagger_{1\text{out}}(-\omega) + \mathrm{e}^{i\theta}\tilde{b}^\dagger_{2\text{out}}(-\omega)\Big)\mathrm{e}^{i\phi}\Big] \\
&= \frac{1}{2}\Big[E_{se}(\omega)\tilde{b}_{1\text{in}}(\omega) + E^*_{se}(-\omega)\tilde{b}^\dagger_{1\text{in}}(-\omega) + E_{si}(\omega)\tilde{b}_{1\text{int}}(\omega) + E^*_{si}(-\omega)\tilde{b}^\dagger_{1\text{int}}(-\omega) \\
&\quad + F_{se}(\omega)\tilde{b}_{2\text{in}}(\omega) + F^*_{se}(-\omega)\tilde{b}^\dagger_{2\text{in}}(-\omega) + F_{si}(\omega)\tilde{b}_{2\text{int}}(\omega) + F^*_{si}(-\omega)\tilde{b}^\dagger_{2\text{int}}(-\omega) \\
&\quad + V_s(\omega)f(\omega) + V^*_s(-\omega)f^\dagger(-\omega)\Big],
\end{aligned} \tag{5.19}$$

where

$$\begin{aligned}
E_{se}(\omega) &= [2\kappa_{e1}E_{s1}(\omega) - 1]\mathrm{e}^{-i\phi} + \sqrt{2\kappa_{e1}}\sqrt{2\kappa_{e2}}F^*_{s2}(-\omega)\mathrm{e}^{i\phi-i\theta}, \\
E_{si}(\omega) &= \sqrt{2\kappa_{e1}}\sqrt{2\kappa_{i1}}E_{s1}(\omega)\mathrm{e}^{-i\phi} + \sqrt{2\kappa_{e2}}\sqrt{2\kappa_{i2}}F^*_{s2}(-\omega)\mathrm{e}^{i\phi-i\theta}, \\
F_{se}(\omega) &= [2\kappa_{e2}E_{s2}(\omega) - 1]\mathrm{e}^{i\theta-i\phi} + \sqrt{2\kappa_{e1}}\sqrt{2\kappa_{e2}}F^*_{s1}(-\omega)\mathrm{e}^{i\phi}, \\
F_{si}(\omega) &= \sqrt{2\kappa_{e2}}\sqrt{2\kappa_{i1}}E_{s2}(\omega)\mathrm{e}^{i\theta-i\phi} + \sqrt{2\kappa_{e1}}\sqrt{2\kappa_{i2}}F^*_{s1}(-\omega)\mathrm{e}^{i\phi}, \\
V_s(\omega) &= \sqrt{2\kappa_{e1}}V_{s1}(\omega)\mathrm{e}^{-i\phi} + \sqrt{2\kappa_{e2}}V^*_{s2}(-\omega)\mathrm{e}^{i\phi-i\theta}.
\end{aligned} \tag{5.20}$$

The squeezing spectrum defined as $\langle X_\phi(\omega)X_\phi(\omega')\rangle = 2\pi S_\phi(\omega)\delta(\omega+\omega')$ can then be obtained using the correlation relations (5.12)

$$S_\phi(\omega) = \frac{1}{4}\Big[|E_{se}(\omega)|^2 + |F_{se}(\omega)|^2 + |E_{si}(\omega)|^2 + |F_{si}(\omega)|^2 + |V(\omega)|^2\gamma_m(\bar{n}_{\rm th}+1) + |V(-\omega)|^2\gamma_m\bar{n}_{\rm th}\Big]. \tag{5.21}$$

We note that if $\tilde{d}(t)$ were a vacuum field, then

$$S_\phi(\omega) = 1/2. \tag{5.22}$$

Hence we define the normalized squeezed parameter as $2S_\phi(\omega)$. The magnitude of squeezing in dB units is then $-10\log_{10}(2S_\phi)$. For identical cavities 1 and 2, we set $\kappa_{e1} = \kappa_{e2} = \kappa_e$, $\kappa_{i1} = \kappa_{i2} = \kappa_i$ and we define the output coupling ratio $\eta = \kappa_e/\kappa = \kappa_e/(\kappa_e+\kappa_i)$. The amplitude quadrature ($\phi = 0$) of the output field is

$$\begin{aligned}
S_0(\omega) &= \frac{1}{4}\Big[|[2\kappa_e E_{s1}(\omega) - 1] - 2\kappa_e F^*_{s2}(-\omega)|^2 + |[2\kappa_e E_{s2}(\omega) - 1] - 2\kappa_e F^*_{s1}(-\omega)|^2 \\
&\quad + 2\kappa_e 2\kappa_i\Big|\Big[E_{s1}(\omega) - F^*_{s2}(-\omega)\Big]\Big|^2 + 2\kappa_e 2\kappa_i|E_{s2}(\omega) - F^*_{s1}(-\omega)|^2 \\
&\quad + 2\kappa_e|V_{s1}(\omega) - V^*_{s2}(-\omega)|^2\gamma_m(\bar{n}_{\rm th}+1) + 2\kappa_e|V_{s1}(-\omega) - V^*_{s2}(\omega)|^2\gamma_m\bar{n}_{\rm th}\Big] \\
&= \frac{1}{4}\Big[|[2\kappa\eta E_{s1}(\omega) - 1] - 2\kappa\eta F^*_{s2}(-\omega)|^2 + |[2\kappa\eta E_{s2}(\omega) - 1] - 2\kappa\eta F^*_{s1}(-\omega)|^2 \\
&\quad + 4\kappa^2\eta(1-\eta)\Big|\Big[E_{s1}(\omega) - F^*_{s2}(-\omega)\Big]\Big|^2 + 4\kappa^2\eta(1-\eta)|E_{s2}(\omega) - F^*_{s1}(-\omega)|^2 \\
&\quad + 2\kappa\eta|V_{s1}(\omega) - V^*_{s2}(-\omega)|^2\gamma_m(\bar{n}_{\rm th}+1) + 2\kappa\eta|V_{s1}(-\omega) - V^*_{s2}(\omega)|^2\gamma_m\bar{n}_{\rm th}\Big] \\
&= \kappa^2\eta^2\Big[|E_{s1}(\omega) - F^*_{s2}(-\omega) - \frac{1}{2\kappa\eta}|^2 + |E_{s2}(\omega) - F^*_{s1}(-\omega) - \frac{1}{2\kappa\eta}|^2 \\
&\quad + (\frac{1}{\eta}-1)\Big|\Big[E_{s1}(\omega) - F^*_{s2}(-\omega)\Big]\Big|^2 + (\frac{1}{\eta}-1)|E_{s2}(\omega) - F^*_{s1}(-\omega)|^2\Big] \\
&\quad + \frac{1}{2}\kappa\eta\Big[|V_{s1}(\omega) - V^*_{s2}(-\omega)|^2\gamma_m(\bar{n}_{\rm th}+1) + |V_{s1}(-\omega) - V^*_{s2}(\omega)|^2\gamma_m\bar{n}_{\rm th}\Big] \\
&= \Big\{\frac{1}{2} + \kappa\eta\Big[\kappa|E_{s1}(\omega) - F^*_{s2}(-\omega)|^2 + \kappa|E_{s2}(\omega) - F^*_{s1}(-\omega)|^2\Big] \\
&\qquad\qquad - {\rm Re}[E_{s1}(\omega) - F^*_{s2}(-\omega)] - {\rm Re}[E_{s2}(\omega) - F^*_{s1}(-\omega)]\Big]\Big\} \\
&\quad + \frac{1}{2}\kappa\eta\Big[|V_{s1}(\omega) - V^*_{s2}(-\omega)|^2\gamma_m(\bar{n}_{\rm th}+1) + |V_{s1}(-\omega) - V^*_{s2}(\omega)|^2\gamma_m\bar{n}_{\rm th}\Big].
\end{aligned} \tag{5.23}$$

5.3 Squeezing in the output fields from double-cavity optomechanics

We have studied the physics of the squeezing process in optomechanics in analogy to the down conversion process, and we expect (5.21) to yield squeezing. We illustrate

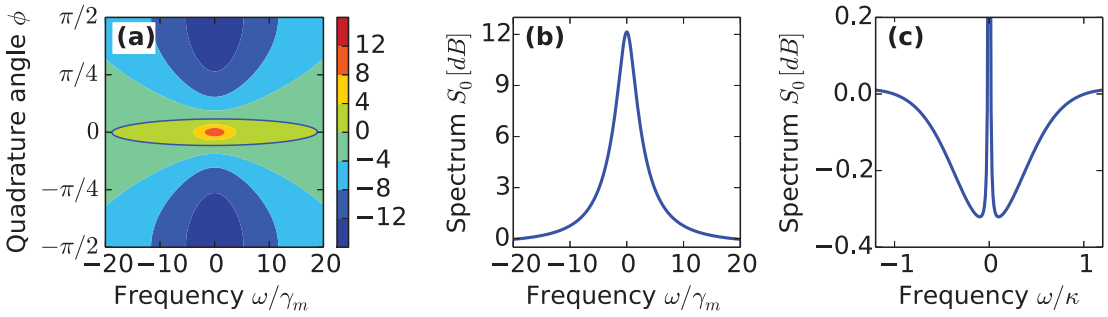

Figure 5.4: (a) The density plot of the squeezing spectra of the output field $b(\omega)$ with $-\Delta_1 = \Delta_2 = \omega_m$ at zero temperature. The middle region between the thick contours is squeezed. (b) The squeezing spectrum ($\phi = 0$) scaled with γ_m. (c) The squeezing spectrum ($\phi = 0$) scaled with $\kappa = 1000\gamma_m$. The parameter set used in the plots are $\omega_m = 2\pi \times 50$MHz, $\kappa = 2\pi \times 1$MHz, $\gamma_m = 2\pi \times 1$kHz, $G_2 = i2\pi \times 0.1$MHz ($C_2 = 20$), $G_1 = -G_2/\sqrt{2}$ ($C_1 = 10$), $\delta_1 = \delta_2 = 0$ and $\theta = \pi$.

the features of our two mode squeezing in the output field $d(t)$ in Fig. 5.4(a) with $\theta = \pi$ and for cooperativities $C_2 = 2C_1 = 20$. We first ignore the effects of internal loss by setting $\eta = 1$. In the plot, we set $\kappa_1 = \kappa_2 = \kappa$. The complete set of parameters is given in the caption. To create this map, we used (5.21) at zero temperature. In the diagram, we observe the largest magnitude of squeezing in the amplitude quadrature S_0 (see Fig. 5.4(b)). The magnitude of squeezing at $\omega = 0$ is about 12dB. As one rotates towards the phase quadrature $S_{\pi/2}$, the squeezing magnitude decreases and it eventually turns into antisqueezing. In Fig. 5.4(c), we show the spectrum in a larger scale, and we find that the squeezing only occurs in the frequency region with ω/γ_m small. There is an antisqueezing noise floor with a full-width close to κ. When ω further increases to be comparable to κ, the optomechanical interaction becomes

negligible and the spectrum turns into vacuum noise, $S_0(\omega) = 0$dB.

In Fig. 6.6, we show in detail the dependence of the squeezing on the cooperativity parameters C_1 and C_2. Before we discuss Fig. 6.6, we analyse the situation analytically. We find that under the approximation $\gamma_m, \kappa_i \ll \omega_m$, the peak value is given by

$$\begin{aligned} S_0(0) &= \frac{1 + (\sqrt{C_1} - \sqrt{C_2})^4}{2(1 - C_1 + C_2)^2} + \frac{(\sqrt{C_1} - \sqrt{C_2})^2(2\bar{n}_{\rm th} + 1)}{(1 - C_1 + C_2)^2} \\ &= \frac{\left[\frac{1}{C_2} + (1 - \sqrt{\frac{C_1}{C_2}})^2\right]^2}{2(1 - \frac{C_1}{C_2} + \frac{1}{C_2})^2} + \frac{(1 - \sqrt{\frac{C_1}{C_2}})^2}{(1 - \frac{C_1}{C_2} + \frac{1}{C_2})^2} \cdot \frac{2\bar{n}_{\rm th}}{C_2}. \end{aligned} \tag{5.24}$$

The first term in (5.24) describes the noise squeezing of the input vacuum field and the second term arises from the noise due to the thermal bath phonons. A short derivation shows that $S_0(0)$ approaches to its minimum value

$$S_{\rm min}(0) = \frac{\bar{n}_{\rm th} + 1}{2(C_2 + \bar{n}_{\rm th} + 1)}, \tag{5.25}$$

when $\frac{C_1}{C_2} \to [(1 + \frac{\bar{n}_{\rm th}+1}{C_2}) - \sqrt{\frac{1}{C_2} + (\frac{\bar{n}_{\rm th}+1}{C_2})^2}]^2$ for given C_2. For $C_i \gg 1$, they can be approximated as $S_{\rm min} = \frac{\bar{n}_{\rm th}+1}{2C_2+2\bar{n}_{\rm th}}$ when $\frac{C_1}{C_2} \to [1 - \frac{1}{\sqrt{C_2}}]^2$, *i.e.* $\sqrt{C_2} - \sqrt{C_1} \to 1$. Thus the squeezing reaches its maximum magnitude at this limit and it decreases to 0 as one further increases $C_1/C_2 \to 1$. In the limit $C_1 = C_2$, $\kappa_1 = \kappa_2$ and $\delta_1 = \delta_2 = 0$; we see from Eq. 5.11 that the cavity modess couple effectively only to one quadrature of the mechanical mode. It thus hinders the active participation of the mechanical mode in the squeezing process as the mediating mechanism, and hence there is no squeezing as seen from Eq.(5.24). This is in agreement with a recent result [113] that the system acts more like a phase insensitive amplifier.

Alternatively, if we fix the ratio C_1/C_2, the squeezing magnitude $S_0(0)$ can be increased by increasing C_2. The squeezing magnitude $S_0(0)$ is a monotonic increasing function of C_2 and it approaches an asymptotic value $S_0(0) \to \frac{1}{2}\left(\frac{1-\sqrt{C_1/C_2}}{1+\sqrt{C_1/C_2}}\right)^2$ at zero temperature. This behaviour is shown in detail in Fig. 5.5(c). This result holds if $1 - \sqrt{C_1/C_2} \gg 1/\sqrt{C_2}$, otherwise it goes to 1/2 if $C_1 = C_2$.

We illustrate the dependence of the squeezing magnitude on the cooperativity parameter or on the pump power in Fig. 5.5. Fig. 5.5(a) shows the squeezing spectrum

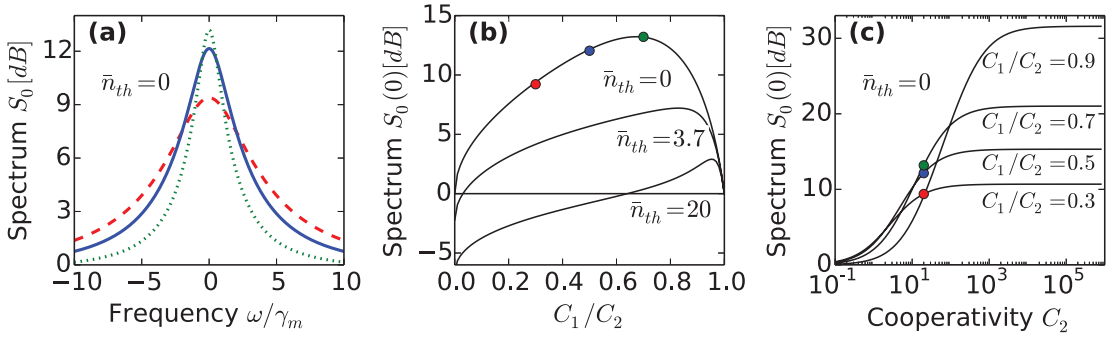

Figure 5.5: (a) The squeezing spectra ($\phi = 0$) with $C_1/C_2 = 0.3$(red dashed), $= 0.5$(blue full) and $= 0.7$(green dotted) at $T = 0$. (b) The squeezing magnitude at $\omega = 0$ versus C_1/C_2 by fixing $C_2 = 20$ at different temperatures. (c) The squeezing magnitude at $\omega = 0$ versus C_2 for different ratios of C_1/C_2 at $\bar{n}_{\rm th} = 0$. The three dots on top of the curves in (b) and (c) correspond to different curves in (a). Other parameters are the same as in Fig. 5.4.

under different ratios of C_1/C_2 and we see that squeezing spectrum gains magnitude but loses width when C_1/C_2 increases from 0.3(dashed) to 0.5(full) and 0.7(dotted). This can be roughly understood from the smallest root of the denominator $D(\omega)$, given by Eqs.(S12). The smallest root occurs at $\omega = -i(1 - C_1 + C_2)\frac{\gamma_m}{2}$. In Fig. 5.5(b), we plot the squeezing magnitude at $\omega = 0$ as a function of C_1/C_2 when the temperatures are both zero and nonzero. We see that when $C_1 = 0$, the vacuum optical inputs only interact with cavity 2, and no squeezing process is taking place. The incoherent phonons from the mirror in the thermal bath result in fluctuations in the optical output field, hence $S_0(0) \leq 0$ when $T \geq 0$. The magnitude of squeezing $S_0(0)$ increases with increasing C_1/C_2 until it reaches the maximum squeezing. At $T = 0$ and $C_2 = 20$, the maximum squeezing occurs at $C_1/C_2 \cong 0.67$ and $S_0(0) \cong 0.024 = 13$dB. The system loses squeezing magnitude after this point if C_1/C_2 keeps increasing.

The internal losses in the optomechanical system would degrade squeezing. When the cavities are subject to internal losses, $\eta < 1$, the terms in the curly bracket increases from a small value to 1/2, and hence the squeezing magnitude is degraded. However, the last term indicates that finite internal loss reduces the effect of the mechanical noise and, in this aspect, it is beneficial for squeezing. The squeezing magnitude at $\omega = 0$ becomes

$$S_0(0) = \frac{1}{2}(1-\eta) + \left[\frac{1+(\sqrt{C_1}-\sqrt{C_2})^4}{2(1-C_1+C_2)^2} + \frac{(\sqrt{C_1}-\sqrt{C_2})^2(2\bar{n}_{\rm th}+1)}{(1-C_1+C_2)^2}\right]\eta. \qquad (5.26)$$

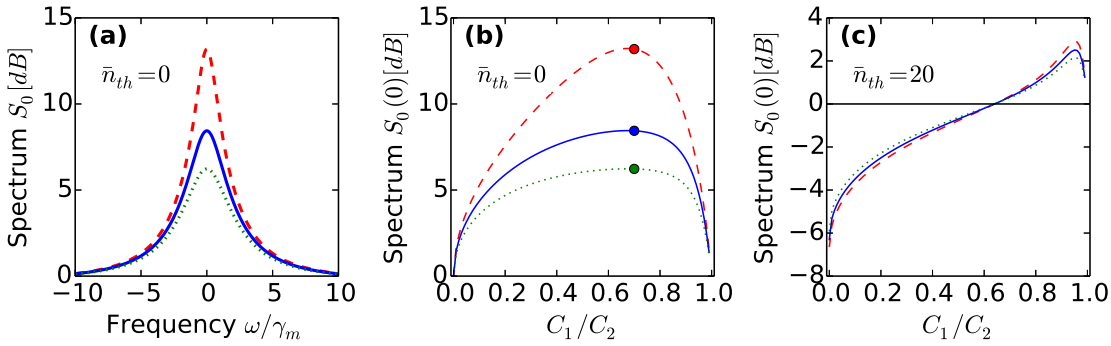

Figure 5.6: The squeezing spectra with internal losses characterized by $\eta = \kappa_e/(\kappa_e + \kappa_i)$ and for $C_2 = 20$. The curves are corresponding to $\eta = 1$(red dashed), $= 0.9$(blue full) and $= 0.8$(green dotted), respectively. Part (a) gives the spectra as a function of ω for $C_1/C_2 = 0.7$ at $\bar{n}_{\rm th} = 0$. Part (b) gives the peak value $S_0(0)$ as a function of C_1/C_2 at $\bar{n}_{\rm th} = 0$. Part (c) gives the peak value $S_0(0)$ as a function of C_1/C_2 at a larger $\bar{n}_{\rm th} = 20$. Other parameters are the same as in Fig. 5.4.

Physically, optical vacuum noise couples into the cavities via both the external and internal decaying paths (κ_e and κ_i). They all participate in the squeezing process and contribute to the two mode squeezed vacuum state in the cavity fields. However, the intra-cavity fields only transform into the output fields from the external decay path κ_e. It means that the quantum correlation is partially lost from the internal decay

path κ_i, and eventually the squeezing magnitude in the output fields is degraded. Figure 5.6 shows the effect of the internal losses. The squeezing remains significant even in presence of $10-20\%$ internal losses.

The physics in the generation of the squeezed vacuum states can be interpreted using the FWM process via phonons, as shown in Fig. 5.7. In cavity 1, A blue

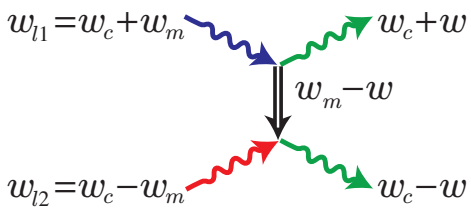

Figure 5.7: Generation of squeezed states via phonons in FWM process. The curly arrows represent photons and double-line arrow represents phonons.

detuned driving laser photon ($\omega_{l1}=\omega_c+\omega_m$), when being scattered by the mechanical oscillator, produces a phonon ($\omega_m-\omega$) and a photon at a lower frequency $\omega_c+\omega$. At the same time in cavity 2, a red detuned driving laser photon ($\omega_{l2}=\omega_c-\omega_m$) by absorbing the phonon ($\omega_m-\omega$) produces a photon at $\omega_c-\omega$. These processes are resonantly enhanced if both the generated photons are close to the cavity resonance frequency. Equivalently, the physics can be described by the effective Hamiltonian for the FWM process in Fig. 5.7: $a_{l1}a_{l2}\int\Phi(\omega)a^\dagger_{\omega_c-\omega}a^\dagger_{\omega_c+\omega}\mathrm{d}\omega+h.c.\approx\alpha\int\Phi(\omega)a^\dagger_{\omega_c-\omega}a^\dagger_{\omega_c+\omega}\mathrm{d}\omega+h.c.$, when the strong driving lasers a_{l1},a_{l2} can be approximated classically by a number α. Here $\Phi(\omega)$ depends on the details of the optomechanical cavities. Such an interaction has been extensively studied in quantum optics [36, 48, 112] and is known to lead to the generation of quantum entanglement as well as squeezing. In the context of double-cavity optomechanics, the generation of entangled pairs has been discussed previously [44, 114–116].

Our double-cavity optomechanics proposal is fundamentally different from the ponderomotive squeezing [117–120], which was experimentally realized by Brooks *et al.* [118] in ultracold atoms, by Purdy *et al.* [120] in a membrane setup, and

by Safavi-Naeini *et al.* [119] in a waveguide-coupled zipper optomechanical cavity. In their experiments, a coherent input at the cavity resonance frequency is applied and the quantum noise of coherent light is reduced by using radiation pressure to push the mechanical resonator which, in turn, feeds back on the light's phase. The output squeezed light is generated at the side-band of the cavity frequency detuned by ω_m, which is approximately equal to the cavity linewidth. The degree of noise reduction depends on the optomechanical coupling strength. They did not use the side-band resolved condition and reported reasonable squeezing (several dB) under experimental conditions. We work in the side-band resolved limit and by using two different parametric processes, where the driving lasers are red and blue detuned, produce photon pairs. Such photon pairs are then combined with a beam splitter to produce squeezing. As a benefit of this particular driving manner, the squeezed output fields are on resonance to the cavity frequency and hence can be made strong. The red detuned driving field, on the other hand, inherently ensures the stability without requiring any extra cooling laser as long as the red detuned pump interaction is stronger than the blue detuned one.

5.4 Effect of the Brownian noise of the mirror on squeezing

It is known that squeezing is degraded by any kinds of noise effects. In optomechanics, the Brownian noise of the mirror makes the observation of quantum effects difficult. As we analyzed in the last section, the squeezing mechanism in our scheme relies on the coherent phonons generated by the driving field to actively transfer quantum coherence between two cavity fields. However, at the same time, the mirror is mediated in the thermal reservoir which excites incoherent phonons and hence limits the purity of the squeezed fields. At a high temperature, the system even loses the squeezing ability. This is illustrated in Fig. 5.5(b), where the curve for $\bar{n}_{\rm th} = 20$ shows antisqueezing when $C_1/C_2 < 0.6$.

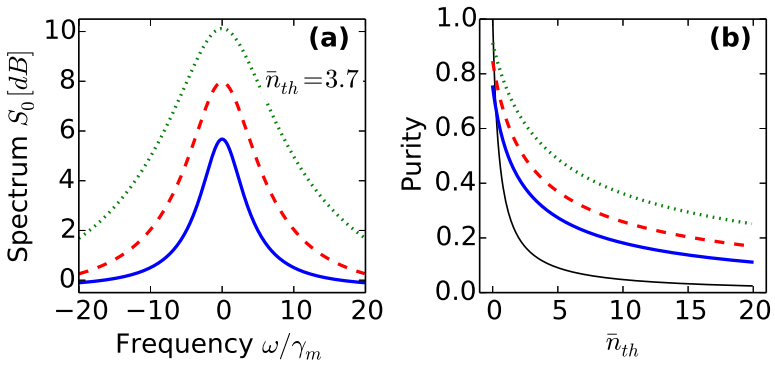

Figure 5.8: (a) The squeezing spectra ($\phi = 0$) at $T = 10$mK correspondingly $\bar{n}_{\rm th} = 3.7$; and (b) purity of the squeezed state with fixed $C_1/C_2 = 1/2$ and changing $C_2 = 20$(blue full), $= 40$(red dashed) and $= 80$(green dotted). Other parameters are the same as in Fig. 5.4. The thin black curve in (b) is the purity for a single mode thermal state.

We now investigate the effect of the V terms in (5.19) on the possible amount of squeezing. In Fig. 5.8(a), we plot the output field amplitude quadrature at a finite temperature $T = 10$mK and correspondingly $\bar{n}_{\rm th} = 3.7$. We assume that such a temperature is obtained either by using a dilution refrigerator [33, 121] or by precooling techniques [120]. Comparing the full curves in Fig. 5.5(a) and in Fig. 5.8(a) which are both plotted using the same parameters but with different bath temperatures, one can clearly see the squeezing magnitude decreases from 12 to 6 when the temperature increases from 0 to 10mK. With a larger phonon occupancy $\bar{n}_{\rm th}$, the second term in Eq.(5.24) dominates the spectrum $S_0(0)$. Interestingly, in our system, the decrease of squeezing due to rising the bath temperature can be compensated by increasing the cooperativity, in a way of enhancing the coupling constant or reducing the decaying rates. Now we concentrate on Fig. 5.8(a). When C_2 is increased from 20 (full) to 40 (dashed) and to 80 (dotted), the squeezing magnitude increases from 6dB to 8dB and 10dB, successively. The widths of the squeezed spectra are increased as well. This agrees with (5.24) from which we find that increasing C_2 essentially reduces the effect

of $\bar{n}_{\rm th}$. Equation (5.24) also suggests that a larger cooperativity is always preferable in order to generate a large squeezing magnitude at nonzero temperatures, although it never exceeds that of the zero temperature case. One has squeezing as long as the right hand side of (5.24) is less than 0.5. For $C_2 = 2C_1 = 20$, $S_0(0)$ has the value $0.030+0.028\bar{n}_{\rm th}$. Fig. 5.5(b) also indicates that the increasing $\bar{n}_{\rm th}$ shifts the optimized ratio of cooperativities C_1/C_2 for squeezing closer to 1.

We conclude this paper by giving a brief discussion of the state of the output field. In particular we discuss the purity of the generated state. The generated state is determined by several dissipative processes and the effects of thermal noise. Thus the state would in general be mixed. We expect that coherent interactions arising from the radiation pressure would make the state more and more pure. The purity of the state is given by the deviation of $\mathrm{Tr}\rho^2$ from unity. For the thermal state $\mathrm{Tr}\rho^2 = 1/(2\bar{n}_{\rm th}+1)$. The state of the output field $d(\omega)$ can be obtained from the quantum Langevin Eqs. 5.11. These equations imply that the field $d(\omega)$ will have a Gaussian Wigner function. For Gaussian states, the purity can be calculated from the known result for a single mode $\mathrm{Tr}\rho^2 = 1/\sqrt{\det\sigma}$ where σ is the covariance matrix of the state

$$\sigma = \begin{pmatrix} 2\langle X_0^2\rangle & \langle X_0 X_{\pi/2} + X_0 X_{\pi/2}\rangle \\ \langle X_0 X_{\pi/2} + X_0 X_{\pi/2}\rangle & 2\langle X_{\pi/2}^2\rangle \end{pmatrix}, \tag{5.27}$$

where $\langle X_0\rangle = \langle X_{\pi/2}\rangle$ which are zero under vacuum inputs. Here the operators X's are defined as in Eq.(5.19). For our system, different frequency modes of the output field are uncorrelated as can be seen from Eqs.(5.14) and (5.15) of the incoming vacuum fields and the mechanical Brownian noise. Hence, we can effectively use the result for the single mode. In Fig. 5.8(b), we plot the purity of the quantum state of the output field $d(\omega)$ for different C_2's. Note that the dissipative processes affect the purity of the state. As the temperature increases, the state purity decreases monotonically. The curves also show that the system with a higher cooperativity $C_2 = 80$ (top dotted

curve) loses purity slower than one with a lower cooperativity $C_2 = 20$ (bottom full curve). The state becomes more and pure as C_2 increases. This is quite consistent with the result for squeezing in the output fields.

5.5 Summary

To summarize the results, we have shown how squeezing of the order of 10dB or more can be generated in a double-cavity optomechanical system. We presented a detailed discussion of the conditions under which the double-cavity optomechanical system would lead to the generation of strong squeezing as a result of the generation of entangled photon pairs. We show that such a photon pair generation can be described by an effective interaction which is used for generating squeezing using parametric down conversion and four-wave mixing. However, there is one significant difference: we generate photon pairs by using active participation of phonons. The phonon mediated processes lead to additional noise terms which degrade squeezing. The purity of the generated squeezed light is stronger with a large cooperativity. In light of the recent progress in optomechanics experiments realizing large cooperativity in Ref. [42, 122], our proposal has promising experimental feasibility.

CHAPTER 6

GENERATING QUADRATURE SQUEEZED LIGHT WITH DISSIPATIVE OPTOMECHANICAL COUPLING

In optomechanical systems, Ponderomotive squeezing of light [117, 119, 120] using a on resonance driving laser has been proved one of the most promising ways to generate squeezed light in cavity optomechanics. Safavi-Naeini *et al.* [119] fabricated a micromechanical cavity resonator from a silicon microchip and observed the fluctuation spectrum at a level $(4.5 \pm 0.2)\%$ below the shot-noise limit despite the highly excited thermal state of the mechanical resonator (10^4 phonons). Purdy *et al.* [120] placed a low-mass partially reflective membrane made of silicon nitride in the middle of an optical cavity and pushed the squeezing limit to 32% (1.7dB) by cooling the membrane to about 1mK. Additional ways of producing optical squeezing in optomechanical systems have also been proposed. One example is use of a double-cavity optomechanical system to generate two-mode squeezed light [123]. Another example [124] is generation of quadrature squeezed light using the dissipative nature of the mechanical resonator in a single cavity driven by two differently detuned lasers. In a closely related subject, Lehnert and co-workers reported the experimental realization of entanglement between cavity output photon-photon pairs [125] and entanglement between mechanical motion and microwave fields [126].

It should be noted that much of the work on cavity optomechanics uses dispersive coupling. However, there are a few studies for dissipative coupling [127–134]—the intrinsic cavity lifetime depends on the mechanical motion. A theoretical analysis of dissipative coupling in cavity optomechanics was reported by Elste *et al.* [127].

They pointed out that the system gives rise to a remarkable quantum noise interference effect which leads to the Fano line shape in the back-action force noise spectra. Experimentally, Li *et al.* [128] for the first time reported dissipative coupling in a cavity optomechanics system that comprises a microdisk and a vibrating nanomechanical beam waveguide. Based on such a setup, Huang and Agarwal [129] proposed a scheme to beat the standard quantum limit (SQL) by irradiation of squeezed light into the cavity. Hammerer and co-workers [130, 131] concentrated on dissipative coupling by placing an optomechanical membrane inside a Michelson-Sagnac interferometer. This scheme is advantageous in the sense that the dissipative coupling is not due to internal dissipation, but the output photons are detectable. Weiss *et al.* [132] presented a comprehensive study of dissipative coupling in both the weak and strong coupling limits, and they found the parameter regions for amplification of cooling as well as EIT and normal-mode splitting. Wu *et al.* [133] experimentally reported the application of torque sensing by using dissipative optomechanical coupling in a photonic crystal split-beam nanocavity. In 2015, Sawadsky *et al.* [135] demonstrated cooling starting from room temperature to 126mK based on the combined effect of dissipative and dispersive coupling. This is quite a remarkable development where the couplings can be changed adding flexibility to the operation. This significant cooling in this experiment encourages us to examine the optical squeezing that can be produced in dissipative optomechanical interaction.

In this chapter, I develop analytically the theory of ponderomotive squeezing in cavity optomechanics with dissipative coupling. I will show that the squeezing magnitudes with dissipative coupling are comparable to those achieved using dispersive coupling. Our novel squeezing scheme broadens the scope of the quantum study of nonlinear interaction in optomechanics. This proposal is based on the parameters reported in [135], however, it is not limited to this system and is applicable to any optomechanical systems that can provide combined interactions. This squeezing scheme

works in the unresolved sideband regime, which has advantages in its easier system fabrication requirements. Moreover, this particular parameter regime makes it feasible for obtaining squeezed light with low frequency mechanical oscillators, although thermal phonons are still an issue. We show that the system can generate a 3dB squeezed field by use of reasonable driving laser powers when the thermal phonon occupancy is as large as 1.5×10^5 (the corresponding bath temperature $T = 1\text{K}$). The effect of a higher bath temperature can be offset by increasing the driving laser power. As a by-product, my theory explains the new instability region for small pump laser red-detunings which was discovered in the experiment [135].

6.1 Theoretical model

We consider the optomechanical system described in the experiment [135] which couples a mechanical oscillator to a Michelson-Sagnac interferometer. In such an op-

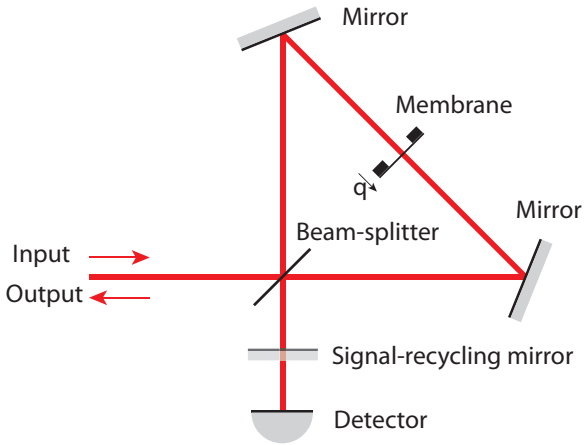

Figure 6.1: (a) Schematic of the Michelson-Sagnac interferometer which is coupled to the mechanical motion of a membrane.

tomechancial topology, the input laser beam is split into two counter-propagating directions and they both interact with a translucent and partially retroreflecting membrane. Altogether four light beams, including two arms which are either reflected or transmitted through the membrane, interference at the beam-splitter thereby form-

ing a Michelson-Sagnac interferometer. Without the signal-recycling mirror (SRM) in the interferometers output port, the interferometer corresponds to a compound mirror whose effective reflectivity depends on the position of the membrane. This compound mirror and the SRM together form an optomechanical system and the complete setup allows for tuning from strong dispersive to strong dissipative optomechanical coupling. When the membrane vibrates, the mechanical displacement q weakly modulates the cavity resonance frequency $\omega_c(q)$ and damping rate $\kappa(q)$. We expand them to linear order with respect to the normalized displacement Q to get $\omega_c(Q) \cong \omega_c - \sqrt{2}g_\omega Q$ and $\kappa(Q) \cong \kappa - \sqrt{2}g_\kappa Q$, where the dispersive coupling constant [1] $g_\omega = (\partial\omega_c/\partial q) * q_{\rm zpf}$ and the dissipative coupling constant $g_\kappa = (\partial\kappa/\partial q) * q_{\rm zpf}$. Typically, the dispersive coupling is larger than the dissipative coupling by a factor of $g_\omega/g_\kappa = \omega_c/\kappa \gg 1$. However, by placing a micro-membrane inside a Michelson-Sagnac interferometer, it has been shown that g_κ and g_ω can be made of the same order.

When the optomechanical system is driven by a strong laser with frequency ω_l and power $\mathcal{P}_l$, the Hamiltonian can be written, in the rotating frame, as

$$\begin{aligned} H = \hbar(\omega_c - \omega_l)a^\dagger a + \frac{1}{2}\hbar\omega_m(Q^2 + P^2) - \hbar\sqrt{2}g_\omega a^\dagger a Q \\ + i\hbar\sqrt{2\kappa(Q)}[a^\dagger(\tilde{\mathcal{E}}_l + a_{\rm in}) - H.c.], \end{aligned} \tag{6.1}$$

where $\tilde{\mathcal{E}}_l = \sqrt{\frac{\mathcal{P}_l}{\hbar\omega_l}}$ denotes the driving laser amplitude incident on the cavity [2] and $a_{\rm in}$ represents the input vacuum noise. To proceed, we linearize the Hamiltonian following the standard procedure by writing $a = a_s + a_1$, $P = P_s + P_1$ and $Q = Q_s + Q_1$. Here we use the subscript s instead of 0 for the mean values in order to distinguish them from the ones in the scenario of solely dispersive coupling. The mean values of the

[1] Note here the dispersive and dissipative coupling constant are defined differently from the ones in Ref. [57] by a factor of $\sqrt{2}$ for sake of consistent definition throughout this dissertation.

[2] Note also the difference between $\tilde{\mathcal{E}}_l$ defined here and $\mathcal{E}_l$ defined elsewhere in this dissertation. We keep the difference because when the cavity decay rate changes, the intra-cavity driving laser amplitude also gets modulated even at a constant laser power.

steady-state under both dissipative and dispersive couplings can be calculated as

$$a_s = \frac{\sqrt{2\kappa_s}\tilde{\mathcal{E}}_l}{\kappa_s + i\Delta_s}, \qquad Q_s = \sqrt{2}(\frac{g_\omega}{\omega_m} + \frac{\Delta_s g_\kappa}{\kappa_s \omega_m})|a_s|^2, \tag{6.2}$$

and $P_s = 0$. Under the effect of a driving laser, the mechanical oscillator displacement Q_s modulates both the cavity resonance frequency and the decay rate. Hence we define $\Delta_s = (\omega_c - \sqrt{2}g_\omega Q_s) - \omega_l$ as the driving laser detuning from the effective cavity resonance frequency; and we define $\kappa_s = \kappa - \sqrt{2}g_\kappa Q_s$ as the effective cavity decay rate. Both Δ_s and κ_s depend on the power of the driving laser. However, by tuning the driving laser frequency ω_l, one can always cause it to be on resonance with the effective cavity frequency, *i.e.* $\Delta_s = 0$. Under this condition, the effective cavity decay rate is determined by the quadratic equation $\kappa_s^2 - \kappa\kappa_s + 4\tilde{\mathcal{E}}_l^2 g_\omega g_\kappa/\omega_m = 0$. In typical OMS, the term $4\tilde{\mathcal{E}}_l^2 g_\omega g_\kappa/\omega_m$ is negligible compared to κ and hence $\kappa_s \cong \kappa$. For example with the parameters reported in [135], $4\tilde{\mathcal{E}}_l^2 g_\omega g_\kappa/\omega_m < \kappa/10^3$ when the driving power is below 10mW.

Then the linearized Hamiltonian takes the form $H = H_0 + H_{\text{int}} + H_{\text{damp}}$ and

$$\begin{aligned} H_0 &= \hbar\Delta_s a_1^\dagger a_1 + \frac{1}{2}\hbar\omega_m(Q_1^2 + P_1^2), \\ H_{\text{int}} &= -\hbar\frac{G_\omega^* a_1 + G_\omega a_1^\dagger}{\sqrt{2}}Q_1 - \hbar G_\kappa \frac{a_1^\dagger - a_1}{\sqrt{2}i}Q_1, \\ H_{\text{damp}} &= -\hbar\sqrt{2\kappa_s}(a_1^\dagger a_{\text{in}} - a_{\text{in}}^\dagger a_1) - \hbar\frac{G_\kappa a_{\text{in}}^\dagger - G_\kappa^* a_{\text{in}}}{2\sqrt{\kappa_s}}Q_1, \end{aligned} \tag{6.3}$$

where $G_{\omega,\kappa} = 2a_s g_{\omega,\kappa}$ is the driving field enhanced dispersive (dissipative) coupling constant between the optical quadrature $X(Y)$ and mechanical quadrature Q_1 [3]. The form of the Hamiltonian (6.6) suggests that it is more intuitive to write the cavity field in terms of its quadratures: $X = (a_1 + a_1^\dagger)/\sqrt{2}$, $Y = (a_1 - a_1^\dagger)/(\sqrt{2}i)$, and $[X, Y] = i$. In the contents of this section, we are interested in generating squeezed light in the output field. Under the effect of dissipative coupling, the standard input-output

[3]Note the extra factor of 2 in the definition of $G_{\omega,\kappa}$ compared to G defined elsewhere in this dissertation. They are related such that $G_\omega X Q_1 = (2a_s g_\omega)\frac{a_1+a_1^\dagger}{\sqrt{2}}\frac{b_1+b_1^\dagger}{\sqrt{2}} = G(a_1 + a_1^\dagger)(b_1 + b_1^\dagger)$.

relation reads

$$a_{\rm in} + a_{\rm out} = \sqrt{2\kappa_s}(1 + \frac{g_\kappa}{\sqrt{2}\kappa_s})a \approx \sqrt{2\kappa_s}a, \tag{6.4}$$

since $g_\kappa \ll \kappa_s$. This relation holds for the field quadrature $X_{\rm in} + X_{\rm out} \approx \sqrt{2\kappa_s}X$, and similarly for Y.

When the new type of optomechanical coupling is involved, we have to modify the stability conditions in solving the nonlinear Hamiltonian. We investigate the dynamics of the system using the quantum Langevin equation

$$\mathrm{d}\Psi(t)/\mathrm{d}t = \mathbb{M}\Psi(t) + \Psi_{\rm in}(t), \tag{6.5}$$

with

$$\Psi(t) = \begin{pmatrix} X(t) \\ Y(t) \\ Q_1(t) \\ P_1(t) \end{pmatrix}, \qquad \Psi_{\rm in}(t) = \begin{pmatrix} \sqrt{2\kappa_s}X_{\rm in}(t) \\ \sqrt{2\kappa_s}Y_{\rm in}(t) \\ -\frac{{\rm Im}G_\kappa}{\sqrt{2\kappa_s}}X_{\rm in}(t) \\ \xi(t) - \frac{{\rm Re}G_\kappa}{\sqrt{2\kappa_s}}Y_{\rm in}(t) \end{pmatrix}, \tag{6.6}$$

and

$$\mathbb{M} = \begin{pmatrix} -\kappa_s & \Delta_s & -{\rm Re}G_\kappa - {\rm Im}G_\omega & 0 \\ -\Delta_s & -\kappa_s & {\rm Re}G_\omega & 0 \\ 0 & 0 & 0 & \omega_m \\ {\rm Re}G_\omega & {\rm Re}G_\kappa + {\rm Im}G_\omega & -\omega_m & -\gamma_m \end{pmatrix}. \tag{6.7}$$

The system is stable if all the eigenvalues of the matrix $\mathbb{M}$ have negative real parts. Before we present the stability condition using the Routh-Hurwitz criterion, we would like to make the following approximation. When the driving laser frequency is not far off resonance ($\Delta_s \sim 0$), the steady state of the field $a_s \cong \sqrt{\frac{2}{\kappa_s}}\tilde{\mathcal{E}}_l(1 - i\frac{\Delta_s}{\kappa_s})$. Note that, although $G_{\omega,\kappa}$ is generally complex, the imaginary part is smaller than the real part by a factor of Δ_s/κ_s. In this paper, since we concentrate on the unresolved sideband limit regime, $\kappa_s \gg \omega_m > \Delta_s$, we can make the approximation $({\rm Re}G_{\omega,\kappa})^2 \cong G^2_{\omega,\kappa}$ with

good precision. We find the condition for stability in our system

$$\Delta_s(G_\omega^2+G_\kappa^2)-\omega_m(\kappa_s^2+\Delta_s^2)<0, \tag{6.8}$$

$$\frac{\omega_m\Delta_s}{2\kappa_s\gamma_m}(G_\omega^2+G_\kappa^2)+\omega_m^2+(\frac{\kappa_s^2+\Delta_s^2-\omega_m^2}{2\kappa_s+\gamma_m}+\frac{\gamma_m}{2})^2-(\frac{\gamma_m}{2})^2>0. \tag{6.9}$$

Note that when $G_\kappa \to 0$, these conditions reduces to the stability condition for the optomechanical system with purely dispersive coupling G_ω. In the unresolved sideband limit where $\kappa_s \gg \omega_m \gg \gamma_m$, G_{ω,κ_s} can be treated as purely real and the conditions (6.8)-(6.9) are simplified as

$$-\frac{\gamma_m}{2\kappa_s\omega_m}(\kappa_s^2+\Delta_s^2)^2<\Delta_s(G_\omega^2+G_\kappa^2)<\omega_m(\kappa_s^2+\Delta_s^2). \tag{6.10}$$

From this condition, one can see that the system is always stable when $\Delta_s=0$. For small negative $\Delta_s(\equiv \omega_c-\omega_l-g_\omega Q_s)$, the first inequality in (6.10) imposes a very tight condition on the stability. Especially with a very high mechanical quality factor $Q=\omega_m/\gamma_m$, the condition reduces to $(|2\Delta_s|/\kappa_s)(G_\omega^2+G_\kappa^2)/\kappa_s^2<1/Q$. This explains the instability region discovered in [135].

Hereafter, we first focus on the on resonance driving scenario ($\Delta_s=0$) and then discuss the squeezing effect with detuned driving by relaxing this condition. When $\Delta_s=0$, the coupling strength $G_{\omega,\kappa}$ is real. The dynamics of the system can be described using the quantum Langevin equations

$$\frac{1}{\omega_m}\ddot{Q}_1+\frac{\gamma_m}{\omega_m}\dot{Q}_1+\omega_m Q_1=G_\omega X+G_\kappa Y+\frac{G_\kappa}{\sqrt{2\kappa_s}}Y_{\rm in}+\xi, \tag{6.11}$$

$$\dot{X}=-\kappa_s X-G_\kappa Q_1+\sqrt{2\kappa_s}X_{\rm in}, \tag{6.12}$$

$$\dot{Y}=-\kappa_s Y+G_\omega Q_1+\sqrt{2\kappa_s}Y_{\rm in}. \tag{6.13}$$

Here, ξ models the Brownian noise acting on the mechanical oscillator, and it obeys $\langle\xi(t)\xi(t')\rangle=\gamma_m(2\bar{n}_{\rm th}+1)\delta(t-t')$, where $\bar{n}_{\rm th}$ is the mean phonon occupation number. The correlations for the vacuum field are $2\kappa_s\langle X_{\rm in}(t)X_{\rm in}(t')\rangle = 2\kappa_s\langle Y_{\rm in}(t)Y_{\rm in}(t')\rangle = \kappa_s\delta(t-t')$. In the unresolved-sideband limit $\kappa_s \gg \omega_m \gg \gamma_m$, hence the vacuum noise dominates over the Brownian mechanical noise at low $\bar{n}_{\rm th}$.

We illustrate the coupling relations of the quantum noises in the optomechanical system, in Fig. 6.2. The field quadratures are subjected to the vacuum input noise

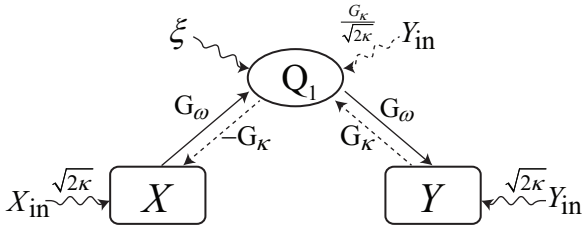

Figure 6.2: The input quantum noises and their coupling relations among different quadratures (X, Y) of the cavity field and mechanical mode (Q_1). The dashed arrows show the noise input and coupling due to dissipative coupling G_κ.

$X_{\rm in}$ and $Y_{\rm in}$. More importantly, we notice that, due to the dissipative coupling G_κ, the input vacuum noise $Y_{\rm in}$ is also coupled directly to the mechanical motion Q_1. At the same time, the form of the interaction Hamiltonian shows that Q_1 interacts with the different cavity quadratures at the rates G_ω and G_κ. Therefore, $Y_{\rm in}$ is fed into the system through two paths: (i) it directly couples to the cavity field; and (ii) it couples to the mechanical motion Q_1 dissipatively and then the optomechanical interaction transfers the noise to the cavity field. These two paths interfere in a coherent manner and lead to the Fano resonance in the cavity field spectrum.

We calculate the output field by combining Eqs.(6.4)-(6.13) after taking the Fourier transform, and find

$$(\kappa_s - i\omega + \chi G_\omega G_\kappa)X_{\rm out} + \chi G_\kappa^2 Y_{\rm out} = (\kappa_s - \chi G_\omega G_\kappa)X_{\rm in} - \sqrt{2\kappa_s}\chi G_\kappa \xi, \tag{6.14}$$

$$(\kappa_s - i\omega - \chi G_\omega G_\kappa)Y_{\rm out} - \chi G_\omega^2 X_{\rm out} = \chi G_\kappa^2 X_{\rm in} + (\kappa_s + 2\chi G_\omega G_\kappa)Y_{\rm in} - \sqrt{2\kappa_s}\chi G_\omega \xi, \tag{6.15}$$

where $\chi = \omega_m/(\omega_m^2 - \omega^2 - i\omega\gamma_m)$ is the mechanical susceptibility. Equations (6.14) and (6.15) describes how the input quantum noises add to the quantum fluctuation of the output fields. Without optomechanical interactions, the output field preserves the input field fluctuations, *i.e.* , $\langle X_{\rm out}^2\rangle = \langle Y_{\rm out}^2\rangle$. As one increases the optomechanical

interaction strengths G_ω and G_κ, the noises are distributed in a nonlinear manner. The squeezed states are generated when the variance is lower than that of the coherent state, *i.e.* , $S_\theta = \langle Z_\theta^2 \rangle < 1/2$ for a specific quadrature $Z_{\theta\text{out}} = X_{\text{out}} \cos\theta + Y_{\text{out}} \sin\theta$.

The full solution of the cavity and mechanical modes used for the numerical plots can be calculated using Eqs. (6.5) and (6.7). The operators can be solved in the frequency domain by taking the Fourier Transform, so that $A^\dagger(-\omega) = [A(-\omega)]^\dagger$. Therefore,

$$\Psi(\omega) = \mathbb{T}\Psi_{\text{in}}(\omega), \tag{6.16}$$

and

$$\begin{aligned}
\mathbb{T} &= -(\mathbb{M} + i\omega\mathbb{1})^{-1} \\
&= \frac{1}{D(\omega)} \begin{pmatrix}
\kappa_s - i\omega - \chi G_\omega G_\kappa & \Delta_s - \chi G_\kappa^2 \\
-\Delta_s + \chi G_\omega^2 & \kappa_s - i\omega + \chi G_\omega G_\kappa \\
\chi[G_\omega(\kappa_s - i\omega) - \Delta_s G_\kappa] & \chi[G_\kappa(\kappa_s - i\omega) + \Delta_s G_\omega] \\
-i\omega\frac{\chi}{\omega_m}(\gamma_m - i\omega)[G_\omega(\kappa_s - i\omega) - \Delta_s G_\kappa] & -i\omega\frac{\chi}{\omega_m}(\gamma_m - i\omega)[G_\kappa(\kappa_s - i\omega) + \Delta_s G_\omega]
\end{pmatrix} \\
&\qquad \begin{pmatrix}
\frac{\chi}{\omega_m}(\gamma_m - i\omega)[-G_\kappa(\kappa_s - i\omega) + \Delta_s G_\omega] & \chi[-G_\kappa(\kappa_s - i\omega) + \Delta_s G_\omega] \\
\chi[G_\omega(\kappa_s - i\omega) + \Delta_s G_\kappa] & \\
\frac{\chi}{\omega_m}(\gamma_m - i\omega)[(\kappa_s - i\omega)^2 + \Delta_s^2] & \chi[(\kappa_s - i\omega)^2 + \Delta_s^2] \\
-\chi[(\kappa_s - i\omega)^2 + \Delta_s^2 + \Delta_s(G_\omega^2 + G_\kappa^2)] & -i\omega\frac{\chi}{\omega_m}[(\kappa_s - i\omega)^2 + \Delta_s^2]
\end{pmatrix},
\end{aligned} \tag{6.17}$$

where $D(\omega) = (\kappa_s - i\omega)^2 + \Delta_s^2 - \chi\Delta_s(G_\omega^2 + G_\kappa^2)$. The two-time correlation functions of the input noise and mechanical noise are given in (1.8) and the correlation functions in the frequency domain can be obtained by taking the Fourier transform yielding

$$\begin{aligned}
&\langle X_{\text{in}}(\omega) X_{\text{in}}(\omega') \rangle = \langle Y_{\text{in}}(\omega) Y_{\text{in}}(\omega') \rangle = \pi\delta(\omega - \omega'), \\
&\langle \xi(\omega)\xi(\omega') \rangle \cong 2\pi\gamma_m(2\bar{n}_{\text{th}} + 1)\delta(\omega + \omega'),
\end{aligned} \tag{6.18}$$

where $\bar{n}_{\text{th}} = [\exp(\frac{\hbar\omega_m}{K_B T}) - 1]^{-1}$ is the mean thermal phonon occupancy number in the limit of large mechanical quality factor. Under the effect of dissipative coupling, the input-output relation (6.4) for the field quadratures becomes

$$X_{\text{in}} + X_{\text{out}} \approx \sqrt{2\kappa_s} X, \qquad Y_{\text{in}} + Y_{\text{out}} \approx \sqrt{2\kappa_s} Y. \tag{6.19}$$

The general quadrature of the output field at any angle θ is

$$\begin{aligned}
Z_{\theta\text{out}}(\omega) &= X_{\text{out}}(\omega)\cos\theta + Y_{\text{out}}(\omega)\sin\theta \\
&= \sqrt{2\kappa_s}\sum_{j=1}^{4}(\mathbb{T}_{1j}\cos\theta + \mathbb{T}_{2j}\sin\theta)\Psi_{\text{in},j}(\omega) - (X_{\text{in}}(\omega)\cos\theta + Y_{\text{in}}(\omega)\sin\theta) \\
&= \Big[(2\kappa_s\mathbb{T}_{11} - 1)\cos\theta + 2\kappa_s\mathbb{T}_{21}\sin\theta\Big]X_{\text{in}}(\omega) \\
&\quad + \Big[(2\kappa_s\mathbb{T}_{12} + G_\gamma\mathbb{T}_{14})\cos\theta + (2\kappa_s\mathbb{T}_{22} + G_\gamma\mathbb{T}_{24} - 1)\sin\theta\Big]Y_{\text{in}}(\omega) \\
&\quad + \sqrt{2\kappa_s}\Big[\mathbb{T}_{14}\cos\theta + \mathbb{T}_{24}\sin\theta\Big]\xi(\omega), \\
&= A_{ZX}(\omega)X_{\text{in}}(\omega) + A_{ZY}(\omega)Y_{\text{in}}(\omega) + A_{Z\xi}(\omega)\frac{1}{\sqrt{\gamma_m}}\xi(\omega),
\end{aligned} \tag{6.20}$$

where the subscripts ij of $\mathbb{T}$ denotes the matrix element in the ith row and in jth column. The factor $1/\sqrt{\gamma_m}$ is added in the ξ term considering the correlation for the mechanical noise has a different dimension from that of the field quadrature as can be seen in (6.18). From the above equation, we can see that the quantum fluctuation $X_{\theta\text{out}}(\omega)$ in the output field originates from $X_{\theta\text{in}}(\omega)$, $Y_{\theta\text{in}}(\omega)$ and $\xi(\omega)$ scaled by the factors A_{ZX}, A_{ZY}, and $A_{Z\xi}$, respectively. The output field spectra can be calculated as

$$\begin{aligned}
S_{\theta\text{out}}(\omega) &= \frac{1}{2\pi}\langle Z_{\theta\text{out}}(\omega)Z_{\theta\text{out}}(\omega')\rangle \\
&= \frac{1}{2}|A_{ZX}(\omega)|^2 + \frac{1}{2}|A_{ZY}(\omega)|^2 + |A_{Z\xi}(\omega)|^2\frac{\omega}{\omega_m}[1 + \coth(\frac{\hbar\omega}{2K_BT})],
\end{aligned} \tag{6.21}$$

where

$$\begin{aligned}
A_{ZX}(\omega) &= \frac{1}{D(\omega)}\Big\{\Big[(\kappa_s^2 + \omega^2 - \Delta_s^2) - \chi\Delta_s(G_\omega^2 + G_\kappa^2)\Big]\cos\theta - 2\kappa_s\Delta_s\sin\theta \\
&\qquad - 2\kappa_s\chi G_\omega(G_\kappa\cos\theta - G_\omega\sin\theta)\Big\}, \\
A_{ZY}(\omega) &= \frac{1}{D(\omega)}\Big\{(\kappa_s^2 + \omega^2 - \Delta_s^2)\sin\theta - 2\kappa_s\Delta_s\cos\theta \\
&\qquad - \chi[G_\kappa(\kappa_s + i\omega) + \Delta_s G_\omega](G_\kappa\cos\theta - G_\omega\sin\theta)\Big\}, \\
A_{Z\xi}(\omega) &= \frac{\sqrt{2\kappa_s\gamma_m}\chi}{D(\omega)}\Big\{ - (\kappa_s - i\omega)(G_\kappa\cos\theta - G_\omega\sin\theta) + \Delta_s(G_\omega\cos\theta + G_\kappa\sin\theta)\Big\}.
\end{aligned} \tag{6.22}$$

In order to achieve squeezing of the cavity field, *i.e.* , to reduce the quadrature variance $S_{\theta\text{out}}(\omega)$, one needs to minimize the scale factors for each noise source. Note that at a low temperature T, $\coth[\hbar\omega/(2K_BT)] \to 1$. Considering the ratio of the leading terms $A_{Z\xi}/A_{ZX} \sim \sqrt{\gamma_m/\kappa_s}G_\kappa\chi \ll 1$, the contribution from the mechanical noise is orders of magnitudes smaller than the noise from the cavity field. Therefore, we should concentrate on minimizing $|A_{ZX}|^2$ and $|A_{ZY}|^2$.

6.2 Squeezing with purely dissipative coupling

The phenomenon of ponderomotive squeezing with purely dissipative coupling can be obtained by setting the dispersive coupling strength $G_\omega = 0$ and $\Delta_s = 0$, so that $Y_{\text{out}} \cong (\chi G_\kappa^2/\kappa_s)X_{\text{in}} + Y_{\text{in}}$ and $X_{\text{out}} + (\chi G_\kappa^2/\kappa_s)Y_{\text{out}} \cong X_{\text{in}}+$ mechanical noise. The vacuum input X_{in} is coupled, not only to X_{out}, but also to Y_{out} via the mediated mechanical mode Q_1 scaled by the mechanical suspectibility χ and dissipative coupling strength G_κ. When one measures the field $Z_{\theta\text{out}} = X_{\text{out}}\cos\theta + Y_{\text{out}}\sin\theta$ at $\theta \neq 0\,^\circ$ or $90\,^\circ$, Y_{out} interferes partially with X_{out} since $\chi(\omega)$ is generally complex. The interference leads to squeezed quantum noises. The output squeezing spectrum is

$$S_{\text{diss}} \cong \frac{1}{2} + \frac{G_\kappa^2}{\kappa_s}\big(2|\chi|^2\Gamma_{\text{diss}}\cos^2\theta - \text{Re}\chi\sin 2\theta\big), \tag{6.23}$$

where $\Gamma_{\text{diss}} = G_\kappa^2/(4\kappa_s) + \gamma_m(2\bar{n}_{\text{th}} + 1)$ is the effective mechanical damping rate. By optimizing θ and $\chi(\omega)$ we obtain the optimal squeezing magnitude

$$S_{\text{diss}}^{\text{opt}} = \frac{\gamma_m(4\bar{n}_{\text{th}} + 3)}{G_\kappa^2/\kappa_s + 2\gamma_m(4\bar{n}_{\text{th}} + 3)}. \tag{6.24}$$

The squeezing magnitude can be enhanced by a large effective dissipative optomechanical coupling strength $G_\kappa^2/(\kappa_s\gamma_m)$ and a low mean phonon occupancy number $\bar{n}_{\text{th}}$. The optimal squeezed quadrature angle lies at $\tan\theta_{\text{diss}}^{\text{opt}} \cong -\sqrt{4G_\kappa^2/(\kappa_s\gamma_m)}$, and $\theta_{\text{diss}}^{\text{opt}}$ approaches to $90\,^\circ$ with a large dissipative coupling strength G_κ. From the above analysis, we can see that the Ponderomotive squeezing relies solely on the interference

of two paths of $X_{\rm in}$. One needs to suppress the input noises $Y_{\rm in}$ and ξ by choosing a quadrature angle $\theta_{\rm disp}^{\rm opt}$ close to $90\,^\circ$. The output field shows anti-squeezing at $\omega = \omega_m$ when $\theta \neq 0$. To illustrate the squeezing effect, we plot the output field spectra at different quadratures in Figs. 6.3(a) and 6.3(b) by numerically solving the quantum Langevin equations (6.11)-(6.13). We use the parameters provided by the experiment reported in [135], and the specific values are given in the caption of Fig. 6.3. At the angle $\theta_{\rm diss}^{\rm opt}$, the output spectrum (as shown in (b)) is characterized by a large squeezing of ~ 40dB at frequency $\omega \sim \omega_m - 2\pi \times 15$Hz and anti-squeezing at $\omega = \omega_m$.

In the other limit when dispersive coupling solely governs the optomechanical interaction, *i.e.* , $G_\kappa = 0$, Eqs. (6.14) and (6.15) reduce to $X_{\rm out} \cong X_{\rm in}$ and $Y_{\rm out} \cong Y_{\rm in} + (\chi G_\omega^2/\kappa_s) X_{\rm in} +$ mechanical noise. This is the conventional Ponderomotive squeezing scheme. It shares a similar noise transformation with the one we discussed above. Hence we are able to observe a similar squeezing phenomenon, but the optimal squeezed quadrature is around $\tan\theta_{\rm disp}^{\rm opt} \cong \sqrt{\kappa_s\gamma_m/(2G_\omega^2)}$, and $\theta_{\rm disp}^{\rm opt}$ approaches 0 with a large dispersive coupling strength G_ω. The output squeezing spectrum is

$$S_{\rm disp} \cong \frac{1}{2} + \frac{G_\omega^2}{\kappa_s}\big(2|\chi|^2\Gamma_{\rm disp}\sin^2\theta + 2{\rm Re}\chi\sin 2\theta\big), \tag{6.25}$$

where $\Gamma_{\rm disp} = G_\omega^2/\kappa_s + \gamma_m(2\bar{n}_{\rm th}+1)$. By optimizing θ and $\chi(\omega)$ we obtain the optimal squeezing magnitude

$$S_{\rm disp}^{\rm opt} = \frac{\gamma_m(\bar{n}_{\rm th}+1)}{G_\omega^2/\kappa_s + 2\gamma_m(\bar{n}_{\rm th}+1)}. \tag{6.26}$$

This result is identical to the one derived in [117] and has been experimentally demonstrated in [119, 120]. The optimal output frequency is $(\omega-\omega_m)^2 = \Gamma_{\rm disp}\gamma_m/2 + \gamma_m^2/4$, which increases with coupling strength G_κ^2. We plot the output spectra of dispersive squeezing in Figs. 6.3(c) and 6.3(d), as a comparison with the dissipative squeezing in Figs. 6.3(a) and 6.3(b). The optimal squeezing spectrum has a quadrature angle close to 0. The optimal squeezing magnitude is shown as ~ 30dB, which agrees with Eq. (6.26). We observe similar output squeezed spectra, although the optimal

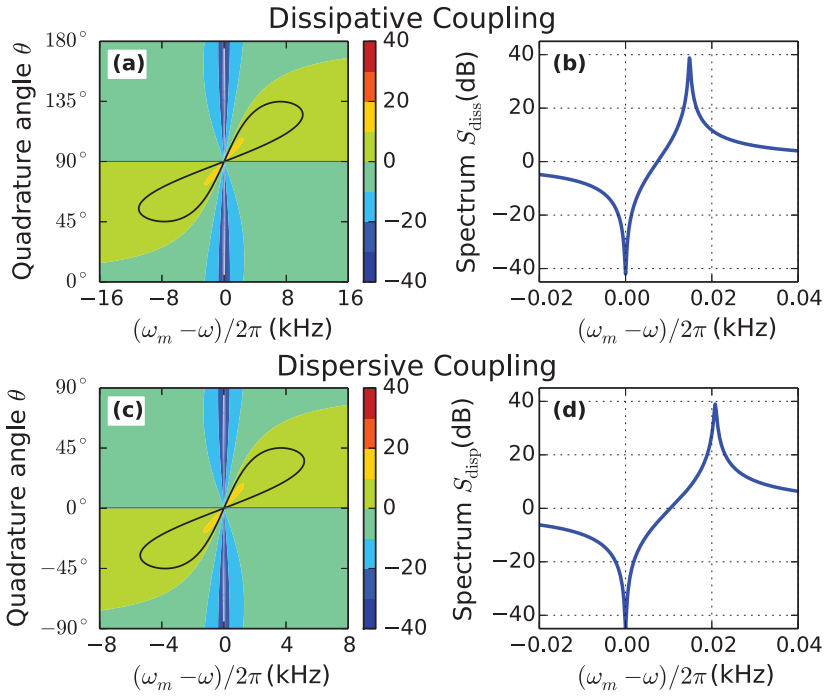

Figure 6.3: Comparison of squeezing spectra with purely dissipative coupling [(a) and (b)] and purely dispersive coupling [(c) and (d)]: The regions inside the black contours in the density plots (a) and (c) show 3dB squeezing region and the blue horizontal lines show the optimal quadratures which are plotted in (b) and (d), respectively. The dissipative coupling strength is $G_\kappa = 2\pi \times 150$ kHz with driving laser power $\mathcal{P}_l \sim 3.5$ W; the dispersive coupling strength is $G_\omega = 2\pi \times 75$ kHz with driving laser power $\mathcal{P}_l \sim 40$ mW. Other parameters are $\kappa_s = 2\pi \times 1.5$ MHz, $\omega_m = 2\pi \times 136$ kHz, $\gamma_m = 2\pi \times 0.23$ Hz, $\Delta_s = 0$ and $\bar{n}_{\rm th} = 0$.

squeezing magnitude is smaller than in Figs. 6.3(a) and 6.3(b) due to lower coupling strengths.

Physically both the dispersive coupling and the dissipative coupling generate optical squeezing in a similar manner, in the sense that they couple the input noise from one quadrature coherently to the other quadrature. Thus the input vacuum noise couples to the optomechanical system via two paths, as shown in Fig. 6.2. These two paths interfere and lead to squeezing. The optimal squeezing exists at different

quadrature angles due to the fact that G_ω couples noise from X to Y and G_κ couples noise from Y to X via the mechanical mode.

6.3 Squeezing with combined effects of dissipative and dispersive coupling

In the previous section, we studied squeezing phenomena with purely dispersive coupling or dissipative coupling. One natural question is whether the combined effect of these two coupling regimes could enhance the squeezing. We next study the generation of squeezed states in the presence of both coupling regimes G_ω and G_κ. When the driving laser frequency is on resonance, $\Delta_s = 0$, according to Eq.(6.14), the input vacuum fluctuations destructively interfere when $G_\omega G_\kappa \to \kappa_s/\chi$. Complete destructive interference exists only when χ is purely real, *i.e.* , $\omega \gg \omega_m$. The output squeezing spectrum is

$$S_{\rm disp} \cong \frac{1}{2} + (G_\kappa \cos\theta - G_\omega \sin\theta)^2 \left[\frac{2|\chi|^2 \Gamma_{\rm comb}}{\kappa_s} - \frac{{\rm Re}\chi}{\kappa_s} \left(\frac{2G_\omega \cos\theta - G_\kappa \sin\theta}{G_\kappa \cos\theta - G_\omega \sin\theta} \right) \right], \quad (6.27)$$

where $\Gamma_{\rm comb} = (4G_\omega^2 + G_\kappa^2)/(4\kappa_s) + \gamma_m(2\bar{n}_{\rm th} + 1)$. The optimal squeezing quadrature angle satisfies $\tan\theta_{\rm hybr}^{\rm opt} \sim G_\kappa/(2G_\omega)$ and the squeezing magnitude

$$S_{\rm comb}^{\rm opt} \cong \frac{1}{2} \cdot \frac{\gamma_m(2\bar{n}_{\rm th} + 1)}{(G_\omega^2 + G_\kappa^2/4)/\kappa_s + \gamma_m(2\bar{n}_{\rm th} + 1)}. \quad (6.28)$$

We see that the squeezing magnitude can be enhanced by increasing the coupling strengthes G_ω and G_κ for any given mean phonon number $\bar{n}_{\rm th}$. The squeezed quadrature rotates from quadrature X to quadrature Y as the ratio of the coupling strengths $G_\kappa/(2G_\omega)$ increases.

In Fig. 6.4(a), we plot the output spectra at different quadratures when the optomechanical system is subject to both dispersive and dissipative couplings. We set the coupling strengths such that $G_\omega = 5G_\kappa$ in accordance with the experimental parameters in [135]. The density plot resembles the main feature of Ponderomotive

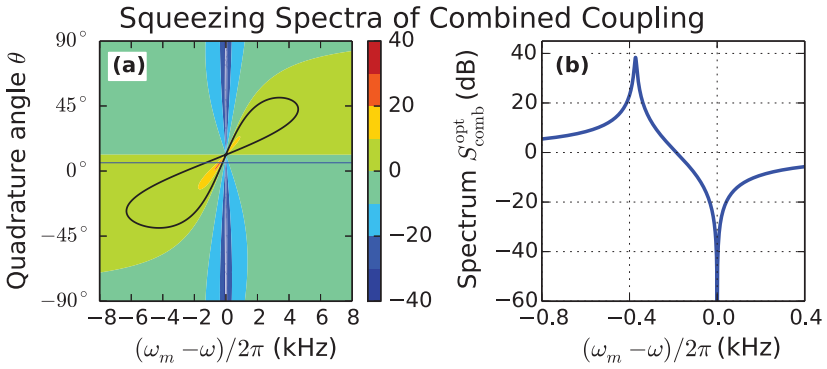

Figure 6.4: The density plots (a) and the optimal squeezing quadrature (b) of the output field spectra with combined dispersive and dissipative couplings. The regions inside the black contours in (a) show the 3 dB squeezing region and the blue horizontal line shows the optimal quadrature which is plotted in (b). The coupling strengths are $G_\omega = 2\pi \times 75$ kHz and $G_\kappa = 2\pi \times 15$ kHz with driving laser power $\mathcal{P}_l \sim 40$ mW. Other parameters are identical to those used in Fig. 6.3.

squeezing with purely G_ω or G_κ, except for a trivial quadrature difference. However, there are distinctions. The frequency bandwidth of the squeezing spectra increases at large quadrature angle and shrinks at lower quadrature angle. This is particularly advantageous in practice, since one usually focuses on a specific quadrature and hence one can make use of the larger bandwidth of the squeezed spectra.

In the optomechanical ponderomotive squeezing process, the mechanical element functions as an active mediating element and it provides coherent coupling between two field quadratures. At the same time, it is subject to the environmental Brownian noise which is incoherent with the cavity field. In the reported Ponderomotive squeezing experiments with purely dispersive optomechanical coupling, the environment temperature sets the limit of the squeezing magnitudes: Safavi-Naeini *et al.* [119] reported 0.2 dB squeezing at $\bar{n}_{\rm th} \sim 10^4$ and Purdy *et al.* [120] pushed the squeezing magnitude to 1.7 dB with a lower thermal phonon occupancy $\bar{n}_{\rm th} = 47$.

We now compare the effect of the thermal phonons on squeezing with different

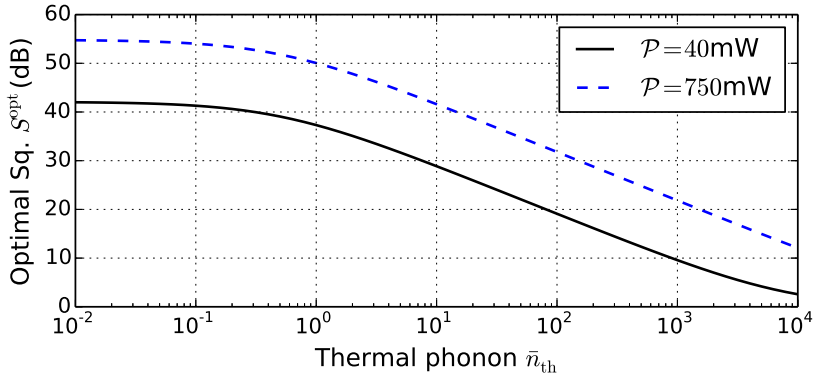

Figure 6.5: The effects of the mean thermal phonon occupation $\bar{n}_{\rm th}$ on the optimal squeezing magnitudes with different couplings. The optimal squeezing magnitudes are very similar for finite $\bar{n}_{\rm th}$ hence the three curves overlap.

optomechanical couplings. Equations. (6.24), (6.26) and (6.28) indicate that the output quadrature variance increases approximately proportionally to $\bar{n}_{\rm th}$ at large coupling rates. Comparing Eqs. (6.24) and (6.26), we find that optomechanical systems with purely dissipative coupling (G_κ) or purely dispersive coupling (G_ω) can generate squeezed fields of similar squeezing magnitude if $G_\kappa = 2G_\omega$. In Fig. 6.5(a), we illustrate the effects of the mean thermal phonon number on the optimal squeezing magnitude under different coupling regimes. The curves show that the squeezing magnitudes decrease with large thermal phonon occupancy $\bar{n}_{\rm th}$. Even when the thermal phonon number is as high as $\bar{n}_{\rm th} = 1000$, the system yields about 10dB squeezing with a combination of optomechanical couplings at $\mathcal{P}_l = 40$mW. If we increase the driving laser power to $\mathcal{P}_l = 150$mW, the squeezing magnitude increases to 15dB. Note that, this phonon number is however difficult to achieve with low mechanical frequency ω_m since $\bar{n}_{\rm th}$ is inversely proportional to ω_m. For example, the system has to be pre-cooled down to $T \sim 6.5$mK in order to get $\bar{n}_{\rm th} = 1000$. On the other hand at high bath temperature, large squeezing magnitude requires an increase in the coupling strength, which can be achieved by increasing the pump power. If the bath temper-

ature increases to $T = 1\text{K}$, the corresponding thermal phonon number increases to $\bar{n}_{\text{th}} \sim 1.5 \times 10^5$. One needs to increase the driving laser power to $\mathcal{P}_l \sim 750\text{mW}$ in order to get 3dB squeezing. For this power the system is still in the stable region.

Note however that the pump power cannot increase infinitely as too strong a pump laser leads to instability of the system dynamics. We discussed the stability condition in detail using the Routh-Hurwitz criterion in Sec. 6.1. For example, our linearization method breaks down and the system settles into instability when the laser power reaches $\mathcal{P}_l \sim 830\text{mW}$ for the parameters given above and the laser frequency set as $\omega_l = \omega_0 - 3\omega_m$. At this power, the coupling strengths are $G_\omega = 2\pi \times 250\text{kHz}$ and $G_\kappa = 2\pi \times 50\text{kHz}$. A lower driving laser frequency allows for a higher critical pump power. Our analysis also reveals an instable region when the effective driving laser detuning Δ_s has a small negative value. This explains the special instability region discovered in [135].

6.4 Squeezing with a fixed frequency driving laser

Sawadsky *et al.* [135] demonstrated a strong cooling effect in an OMS with both dissipative and dispersive coupling interactions. The experimental results agree remarkably well with the theoretical calculation. In the experiment, the authors fixed the driving laser frequency ω_l on resonance with the empty cavity resonance frequency ω_c. When the driving laser power increases, the effective cavity resonance frequency changes due to the displacement of the mechanical membrane and this leads to an effective detuning of the driving laser. In this section, we analyze the squeezing phenomena in an OMS driven by a laser with fixed frequency $\omega_l = \omega_c$. Under this condition, the effective detuning Δ_s and effective cavity decay rate κ_s can be determined by solving the nonlinear equation set (6.2). We use the parameters reported in [135]. The solution to (6.2) shows that $\kappa_s \sim \kappa$ when the driving laser power $\tilde{\mathcal{E}}_l$ is below 250 mW. However, the effective driving laser detuning Δ_s increases linearly

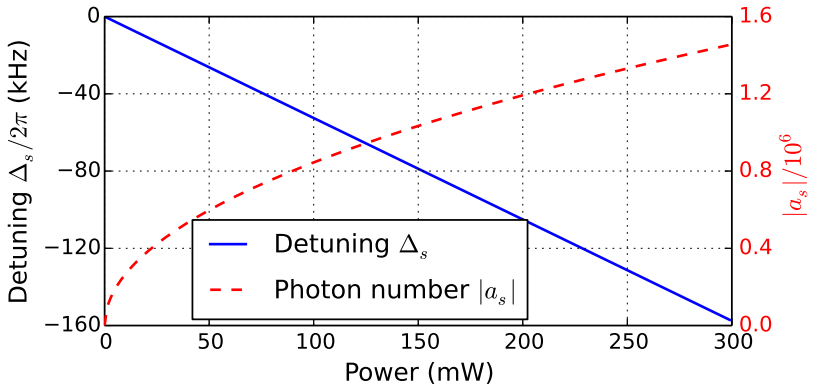

Figure 6.6: The change of the effective detuning and mean cavity photon number as the driving laser power increases from 0 to 200 mW. Other parameters are identical to those used in Figs. 6.4.

from 0 to a value close to $-\omega_m$, as shown in Fig. 6.6. The cavity mean photon number $|a_s|$ is also displayed in Fig. 6.6. When the driving laser power is set as 40mW, the effective detuning $\Delta_s = 2\pi \times 20$kHz. The corresponding coupling strengths remain at the values $G_\omega = 2\pi \times 75$kHz, which are similar to the ones used in Figs. 6.3 and 6.4. We show the squeezing spectra with different coupling interactions in Fig. 6.7 at zero temperature. Their optimal squeezing magnitudes reach close to 40 dB. We find large regions with over 3 dB squeezing in both spectra, as illustrated between the thick black 3 dB contour lines. We observe large regions of squeezing over 10 dB and in Fig. 6.7(b) even squeezing over 20 dB. The results are very similar to the ones in Figs. 6.3(a) and 6.4(a), and even the effects of temperature are similar so they are not discussed here.

6.5 Summary

To summarize the results, we have developed analytically the theory of Ponderomotive squeezing in cavity optomechanics with dissipative coupling. We show that the squeezing magnitudes with dissipative coupling are comparable to those achieved

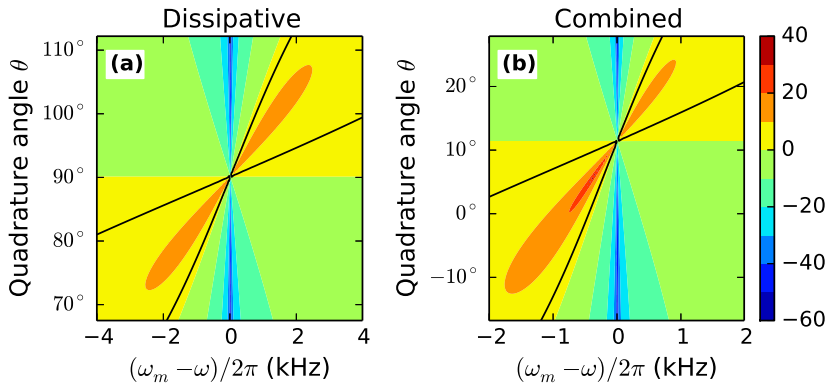

Figure 6.7: The squeezing spectra in an optomechanical system with (a) purely dissipative coupling $G_\kappa = 2\pi \times 150$kHz and $\mathcal{P}_l \sim 3.5$W, and (b) combined both couplings with $G_\omega = 5G_\kappa = 2\pi \times 75$ kHz and $\mathcal{P}_l \sim 40$ mW. Other parameters are identical to those used in Fig. 6.3 or 6.4. The regions beween the black contours have over 3dB squeezing.

using dispersive coupling. This novel squeezing scheme broadens the scope of the quantum study of nonlinear interaction in optomechanics. Our proposal is based on the parameters reported in [135], however, it is not limited to this system and is applicable to any optomechanical system that can provide combined interactions. This squeezing scheme works in the unresolved sideband regime, which has advantages in its easier system fabrication requirements. Moreover, this particular parameter regime makes it feasible for obtaining squeezed light with low frequency mechanical oscillators, although thermal phonons are still an issue. We show that the system can generate 3 dB squeezed field by using reasonable driving laser powers when the thermal phonon occupancy is as large as 1.5×10^5 (bath temperature $T = 1$ K correspondingly). The effect of higher bath temperature can be offset by increasing the driving laser power. As a by-product, our theory explains the new instability region for small pump laser red-detunings which was discovered in the experiment [135].

CHAPTER 7

CONCLUSIONS AND OUTLOOK

In optomechanics, which concerns the coupling between photons and phonons via radiation pressure — or most recently — also via optical gradient forces, the ultimate goal is to establish a complete control of the mechanical oscillator down to the single quantum level. The vigorous theoretical and experimental developments in cavity optomechanics during the past decade are constantly opening up new avenues with respect to applications and tests of the foundations of physics. In this dissertation, I presented my studies of the coherent effects and methods for generating squeezed state of light in cavity optomechanical systems, incorporating material from my publications [43, 53–57] and submission [52]. My research horizon is not limited to the effects within cavity OMS and it expands to the realms of quantum phenomena in atomic systems [67, 136] and fundamental quantum mechanics [137]. Most of my studies were motivated by recent experiments which push the state-of-art parameters in the optomechanical realm. On the other hand, many of my theoretical proposals have also been demonstrated experimentally with/by our collaborators or other groups in this field.

The aim of this dissertation has been to explore the coherent interference effects between optical/microwave and mechanical fields in optomechanical systems, and to study the generation of squeezed light by utilizing an active mechanical mode. In Chap. 1, I explained the the basis of the theoretical model of an optomechanical system by deriving the Hamiltonian and Heisenberg equations of motion. I presented the standard linearization procedure to solve the dynamical equations. The stability

of the dynamical equations was studied using the Routh-Hurwitz criterion.

In Chapter 2, I briefly introduced the EIT and explained the physics behind EIT by using the coherent photon-phonon interaction processes. I presented results for the transient EIT, and applied to storage and retrieval of optical pulses. Next, I adopted Ramsey's method of separated oscillatory fields to study coherences of the mechanical system in an optomechanical resonator. The high-resolution Ramsey fringes are observed in the emission optical field, when two pulses separated in time are applied. By collaborating with experimental groups, we performed the experimental demonstration using a silica microresonator.

In Chapter 3, I showed my prediction and experimental verification of electromagnetically induced absorption (EIA) in double-cavity OMS. I discussed the origin of EIA in OMS which exhibits the existence of an absorption peak within the transparency window. The full analytical results provide the width and the height of the EIA peak. I explained the effect in terms of the dynamics of three coupled oscillators (rather than two which is used to explain EIT) under different conditions on the relaxation parameters. The EIA is generic and can be observed in a variety of other systems. By collaborating with an experimental group, we demonstrated the EIA in metamaterials. In the last section, I also showed how double-cavity OMS enables us to achieve a transduction process to a number of different frequencies including, in principle, the possibility of transduction from optical to microwave frequencies. By tuning the frequency of the second cavity one can produce output fields at a range of frequencies. I presented analytical results for the steady-state behavior which is controlled by the power and the detuning of the field driving the second cavity.

In Chapter 4, I demonstrated the existence of Fano resonances in cavity optomechanics by identifying the interfering contributions to the fields generated at anti-Stokes and Stokes frequencies. Unlike the atomic systems, the optomechanical systems provide great flexibility as the width of the resonance is controlled by the

coupling field. I further showed how the double cavities coupled by a single optomechanical mirror can lead to the splitting of the Fano resonance and how the second cavity can be used to tune the Fano resonances. The Fano resonances are quite sensitive to the decay parameters associated with cavities and the mechanical mirror. Such resonances can be studied by both pump probe experiments as well as via the spectrum of the quantum fluctuations in the output fields.

In Chapter 5, I proposed a scheme for generating squeezed light by using a double-cavity optomechanical system driven by a blue detuned laser in one cavity and by a red detuned laser in the other. This double cavity system is shown to effectively mimic an interaction that is similar to the one for a downconverter, which is known to be a source of strong squeezing for light fields. There are however distinctions, as the phonons, which lead to such an interaction, can contribute to quantum noise. I showed that squeezing of the output fields, of the order of 10dB, can be achieved even for an effective mechanical mode occupation number of about 4 which for the chosen parameters corresponds to 10mK. These results are generic and applicable to a wide class of electro- and optomechanical systems involving interaction of two electromagnetic modes and one mechanical mode.

In Chapter 6, I studied a novel optomechanical interaction, namely, dissipative optomechanical coupling in which the mechanical displacement modulates the cavity decay rate, instead of the resonance frequency. This is based on a recent demonstration of cooling of a macroscopic silicon nitride membrane based on dissipative coupling. I theoretically showed that such a system in a cavity can yield good squeezing, which is comparable to that produced by dispersive coupling. I also reported the squeezing resulting from the combined effects of dispersive and dissipative couplings; thus the device can be operated in one regime or the other. I derived the maximal frequency and quadrature angles needed to observe squeezing for given optomechanical coupling strengths. I also discussed the effects of temperature on squeezing.

In the last chapter, I examined the squeezing capability of dissipative OMS based on the optomechanical setup in Michelson-Sagnac interferometers (MSI) coupled to a vibrating membrane. I concluded that squeezing of the order of 10dB or more can be produced in the output radiation. My next stage of study is to find a method to increase this squeezing magnitude. It is known that quantum feedback can be useful to control quantum devices. One possibility is to introduce the quantum feedback control method to manage the output performance of OMS. Specifically, one can consider placing a reflective mirror to the output port of the MSI and inject the squeezed output back to the OMS. This feedback input interferes with the cavity field; therefore it may further suppress the quantum fluctuation of the specific quadrature leading to enhancement of the squeezing magnitude. The interference can be controlled by tuning the phase of the feedback.

The squeezing of the nanomechanical mirror is much more difficult to achieve. Theoretically, the mirror can be put in a quantum state by pumping the OMS with squeezed light from the outside or by driving the OMS with both red and blue detuned pumps. An experimental implementation of this technique has just appeared [138, 139]. One important possibility is to use the anharmonicity of the mirror to produce mechanical squeezing. This would be an important direction to follow.

Bibliography

[1] A. Ashkin. “Applications of laser radiation pressure”. In: *Science* 210.4474 (1980), pp. 1081–1088 (cit. on p. 2).

[2] V. B. Braginsky et al. *Quantum measurement*. Cambridge University Press, 1995 (cit. on p. 2).

[3] T. J. Kippenberg and K. J. Vahala. “Cavity optomechanics: Back-action at the mesoscale”. In: *Science* 321.5893 (2008), pp. 1172–1176 (cit. on p. 2).

[4] M. Aspelmeyer, P. Meystre, and K. Schwab. “Quantum optomechanics”. In: *Physics Today* 65.7 (2012), pp. 29–35 (cit. on p. 2).

[5] M. Aspelmeyer, T. J. Kippenberg, and F. Marquardt. “Cavity optomechanics”. In: *Rev. Mod. Phys.* 86 (4 Dec. 2014), pp. 1391–1452 (cit. on pp. 2, 8).

[6] D. Van Thourhout and J. Roels. “Optomechanical device actuation through the optical gradient force”. In: *Nature Photonics* 4.4 (2010), pp. 211–217 (cit. on p. 2).

[7] G. Guccione et al. “Scattering-Free Optical Levitation of a Cavity Mirror”. In: *Phys. Rev. Lett.* 111 (18 Oct. 2013), p. 183001 (cit. on p. 2).

[8] M. Scala et al. “Matter-Wave Interferometry of a Levitated Thermal Nano-Oscillator Induced and Probed by a Spin”. In: *Phys. Rev. Lett.* 111 (18 Oct. 2013), p. 180403 (cit. on p. 2).

[9] W. Lechner et al. “Cavity Optomechanics of Levitated Nanodumbbells: Nonequilibrium Phases and Self-Assembly”. In: *Phys. Rev. Lett.* 110.14 (2013) (cit. on p. 2).

[10] O. Romero-Isart et al. “Quantum Magnetomechanics with Levitating Superconducting Microspheres”. In: *Phys. Rev. Lett.* 109.14 (2012) (cit. on p. 2).

[11] O. Romero-Isart et al. “Large Quantum Superpositions and Interference of Massive Nanometer-Sized Objects”. In: *Phys. Rev. Lett.* 107 (2 July 2011), p. 020405 (cit. on p. 2).

[12] O. Romero-Isart et al. “Large Quantum Superpositions and Interference of Massive Nanometer-Sized Objects”. In: *Phys. Rev. Lett.* 107.2 (2011) (cit. on p. 2).

[13] J. Bochmann et al. “Nanomechanical coupling between microwave and optical photons”. In: *Nature Physics* 9.11 (2013), pp. 712–716 (cit. on p. 2).

[14] T. Bagci et al. “Optical detection of radio waves through a nanomechanical transducer”. In: *Nature(London)* 507.7490 (2014), pp. 81–85 (cit. on pp. 2, 58).

[15] H. Li et al. “Multichannel cavity optomechanics for all-optical amplification of radio frequency signals”. In: *Nature Communications* 3 (2012) (cit. on p. 2).

[16] M. R. Vanner et al. “Cooling-by-measurement and mechanical state tomography via pulsed optomechanics”. In: *Nature Communications* 4 (2013) (cit. on p. 2).

[17] G. Anetsberger et al. “Near-field cavity optomechanics with nanomechanical oscillators”. In: *Nature Physics* 5.12 (2009), pp. 909–914 (cit. on p. 2).

[18] T. J. Kippenberg and K. J. Vahala. “Cavity Opto-Mechanics”. In: *Opt. Express* 15.25 (Dec. 2007), pp. 17172–17205 (cit. on p. 2).

[19] C. Dong et al. “Optomechanical Dark Mode”. In: *Science* 338.6114 (2012), pp. 1609–1613 (cit. on pp. 2, 7, 46, 57).

[20] G. Bahl et al. “Brillouin cavity optomechanics with microfluidic devices”. In: *Nature Communications* 4 (2013) (cit. on p. 2).

[21] A. B. Matsko et al. “Optomechanics with Surface-Acoustic-Wave Whispering-Gallery Modes”. In: *Phys. Rev. Lett.* 103.25 (2009) (cit. on pp. 2, 46).

[22] N. Brahms et al. “Optical Detection of the Quantization of Collective Atomic Motion”. In: *Phys. Rev. Lett.* 108.13 (2012) (cit. on p. 2).

[23] T. Botter et al. “Optical Readout of the Quantum Collective Motion of an Array of Atomic Ensembles”. In: *Phys. Rev. Lett.* 110.15 (2013) (cit. on p. 2).

[24] T. P. Purdy et al. “Tunable Cavity Optomechanics with Ultracold Atoms”. In: *Phys. Rev. Lett.* 105.13 (2010) (cit. on p. 2).

[25] X. Song et al. “Graphene Optomechanics Realized at Microwave Frequencies”. In: *Phys. Rev. Lett.* 113.2 (2014) (cit. on p. 2).

[26] M. Eichenfield et al. “A picogram- and nanometre-scale photonic-crystal optomechanical cavity”. In: *Nature(London)* 459.7246 (2009), 550–U79 (cit. on p. 2).

[27] O. Arcizet et al. “A single nitrogen-vacancy defect coupled to a nanomechanical oscillator”. In: *Nature Physics* 7.11 (2011), pp. 879–883 (cit. on p. 2).

[28] Y. Arita, M. Mazilu, and K. Dholakia. “Laser-induced rotation and cooling of a trapped microgyroscope in vacuum”. In: *Nature Communications* 4 (2013) (cit. on p. 2).

[29] G. Anetsberger et al. “Ultralow-dissipation optomechanical resonators on a chip”. In: *Nature Photonics* 2.10 (2008), pp. 627–633 (cit. on p. 2).

[30] F. Marquardt et al. “Quantum theory of cavity-assisted sideband cooling of mechanical motion”. In: *Physical Review Letters* 99.9 (2007), p. 093902 (cit. on p. 2).

[31] I. Wilson-Rae et al. “Theory of ground state cooling of a mechanical oscillator using dynamical backaction”. In: *Physical Review Letters* 99.9 (2007), p. 093901 (cit. on p. 2).

[32] A. D. OConnell et al. “Quantum ground state and single-phonon control of a mechanical resonator”. In: *Nature* 464.7289 (2010), pp. 697–703 (cit. on p. 2).

[33] J. D. Teufel et al. “Sideband cooling of micromechanical motion to the quantum ground state”. In: *Nature(London)* 475 (7356 July 2011), pp. 359–363 (cit. on pp. 2, 96).

[34] J. Chan et al. “Laser cooling of a nanomechanical oscillator into its quantum ground state”. In: *Nature* 478.7367 (2011), pp. 89–92 (cit. on p. 2).

[35] M. Vogel. “Principles of Lasers, 5th edn., by O. Svelto: Scope: monograph. Level: advanced undergraduate and above”. In: *Contemporary Physics* 53.2 (2012), pp. 173–173 (cit. on p. 3).

[36] G. S. Agarwal. *Quantum Optics*. Cambridge University Press, 2012 (cit. on pp. 5, 80, 94).

[37] J. C. Sankey et al. “Strong and tunable nonlinear optomechanical coupling in a low-loss system”. In: *Nature Physics* 6.9 (2010), pp. 707–712 (cit. on pp. 6, 7).

[38] M. Karuza et al. “Optomechanically induced transparency in a membrane-in-the-middle setup at room temperature”. In: *Phys. Rev. A* 88 (1 July 2013), p. 013804 (cit. on p. 6).

[39] J.-Q. Liao and F. Nori. “Single-photon quadratic optomechanics”. In: *Scientific Reports* 4 (2014) (cit. on pp. 6, 79).

[40] W. Wieczorek et al. “Optimal State Estimation for Cavity Optomechanical Systems”. In: *Phys. Rev. Lett.* 114 (22 2015), p. 223601 (cit. on p. 7).

[41] E. Verhagen et al. “Quantum-coherent coupling of a mechanical oscillator to an optical cavity mode”. In: *Nature(London)* 482.7383 (2012), pp. 63–67 (cit. on p. 7).

[42] R. Leijssen and E. Verhagen. “Strong optomechanical interactions in a sliced photonic crystal nanobeam”. In: *Scientific Reports* 5 (2015), p. 15974 (cit. on pp. 7, 98).

[43] K. Qu et al. “Optomechanical Ramsey interferometry”. In: *Phys. Rev. A* 90 (5 Nov. 2014), p. 053809 (cit. on pp. 8, 13, 30, 46, 79, 118).

[44] C. Genes et al. “Chapter 2 Quantum Effects in Optomechanical Systems”. In: *Advances in Atomic Molecular and Optical Physics*. Vol. 57. Academic Press, 2009, pp. 33 –86 (cit. on pp. 9, 94).

[45] A. Dorsel et al. “Optical Bistability and Mirror Confinement Induced by Radiation Pressure”. In: *Phys. Rev. Lett.* 51 (17 Oct. 1983), pp. 1550–1553 (cit. on p. 10).

[46] O. Kyriienko, T. C. H. Liew, and I. A. Shelykh. “Optomechanics with Cavity Polaritons: Dissipative Coupling and Unconventional Bistability”. In: *Phys. Rev. Lett.* 112.7 (2014) (cit. on p. 10).

[47] F. Marquardt, J. G. E. Harris, and S. M. Girvin. “Dynamical Multistability Induced by Radiation Pressure in High-Finesse Micromechanical Optical Cavities”. In: *Phys. Rev. Lett.* 96 (10 Mar. 2006), p. 103901 (cit. on p. 10).

[48] D. F. Walls and G. J. Milburn. *Quantum optics / D.F. Walls, Gerard J. Milburn*. English. 2nd ed. Springer Berlin, 2008, xii, 425 p. : (cit. on pp. 11, 80, 82, 94).

[49] A. Nunnenkamp et al. “Quantum-Limited Amplification and Parametric Instability in the Reversed Dissipation Regime of Cavity Optomechanics”. In: *Phys. Rev. Lett.* 113.2 (2014) (cit. on p. 13).

[50] J. Qian et al. “Quantum Signatures of the Optomechanical Instability”. In: *Phys. Rev. Lett.* 109.25 (2012) (cit. on p. 13).

[51] M Karuza et al. “Optomechanical sideband cooling of a thin membrane within a cavity”. In: *New J. Phys.* 14.9 (2012), p. 095015 (cit. on p. 13).

[52] K. Qu and G. S. Agarwal. *Optical memories and transduction of fields in double cavity optomechanical systems*. 2012. eprint: `arXiv:1210.4067` (cit. on pp. 13, 14, 26, 79, 118).

[53] K. Qu and G. S. Agarwal. “Phonon-mediated electromagnetically induced absorption in hybrid opto-electromechanical systems”. In: *Phys. Rev. A* 87.3 (2013) (cit. on pp. 14, 16, 43, 79, 118).

[54] X. Zhang et al. “Electromagnetically induced absorption in a three-resonator metasurface system”. In: *Scientific Reports* 5 (May 2015), p. 10737 (cit. on pp. 14, 62, 79, 118).

[55] K. Qu and G. S. Agarwal. “Fano resonances and their control in optomechanics”. In: *Phys. Rev. A* 87.6 (2013) (cit. on pp. 14, 16, 79, 118).

[56] K. Qu and G. S. Agarwal. “Strong squeezing via phonon mediated spontaneous generation of photon pairs”. In: *New J. Phys.* 16.11 (2014), p. 113004 (cit. on pp. 14, 118).

[57] K. Qu and G. S. Agarwal. “Generating quadrature squeezed light with dissipative optomechanical coupling”. In: *Phys. Rev. A* 91 (6 June 2015), p. 063815 (cit. on pp. 15, 102, 118).

[58] G. S. Agarwal and S. Huang. “Electromagnetically induced transparency in mechanical effects of light”. In: *Phys. Rev. A* 81 (4 Apr. 2010), p. 041803 (cit. on pp. 16, 17, 26, 43, 68, 79).

[59] S. Weis et al. “Optomechanically Induced Transparency”. In: *Science* 330.6010 (2010), pp. 1520–1523 (cit. on pp. 16, 26, 28, 43, 68).

[60] A. H. Safavi-Naeini et al. “Electromagnetically induced transparency and slow light with optomechanics”. In: *Nature(London)* 472.7341 (2011), pp. 69–73 (cit. on pp. 16, 26, 43, 68, 69).

[61] A. Kronwald and F. Marquardt. “Optomechanically Induced Transparency in the Nonlinear Quantum Regime”. In: *Phys. Rev. Lett.* 111.13 (2013) (cit. on pp. 16, 26, 43).

[62] I.-C. Hoi et al. “Demonstration of a single-photon router in the microwave regime”. In: *Physical review letters* 107.7 (2011), p. 073601 (cit. on pp. 16, 43).

[63] G. Agarwal and S. Huang. “Optomechanical systems as single-photon routers”. In: *Physical Review A* 85.2 (2012), p. 021801 (cit. on pp. 16, 62).

[64] L. Tian and H. Wang. “Optical wavelength conversion of quantum states with optomechanics”. In: *Physical Review A* 82.5 (2010), p. 053806 (cit. on p. 16).

[65] V. Fiore et al. “Optomechanical light storage in a silica microresonator”. In: *Phys. Rev. A* 87 (2 Feb. 2013), p. 023812 (cit. on pp. 16, 26, 29, 43, 46).

[66] S. Barzanjeh et al. “Reversible Optical-to-Microwave Quantum Interface”. In: *Phys. Rev. Lett.* 109 (13 Sept. 2012), p. 130503 (cit. on pp. 16, 44, 70).

[67] K. Qu and G. S. Agarwal. “Ramsey spectroscopy with squeezed light”. In: *Optics Letters* 38.14 (2013), pp. 2563–2565 (cit. on pp. 16, 30, 38, 118).

[68] J. T. Hill et al. “Coherent optical wavelength conversion via cavity optomechanics”. In: *Nature Communications* 3 (2012) (cit. on pp. 16, 44, 46, 58, 70).

[69] A. I. Lvovsky, B. C. Sanders, and W. Tittel. “Optical quantum memory”. In: *Nature photonics* 3.12 (2009), pp. 706–714 (cit. on p. 26).

[70] C. Clausen et al. “Quantum storage of photonic entanglement in a crystal”. In: *Nature* 469.7331 (2011), pp. 508–511 (cit. on p. 26).

[71] C. Clausen et al. “Quantum storage of heralded polarization qubits in birefringent and anisotropically absorbing materials”. In: *Physical review letters* 108.19 (2012), p. 190503 (cit. on p. 26).

[72] R Grobe, F. T. Hioe, and J. Eberly. “Formation of shape-preserving pulses in a nonlinear adiabatically integrable system”. In: *Physical review letters* 73.24 (1994), p. 3183 (cit. on p. 26).

[73] M. Fleischhauer and M. Lukin. “Dark-state polaritons in electromagnetically induced transparency”. In: *Physical Review Letters* 84.22 (2000), p. 5094 (cit. on pp. 26, 43).

[74] C. Liu et al. “Observation of coherent optical information storage in an atomic medium using halted light pulses”. In: *Nature* 409.6819 (2001), pp. 490–493 (cit. on pp. 26, 43).

[75] D. Phillips et al. “Storage of light in atomic vapor”. In: *Physical Review Letters* 86.5 (2001), p. 783 (cit. on pp. 26, 43).

[76] T. N. Dey and G. S. Agarwal. “Storage and retrieval of light pulses at moderate powers”. In: *Phys. Rev. A* 67 (3 Mar. 2003), p. 033813 (cit. on pp. 26, 29).

[77] M. T. Rakher et al. “Quantum transduction of telecommunications-band single photons from a quantum dot by frequency upconversion”. In: *Nature Photonics* 4.11 (2010), pp. 786–791 (cit. on p. 43).

[78] S. E. Harris and Y. Yamamoto. “Photon Switching by Quantum Interference”. In: *Phys. Rev. Lett.* 81 (17 Oct. 1998), pp. 3611–3614 (cit. on p. 43).

[79] A. Lezama, S. Barreiro, and A. M. Akulshin. “Electromagnetically induced absorption”. In: *Phys. Rev. A* 59 (6 June 1999), pp. 4732–4735 (cit. on p. 43).

[80] A. M. Akulshin, S. Barreiro, and A. Lezama. "Electromagnetically induced absorption and transparency due to resonant two-field excitation of quasidegenerate levels in Rb vapor". In: *Phys. Rev. A* 57 (4 Apr. 1998), pp. 2996–3002 (cit. on p. 43).

[81] A. Lipsich et al. "Absorption spectra of driven degenerate two-level atomic systems". In: *Phys. Rev. A* 61 (5 Apr. 2000), p. 053803 (cit. on p. 43).

[82] L. Tian. "Adiabatic State Conversion and Pulse Transmission in Optomechanical Systems". In: *Phys. Rev. Lett.* 108 (15 Apr. 2012), p. 153604 (cit. on pp. 44, 58, 70).

[83] Y.-D. Wang and A. A. Clerk. "Using Interference for High Fidelity Quantum State Transfer in Optomechanics". In: *Phys. Rev. Lett.* 108.15 (2012) (cit. on pp. 44, 58, 70).

[84] R. W. Andrews et al. "Bidirectional and efficient conversion between microwave and optical light". In: *Nature Physics* 10.4 (Mar. 2014), pp. 321–326 (cit. on pp. 44, 45, 57, 79).

[85] T. Bagci et al. "Optical detection of radio waves through a nanomechanical transducer". In: *Nature* 507.7490 (2014), pp. 81–85 (cit. on pp. 44, 45).

[86] J. M. Dobrindt, I. Wilson-Rae, and T. J. Kippenberg. "Parametric Normal-Mode Splitting in Cavity Optomechanics". In: *Phys. Rev. Lett.* 101.26 (2008) (cit. on p. 53).

[87] C. L. Garrido Alzar, M. A. G. Martinez, and P. Nussenzveig. "Classical analog of electromagnetically induced transparency". In: *American Journal of Physics* 70.1 (2002) (cit. on p. 55).

[88] D. D. Smith et al. "Coupled-resonator-induced transparency". In: *Phys. Rev. A* 69 (6 June 2004), p. 063804 (cit. on p. 55).

[89] A. Naweed et al. “Induced transparency and absorption in coupled whispering-gallery microresonators”. In: *Phys. Rev. A* 71 (4 Apr. 2005), p. 043804 (cit. on p. 55).

[90] Y. Liu et al. “Electromagnetically Induced Transparency and Wideband Wavelength Conversion in Silicon Nitride Microdisk Optomechanical Resonators”. In: *Phys. Rev. Lett.* 110.22 (2013) (cit. on p. 58).

[91] L. Fan et al. “Cascaded optical transparency in multimode-cavity optomechanical systems”. In: *Nature communications* 6 (2015) (cit. on pp. 62, 79).

[92] S. Huang and G. Agarwal. “Entangling nanomechanical oscillators in a ring cavity by feeding squeezed light”. In: *New Journal of Physics* 11.10 (2009), p. 103044 (cit. on p. 62).

[93] F Altomare et al. “Tripartite interactions between two phase qubits and a resonant cavity”. In: *Nature Physics* 6.10 (2010), pp. 777–781 (cit. on p. 62).

[94] R. D. Kekatpure et al. “Phase-Coupled Plasmon-Induced Transparency”. In: *Phys. Rev. Lett.* 104 (24 2010), p. 243902 (cit. on p. 62).

[95] B. Gallinet and O. J. Martin. “Influence of electromagnetic interactions on the line shape of plasmonic Fano resonances”. In: *ACS nano* 5.11 (2011), pp. 8999–9008 (cit. on p. 62).

[96] U. Fano. “Effects of Configuration Interaction on Intensities and Phase Shifts”. In: *Phys. Rev.* 124 (6 Dec. 1961), pp. 1866–1878 (cit. on p. 63).

[97] C. Galland et al. “Heralded Single-Phonon Preparation, Storage, and Readout in Cavity Optomechanics”. In: *Phys. Rev. Lett.* 112.14 (2014) (cit. on p. 79).

[98] P. Rabl. “Photon Blockade Effect in Optomechanical Systems”. In: *Phys. Rev. Lett.* 107.6 (2011) (cit. on p. 79).

[99] A. Nunnenkamp, K. Borkje, and S. M. Girvin. "Single-Photon Optomechanics". In: *Phys. Rev. Lett.* 107.6 (2011) (cit. on p. 79).

[100] J. Restrepo, C. Ciuti, and I. Favero. "Single-Polariton Optomechanics". In: *Phys. Rev. Lett.* 112.1 (2014) (cit. on p. 79).

[101] J. P. Dowling. "Quantum optical metrology–the lowdown on high-N00N states". In: *Contemporary physics* 49.2 (2008), pp. 125–143 (cit. on p. 79).

[102] C. C. Gerry, A. Benmoussa, and R. A. Campos. "Parity measurements, Heisenberg-limited phase estimation, and beyond". In: *J. Mod. Opt.* 54.13-15 (2007), pp. 2177–2184 (cit. on p. 79).

[103] C. M. Caves. "Quantum-mechanical noise in an interferometer". In: *Phys. Rev. D* 23.8 (1981), p. 1693 (cit. on p. 79).

[104] K. Stannigel et al. "Optomechanical Transducers for Long-Distance Quantum Communication". In: *Phys. Rev. Lett.* 105.22 (2010) (cit. on p. 80).

[105] K. Stannigel et al. "Optomechanical Quantum Information Processing with Photons and Phonons". In: *Phys. Rev. Lett.* 109.1 (2012) (cit. on p. 80).

[106] S. L. Braunstein and P. van Loock. "Quantum information with continuous variables". In: *Rev. Mod. Phys.* 77 (2 June 2005), pp. 513–577 (cit. on p. 80).

[107] N. Gisin et al. "Quantum cryptography". In: *Rev. Mod. Phys.* 74 (1 Mar. 2002), pp. 145–195 (cit. on p. 80).

[108] N. Gisin and R. Thew. "Quantum communication". In: *Nature Photonics* 1.3 (2007), pp. 165–171 (cit. on p. 80).

[109] A. Furusawa et al. "Unconditional quantum teleportation". In: *Science* 282.5389 (1998), pp. 706–709 (cit. on p. 80).

[110] R. Raussendorf and H. J. Briegel. "A one-way quantum computer". In: *Phys. Rev. Lett.* 86.22 (2001), p. 5188 (cit. on p. 80).

[111] P. Walther et al. “Experimental one-way quantum computing”. In: *Nature(London)* 434.7030 (2005), pp. 169–176 (cit. on p. 80).

[112] L. Mandel and E. Wolf. *Optical Coherence and Quantum Optics*. Cambridge University Press, 1995 (cit. on pp. 80, 94).

[113] A. Metelmann and A. A. Clerk. “Quantum-Limited Amplification via Reservoir Engineering”. In: *Phys. Rev. Lett.* 112 (13 Apr. 2014), p. 133904 (cit. on p. 91).

[114] Y.-D. Wang and A. A. Clerk. “Reservoir-Engineered Entanglement in Optomechanical Systems”. In: *Phys. Rev. Lett.* 110 (25 June 2013), p. 253601 (cit. on p. 94).

[115] L. Tian. “Robust Photon Entanglement via Quantum Interference in Optomechanical Interfaces”. In: *Phys. Rev. Lett.* 110 (23 June 2013), p. 233602 (cit. on p. 94).

[116] Z.-q. Yin and Y.-J. Han. “Generating EPR beams in a cavity optomechanical system”. In: *Phys. Rev. A* 79 (2 Feb. 2009), p. 024301 (cit. on p. 94).

[117] C. Fabre et al. “Quantum-noise reduction using a cavity with a movable mirror”. In: *Phys. Rev. A* 49 (2 Feb. 1994), pp. 1337–1343 (cit. on pp. 94, 99, 110).

[118] D. W. C. Brooks et al. “Non-classical light generated by quantum-noise-driven cavity optomechanics”. In: *Nature(London)* 488.7412 (2012), pp. 476–480 (cit. on p. 94).

[119] A. H. Safavi-Naeini et al. “Squeezed light from a silicon micromechanical resonator”. In: *Nature(London)* 500 (7461 Aug. 2013), p. 185 (cit. on pp. 94, 95, 99, 110, 113).

[120] T. P. Purdy et al. “Strong Optomechanical Squeezing of Light”. In: *Phys. Rev. X* 3 (3 Sept. 2013), p. 031012 (cit. on pp. 94, 96, 99, 110, 113).

[121] F. Massel et al. “Multimode circuit optomechanics near the quantum limit”. In: *Nature Communications* 3 (2012) (cit. on p. 96).

[122] A. Fainstein et al. “Strong Optical-Mechanical Coupling in a Vertical GaAs/AlAs Microcavity for Subterahertz Phonons and Near-Infrared Light”. In: *Phys. Rev. Lett.* 110.3 (2013) (cit. on p. 98).

[123] M. J. Woolley and A. A. Clerk. “Two-mode squeezed states in cavity optomechanics via engineering of a single reservoir”. In: *Phys. Rev. A* 89 (6 June 2014), p. 063805 (cit. on p. 99).

[124] A. Kronwald, F. Marquardt, and A. A. Clerk. “Dissipative optomechanical squeezing of light”. In: *New J. Phys.* 16.6 (2014), p. 063058 (cit. on p. 99).

[125] D Riste et al. “Deterministic entanglement of superconducting qubits by parity measurement and feedback”. In: *Nature(London)* 502.7471 (2013), pp. 350–354 (cit. on p. 99).

[126] T. Palomaki et al. “Entangling mechanical motion with microwave fields”. In: *Science* 342.6159 (2013), pp. 710–713 (cit. on p. 99).

[127] F. Elste, S. M. Girvin, and A. A. Clerk. “Quantum Noise Interference and Backaction Cooling in Cavity Nanomechanics”. In: *Phys. Rev. Lett.* 102 (20 May 2009), p. 207209 (cit. on p. 99).

[128] M. Li, W. H. P. Pernice, and H. X. Tang. “Reactive Cavity Optical Force on Microdisk-Coupled Nanomechanical Beam Waveguides”. In: *Phys. Rev. Lett.* 103 (22 Nov. 2009), p. 223901 (cit. on pp. 99, 100).

[129] S. Huang and G. S. Agarwal. “Reactive coupling can beat the motional quantum limit of nanowaveguides coupled to a microdisk resonator”. In: *Phys. Rev. A* 82 (3 Sept. 2010), p. 033811 (cit. on pp. 99, 100).

[130] A. Xuereb, R. Schnabel, and K. Hammerer. "Dissipative Optomechanics in a Michelson-Sagnac Interferometer". In: *Phys. Rev. Lett.* 107 (21 Nov. 2011), p. 213604 (cit. on pp. 99, 100).

[131] S. P. Tarabrin et al. "Anomalous dynamic backaction in interferometers". In: *Phys. Rev. A* 88 (2 Aug. 2013), p. 023809 (cit. on pp. 99, 100).

[132] T. Weiss, C. Bruder, and A. Nunnenkamp. "Strong-coupling effects in dissipatively coupled optomechanical systems". In: *New J. Phys.* 15.4 (2013), p. 045017 (cit. on pp. 99, 100).

[133] M. Wu et al. "Dissipative and Dispersive Optomechanics in a Nanocavity Torque Sensor". In: *Phys. Rev. X* 4 (2 June 2014), p. 021052 (cit. on pp. 99, 100).

[134] Y.-C. Liu et al. "Dynamic Dissipative Cooling of a Mechanical Resonator in Strong Coupling Optomechanics". In: *Phys. Rev. Lett.* 110.15 (2013) (cit. on p. 99).

[135] A. Sawadsky et al. "Observation of Generalized Optomechanical Coupling and Cooling on Cavity Resonance". In: *Phys. Rev. Lett.* 114 (4 Jan. 2015), p. 043601 (cit. on pp. 100, 101, 103, 105, 110, 112, 115, 117).

[136] H. Shen et al. "Controlled-X gate with cache function for one-way quantum computation". In: *Phys. Rev. A* 85.3 (2012) (cit. on p. 118).

[137] G. S. Agarwal and K. Qu. "Spontaneous generation of photons in transmission of quantum fields in PT-symmetric optical systems". In: *Phys. Rev. A* 85.3 (2012) (cit. on p. 118).

[138] E. E. Wollman et al. "Quantum squeezing of motion in a mechanical resonator". In: *Science* 349.6251 (2015), pp. 952–955 (cit. on p. 121).

[139] J. L. Miller. "A quantum squeezed state of a mechanical resonator has been realized". In: *Physics Today* 68.11 (2015), pp. 14–16 (cit. on p. 121).

VITA

Kenan Qu

Candidate for the Degree of

Doctor of Philosophy

Dissertation: Coherent Interference Effects and Squeezed Light Generation in Optomechanical Systems

Major Field: Physics

Biographical:

Personal Data: Born in City of Changzhi, Shanxi Province, China on January 13, 1988.

Education:

Received the B.S. degree from Nankai University, Tianjin, China, 2009, in Microelectronics

Completed the requirements for the degree of Doctor of Philosophy with a major in Physics Oklahoma State University in December, 2015.